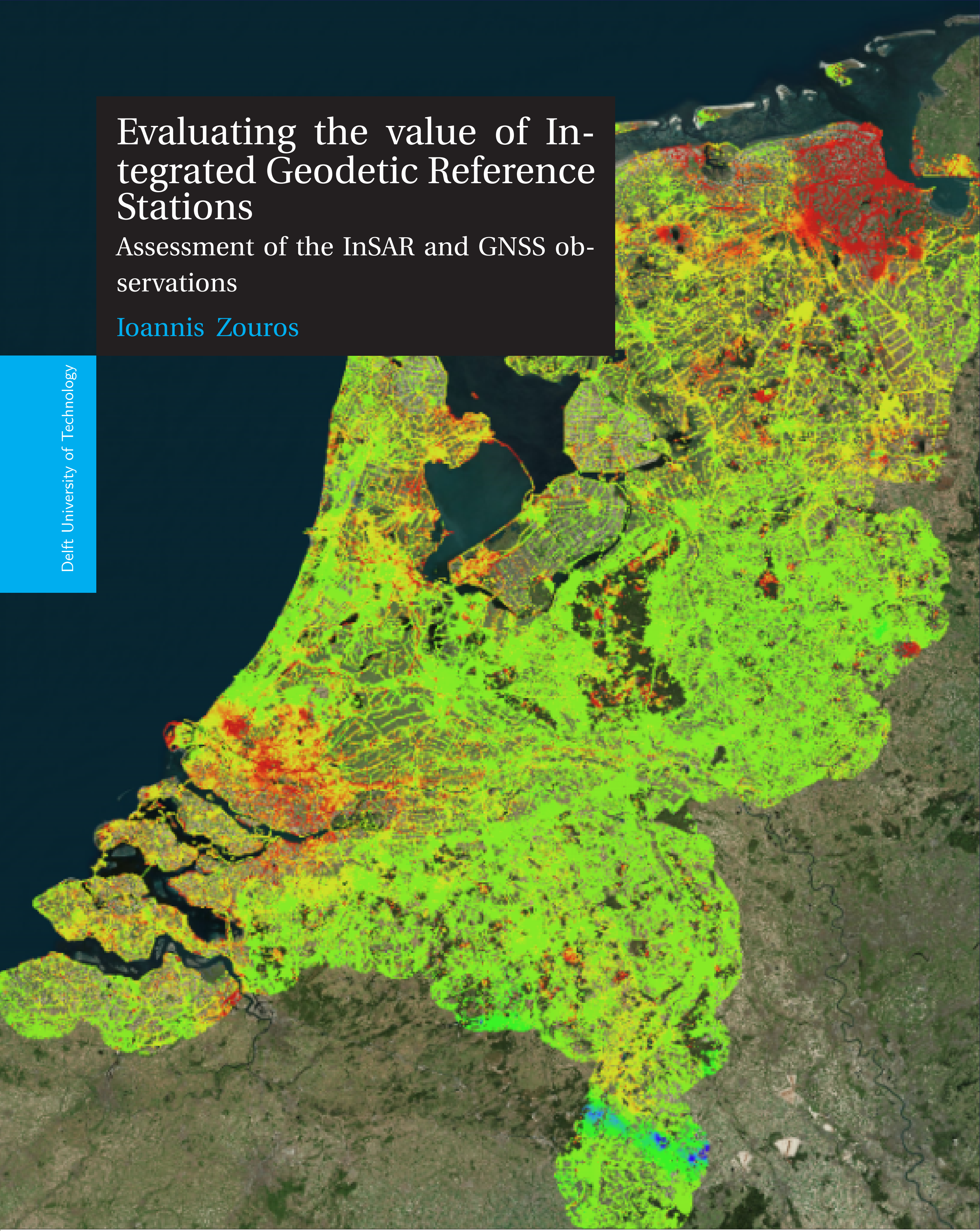

Evaluating the value of Integrated Geodetic Reference Stations

Assessment of the InSAR and GNSS observations

Ioannis Zouros

Delft University of Technology

Delft University of Technology

Challenge the future

Evaluating the value of Integrated Geodetic Reference Stations

Assessment of the InSAR and GNSS observations

by

Ioannis Zouros

in partial fulfillment of the requirements for the degree of

Master of Science
in Applied Earth Sciences

at the Delft University of Technology,
to be defended publicly on, Thursday 2nd December 2021 at 15:00.

Student number:	5034868	
Project duration:	February 22, 2021 – December 2, 2021	
Supervisor:	Prof. dr. ir. R. F. Hanssen,	TU Delft, Geoscience and Remote Sensing (CiTG)
Thesis committee:	ir. S. A. N. van Diepen,	TU Delft, Geoscience and Remote Sensing (CiTG)
	Dr. ir. D. C. Slobbe,	TU Delft, Geoscience and Remote Sensing (CiTG)
External:	Dr. ir. G. Ketelaar,	Nederlandse Aardolie Maatschappij
	ir. H. Maljaars,	SkyGeo Netherlands B.V.

Preface

With this project, my journey at the TU Delft comes to an end. Since in my view every project requires teamwork, I'll use the next lines to thank my teammates.

First and foremost, regarding this master thesis, I want to thank the chair of my graduation committee, Ramon Hanssen. Before I started, I could never imagine that I would receive this amount of help and guidance. All the hours spent in progress meetings, going over either basic principles or more advanced details so I fully understand what's under the process are appreciated. The questions he would always use to stimulate my thinking were the most valuable intake that I had, which allowed me to develop my rational and skills.

Also, I feel thankful for all the time and effort Simon van Diepen spent with me while being my daily supervisor. Simon was always, but always there to answer my questions, resolve technical difficulties, and was available to regularly interrupt his schedule to help me when I got stuck. His willingness to offer his expertise was extremely important for this project to be finished.

I would also like to thank Hanno Maljaars, my company supervisor from SkyGeo. I am grateful that he didn't hesitate to agree to supervise a graduation project, while at the same time managing SkyGeo's engineering team. His thoughts and suggestions were valuable and the aid he provided for this work was always prompt and punctual. Also, I want to thank SkyGeo Netherlands B.V. for providing the PSI algorithm used for this analysis.

Regarding this project, more people were involved. I want to thank Freek van Leijen, Hans van der Marel and Cornelis Slobbe from the TU delft, but also Gini Ketelaar from Nederlandse Aardolie Maatschappij. They provided data and useful input for this work. It goes without saying that my daily-huddle buddies, Wietske, Max, Marc, and Philip helped me with their questions during our daily meetings.

Since this journey was not only about the thesis, I also want to thank all my classmates and friends I made here. They were amazing companions and sharing time with them made everything so much easier and natural. My friends in Greece played a huge role as well. Although being apart, we managed to make our friendship even stronger. Also, a big thanks to my godparents in New York, whose help was again unprecedented.

Finally, I owe the biggest gratitude to my family, my parents, and my brother. There's a proverb saying: Shared joy is a double joy; shared sorrow is half a sorrow. This challenging experience of being a TU Delft Master of Science student could never have been realized without you guys. Sharing feelings during difficult times, but also enjoying springs of happiness in good moments kept me pushing forward. You have created the best family environment anyone could ever ask for. I feel so lucky and grateful for growing up and living with you. You have been and will always be the most important people in my life, the only wealth I have.

Ioannis Zouros
Delft, November 2021

Abstract

Interferometric Synthetic Aperture Radar (InSAR) and Global Navigation Satellite Systems (GNSS) are widely used to monitor the dynamic behavior of the Earth. InSAR is a geodetic technique that estimates millimeter-level relative displacement time-series in an opportunistic network of a multitude of coherent points on the Earth's surface, in a local datum. GNSS uses ground-based instrumentation to acquire time-series data over a limited number of specific and well-defined points in a known geodetic datum.

The Integrated Geodetic Reference Station (IGRS) is designed to combine these (and other) techniques into one common instrument, establishing an integrated benchmark, i.e., a GNSS antenna and two radar corner reflectors, ensuring an identical kinematic behavior. This enables a geodetic datum connection, effectively enabling the InSAR results to be represented in a common geodetic datum, instead of a free network. However, the efficacy of the IGRS has not yet been proven, i.e., a thorough analysis of the first empirical results of an IGRS network has not yet been performed.

Here we show that by using three years of data from a spatio-temporal network of 29 IGRS stations in an area of 60 × 60 km, and 742 independent Synthetic Aperture Radar (SAR) acquisitions, we reach a high level of agreement, demonstrating that IGRS can be used to connect InSAR information products to a well-defined geodetic datum.

By using an Overall Model Test with a significance level of 5% we found that 96% of the double-difference arcs in time and space, sustain the null hypothesis that both the InSAR and the GNSS results stem from the same distribution. We found that the main reason for rejecting the null hypothesis for the remaining 4% of the double-difference arcs is that the results of both the InSAR and the GNSS are affected by a leakage of signal from the functional to the stochastic model. For the InSAR observations there is inadequately modeled atmosphere leaking into the stochastic model, while for the GNSS it appears that the precision estimate of the periodically moving stations is worse than the non-periodically moving stations, which suggests that the stochastic model is influenced by the the functional model.

In the end, this study proved the efficacy of the IGRS to connect different geodetic datums, and this enables the InSAR results to be integrated in a well-defined geodetic datum.

List of Acronyms

1D	One Dimensional
2D	Two Dimensional
3D	Three Dimensional
ALS	Airborne Laser Scanning
AOI	Area Of Interest
APS	Atmospheric Phase Screen
DS	Distributed Scatterer
ECEF	Earth Centered Earth Fixed
ENU	East North Up
ETRS89	European Terrestrial Reference System 1989
GRS80	Geodetic Reference System 1980
GNSS	Global Navigation Satellite System
GPS	Global Positioning System
IGRS	Integrated Geodetic Reference Station
InSAR	Interferometric Synthetic Aperture Radar
LoS	Line-of-Sight
NAM	Nederlandse Aardolie Maatschappij
NAD	Normalised Amplitude Dispersion
OMT	Overall Model Test
PS	Persistent Scatterer
PSI	Persistent Scatterer Interferometry
RCS	Radar Cross Section
SCR	Signal to Clutter Ratio
SAR	Synthetic Aperture Radar
ZDP	Zero Doppler Plane

List of Figures

List of Tables

Contents

1

Introduction

In this chapter, relevant background information about the project is provided in section 1.1, along with the problem statement which can be found in section 1.2, followed by section 1.3 including the research objective. The outline of this thesis can be seen in section 1.4.

1.1. Background

Satellite-based Interferometric Synthetic Aperture Radar (InSAR) has shown to be remarkably useful for studying, detecting and monitoring the dynamic behavior of the Earth's surface and/or objects on it. In fact, the technology currently has an increasingly wide area of application, reaching from the wide-scale analysis of regional phenomena, such as subsidence, to the evaluation of single measurement points on an object in the built environment, such as a single part of a house. With a precision down to less than a millimeter, with a wide coverage, with a high density of measurement points, with a sub-weekly update frequency and an increasing number of satellite sensors available to acquire data, the technology is in a "golden age".

For many applications, InSAR is not the only suitable technique to estimate deformation. The main other geodetic techniques [1] for this purpose are: (i) Global Navigation Satellite System (GNSS), (ii) repeated leveling, (iii) repeated Airborne Laser Scanning (ALS) and (iv) repeated gravity surveys. All the above techniques are widely used to estimate deformation using different observables and benchmarks.

For InSAR, the principle observable is the double-difference (in time and space) displacement in the Line-of-Sight (LoS) to the radar instrument, derived from the interferometric phase (Hanssen, 2001). The selection of representative virtual benchmarks is performed aposteriori based on the objectives of the study. The principle observable of GNSS is the 3 Dimensional (3D) position of the GNSS-antenna reference point, acquired at one position and one epoch (Teunissen & Montenbruck, 2017). The deformation is obtained by differencing spatial differences between epochs (campaign style) or by differencing temporal differences between positions (continuous). It requires the apriori installation of physical benchmarks or continuous GNSS instrumentation.

For leveling, the principle observable is a spatial difference in geometric elevation between two benchmarks (Torge & Müller, 2012). The deformation is then derived by differencing spatial differences between epochs. It requires the apriori installation of physical benchmarks and manual in-situ land surveying. The cost increases with the area of interest and the temporal sampling. The principle observable of ALS is the 3D position of a location on the Earth's surface (Carter et al., 2007). The deformation is obtained by differencing the elevation of two positions for one epoch and subsequently subtracting two epochs. For gravimetry, the principle observable is the gravitational acceleration acquired at one position and one epoch (absolute gravimetry) or the spatial difference between gravitational accelerations at two positions at one epoch (relative gravimetry) (Timmen, 2010). The deformation is derived by spatio-temporal or temporal differencing, respectively, assuming that there is no mass movements between the epochs.

All the benchmarks needed and mentioned above are usually not at the same location, not surveyed at the same time, are used with different geodetic reference systems and are not representative of the same

---

[1] These techniques are not covered in detail in this thesis. A summary of the basic concepts for InSAR and GNSS can be found in section 2.1. For leveling and Airborne Laser Scanning, more information can be found in Kamphuis (2019) and for gravimetry in Wolfgang & Peter (2009).

physical signal. Therefore, a direct comparison (or integration) of these geodetic techniques will always result in significant differences.

1.2. Problem statement

InSAR observations can generate deformation products, which are then used for several applications, from modelling volcanoes to detecting landslides or infrastructure stability analysis (Czikhardt et al., 2021). Yet, given all it's feats, there are still a number of significant shortcomings. While the intrinsic observations may be of high quality, it is often not exactly known what it is that we are measuring, or, in different words, it is sometimes difficult to estimate where the effective center of the scatterers is located. Also, InSAR is inherently a relative technique, meaning that all observations are taken with respect to a reference point, that is assumed to be stable, although its actual behavior is not known. What is more, although the phase observations precision can reach the millimeter level, the geolocation of the Persistent Scatterers usually can only reach a precision up to the decimeter level, often missing a link to the physical objects on the Earth's surface (Czikhardt et al., 2021).

An idea to overcome some of these shortcomings is to link InSAR with one or more of the deformation techniques elaborated in section 1.1. Linking these techniques together in a meaningful and quantitatively sound way has proven to be very difficult. Typically, each technique has its own set of (virtual) benchmarks. For example, while the GNSS data are available as point values of a GNSS antenna (i.e., known physical source), the InSAR data are available without exact information about the source (i.e., spatially spread). For this reason, the interpretation of the comparison between these two techniques will always be affected by some sort of interpolation.

In order to conquer this problem we could force a pixel value in the InSAR deformation image to represent the exact deformation of the GNSS antenna. In doing so, it is ensured that observations for both the InSAR and the GNSS stem from the same origin. As a result of this, the deformation estimates could then be translated to a common datum and could possibly be interpreted together correctly. The materialization of this idea is the Integrated Geodetic Reference Station (IGRS), see Figure 1.1 (Kamphuis, 2019). This means that working with these instruments would yield that the time-series data represent the same deformation characteristics, which is an essential aspect in the interpretation of observations stemming from different sensors or monitoring techniques.

Figure 1.1: The IGRS in Engelbert, Groningen (Kamphuis, 2019).

These stations were specifically designed to link several deformation geodetic techniques (InSAR, GNSS, leveling, ALS, relative gravity, photogrammetry). In other words, it is a collocated benchmark whose motion can be estimated as a single mechanical structure.

The concept was adopted by Nederlandse Aardolie Maatschappij (NAM) in the northern part of the Netherlands, around the broader Groningen area, where 29 stations have been installed in collaboration with TU Delft and 06-GPS, see Figure 1.2.

Figure 1.2: Map with all the IGRS used in the study. Here we see the location of all 29 IGRS installed in the broader Groningen area. The station "Engelbert" shown in Figure 1.1 is depicted with "ENGE" in this map.

Kamphuis (2019) studied the design and installation of the network and played an important role in installing it. By the time of that project, less than a year of data was acquired. Thus, the main recommendation was to evaluate an extended time-series of data coming from these stations. Now we already have available time-series data up to almost three years long from 29 IGRS. This amount of data coming from a network of IGRS was never available before. Our intention is to use the data stemming from the IGRS network to assess the InSAR and the GNSS observations. In other words, this project focuses on the evaluation of the technique agreement between InSAR and GNSS using around three years of data. Besides the abundance of data available, what is crucial and novel about this research is that for the first time we are able to compare InSAR and GNSS results in the observation space. A lot of studies are available comparing, for instance, the estimated displacement rates from these techniques. In this case, a more robust comparison of the results is available. The comparison of the results of the geodetic techniques in the observation space requires a clear, identifiable, collocated target. This is for the first time available with the IGRS.

1.3. Research objective

The IGRS is designed to serve as a common benchmark for several geodetic techniques to be connected. In such a way, the widely and freely available InSAR observations, instead of referring to a so-called "free network" (i.e., positions and displacements of scatterers relative over time and space), could be integrated into a well defined geodetic datum or a reference system, such as the European Terrestrial Reference System 1989 (ETRS89) [2].

In this project we establish a methodology for evaluating the comparison of the results among the different geodetic techniques (InSAR and GNSS) and provide an evaluation of their quality. For the technique

---

[2] Coordinates in ETRS89 are expressed either as three dimensional (X, Y, Z) Cartesian coordinates or as three dimensional ellipsoidal coordinates (ϕ, λ, h), based on the Geodetic Reference System 1980 (GRS80) ellipsoid.

comparison, this study is using the available data from the IGRS in the broader Groningen area. The main research question of this thesis is:

How can we prove the efficacy of the IGRS to connect different geodetic datums from InSAR and GNSS estimates, using empirical data acquired from a network of IGRS?

In order to provide an answer to this question, it was broken down into the sub-questions that are listed below:

1. How can we establish a methodology for comparing InSAR and GNSS results recorded from an IGRS network?
2. How can the quality of the IGRS data for the InSAR and the GNSS observation techniques be evaluated?

1.4. Thesis outline

This project focuses on proving the efficacy of the IGRS to connect different geodetic datums by assessing the InSAR and the GNSS observations, with data from the IGRS located around the Groningen gas field. In chapter 2, we discuss background information behind the study. We begin with a short introduction to the basics of InSAR and GNSS, followed by the description of the quality of the techniques and a summary of the design specifications of the IGRS. The available data and the methodology of the comparison between the two techniques is covered in chapter 3. Also, the functional and the stochastic model developed are demonstrated, along with the definition of the stochastic model used for the testing performed. The results of the project and the discussion can be found in chapter 4. Finally, chapter 5 includes the conclusions of this thesis and the recommendations for future work and research.

2

Background

This chapter begins with an introduction to InSAR and GNSS, see section 2.1. The main principles of the two geodetic monitoring techniques are explained. The chapter continues with section 2.2, addressing of the quality of the position estimates for InSAR and GNSS observations. Lastly, it includes a description of the IGRS set-up which can be found in section 2.3.

2.1. Basic InSAR and GNSS principles

In this section we describe the fundamental concepts of InSAR and GNSS, in subsection 2.1.1 and subsection 2.1.3 respectively. The steps that the Persistent Scatterer Interferometry (PSI) algorithm uses are described in subsection 2.1.2.

2.1.1. Fundamental InSAR concepts

Interferometric Synthetic Aperture Radar and more specifically Persistent Scatterer InSAR is a common, satellite based deformation monitoring technique, providing a dense spatial distribution of millimeter resolution deformation estimates. The InSAR principle is covered in great detail in Hanssen (2001), van Leijen (2014) and Dheenathayalan (2019). Here, only a very short summary is presented.

InSAR relies on the measurement of the phase difference between two (or more) complex-valued Synthetic Aperture Radar (SAR) images, acquired from different orbital positions and/or at different times (Pepe & Calò, 2017). The complex value contains information about the amplitude A of the signal and the phase ψ of the signal. Both properties are combined in the complex phasor P (Hanssen, 2001) as

$$P = Ae^{i\psi}. \tag{2.1}$$

Each SAR image is formed by radio pulses emitted by the radar instrument which is mounted on the satellite. The pulses reach the Earth's surface and return to the radar. The objects that reflect the microwave signal are called scatterers. Following the taxonomy of Hu et al. (2019), we can distinguish between Point Scatterers (PS) and Distributed Scatterers (DS). In Point Scatterers the measurement of the pixel is dominated by one strong reflecting object, such as a corner reflector, which can be considered as a point source at a fixed 3D position. In Distributed Scatterers a large number of scattering objects, distributed within the entire resolution cell, form the measurement.

InSAR is using the phase difference of SAR images. This is because one phase observation itself cannot give any information about displacement. In order to get information about displacement we need four phase observations acquired in different time and space. Then, it is possible for the so called double-difference to be computed. This is the (wrapped) interferometric phase, which is a phase difference in space and time and can be denoted as

$$\phi^{w} = mod\{\phi+\pi, 2\pi\} - \pi, \quad \text{with } \phi = 2\pi k + \phi_N, \tag{2.2}$$

where $\phi_N \in [-\pi, \pi)$ expresses additive phase noise and k is the integer ambiguity number.

The basic InSAR principle is shown in Figure 2.1.

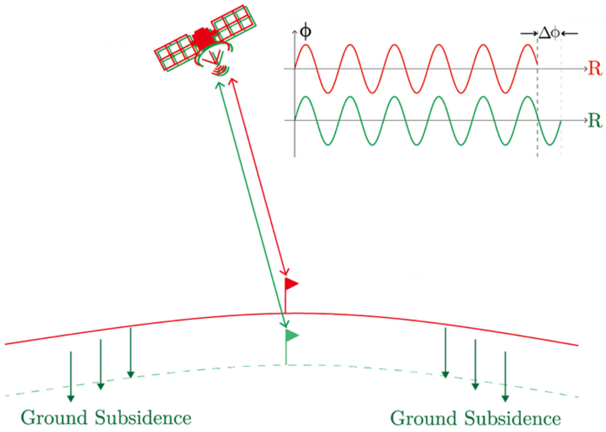

Figure 2.1: The interferometric phase difference. Here we see two satellite passes over the same point which has experienced a displacement (Qin, 2018).

The relation between the interferometric phase and a displacement in the radar Line-of-Sight direction (i.e., the "looking" direction of the satellite) is given by (Hanssen, 2001)

$$\phi = -\frac{4\pi}{\lambda}\delta_{\mathrm{LoS}}, \tag{2.3}$$

where λ is the radar wavelength and δ_{LoS} is the displacement in the LoS direction.

In order to be able to separate the displacement signal from the other components included, such as the topography, the atmospheric contribution and orbital errors, two or more satellite acquisitions must be used.

After the actual displacement is computed for each scatterer, it needs to be related to objects on Earth. All the scatterers lay on a 2 Dimensional (2D) reference system in the radar datum which is defined by two axes representing the pixel and line numbers of the SAR image. With a process called georeferencing, this 2D system is transformed into a 3D Terrestrial Reference Frame.

2.1.2. Persistent Scatterer Interferometry

InSAR is based on the interferometric processing of radar images. To overcome the major limitations of radar interferometry, that is, temporal decorrelation and atmospheric signal delay, radar interferometric time-series analysis methods have been introduced (Ferretti et al., 2000). The main objective of a radar interferometric time-series analysis method is the detection of those pixels for which the deformation time-series can be estimated with sufficient reliability (van Leijen, 2014). The Persistent Scatterer Interferometry algorithms are used to perform an analysis of a stack of interferograms to detect Persistent Scatterers and estimate their deformation time-series. In other words, these algorithms transform a radar interferometric data stack into a set of detected Persistent Scatterers. Below, the basic steps of the PSI algorithm used are explained.

The first step in order for the PSI algorithm to be initiated is the selection of a set of 1st order PS candidates. These PS have a stable temporal phase behavior, based on amplitude information. The main objective for selecting a set of 1st order PS candidates is to establish a reference network of coherent points, which are distributed homogeneously over the area of interest in order to interpolate the estimated atmospheric signal. At the next step in the PSI algorithm the 1st order PS are connected in the form of a network to make relative phase observations. After the formation of a network and the calculation of the relative phase observations per arc, the phases are unwrapped per arc in time together with the estimation of the parameters of interest (e.g., relative deformation rate, residual height difference, etc.). After the parameter estimation per arc the unwrapped interferometric phases and parameters of interest are relative in space, so they are then spatially unwrapped and integrated with respect to a single reference point. All the final results of PSI are relative to this reference point.

After the unwrapping, the atmosphere estimation is performed. A linear model is fitted (i.e., assuming a constant displacement rate in time) in order to compute the estimated interferometric phase. The atmospheric contribution is then assumed to be the residuals between the observed and the estimated phase. Then, in order to compute the atmospheric delay in each interferogram, known as the Atmospheric Phase Screen (APS), the algorithm interpolates the values obtained for the network points to the whole image. In this step kriging [1] is used. Kriging takes into account the statistical relationships among the measured points and assumes that the distance between them reflects a spatial correlation. In this way, we obtain estimated values for the atmospheric delay for the whole image.

The last step of the PSI algorithm is to desnify the network of Persistent Scatterers with a set of 2nd order PS candidates using a less strict threshold. Finally, the deformation time-series is obtained for the densified network of points.

2.1.3. Fundamental GNSS concepts

The term Global Navigation Satellite System is a generic name for multiple satellite based positioning systems (Hofmann-Wellenhof et al., 1992). The widely known Global Positioning System (GPS) has been developed from the United States, GLONASS has been developed by the Russian Federation, Beidou has been developed by the Chinese government, while Europe has developed the Galileo system.

GNSS positioning is based on the principle of triangulation and pseudo-ranges. With triangulation the coordinates of a point (x, y, z) can be determined from distance measurements to 3 other points with known coordinates $(x^{(}k), y^{(}k), z^{(}k))$. A pseudo-range $\rho^{(}k)$ is a one-way "distance" measurement obtained using independent clocks; the distance measurements are biased by an unknown clock offset b. This is illustrated in Figure 2.2. In other words, in order to find the position of a GNSS receiver antenna on Earth, we need measurements from at least 4 satellites.

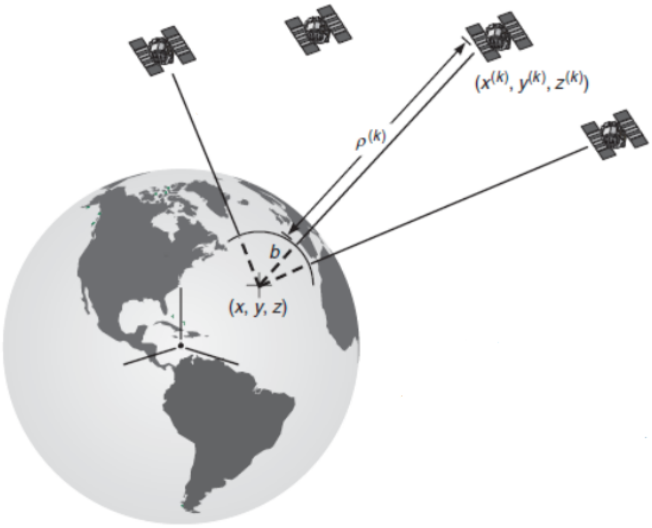

Figure 2.2: GNSS positioning. The position of the GNSS antenna is estimated based on the principle of trilateration (Enge, 1994).

With a single range measurement, we would know that the position of the receiver antenna must lie somewhere on a sphere, centered on the satellite, with a radius equal to the measured range. If we simultaneously make a range measurement to a second satellite, then our receiver must also lie on a sphere, centered on the second satellite. The intersection of the two spheres yields a circle, in which the receiver must lie on. A third simultaneous range measurement gives us a third sphere, which intersects the other two at just two points. One of these points can be immediately dismissed as being the location of our receiver, since it lies far out in space. So, the simultaneous measurement of the ranges to three satellites is sufficient to determine the position in 3D. However, in order to deal with the receiver clock error b and pseudo-ranges $p^{(}k)$, a measurement from a fourth satellite is needed (Teunissen & Montenbruck, 2017).

There are multiple methods for the use of GNSS for geodetic monitoring. In the case of relative measurements over a baseline between two stations, the difference in the observed phase between them is given by

$$\phi_2^i - \phi_1^i = F(\Delta x_{12}, \Delta y_{12}, \Delta z_{12}, \delta t, \Delta T, A^i), \tag{2.4}$$

where δt is the clock error, ΔT is the difference in tropospheric delay between the two receiver positions and A^i is an integer amount of full phase cycles. $\Delta x_{12}, \Delta y_{12}, \Delta z_{12}$ are identical for every satellite used and can

---

[1] A more detailed description of kriging as an interpolation method can be found in Oliver & Webster (1990).

be determined by solving a set of equations when signals from four (or more) satellites are simultaneously received (Teunissen & Montenbruck, 2017). In case of more than two stations the GNSS data is processed as a network. The basic equations are the same as in Eq. (2.4), but for the network processing different strategies can be used. Three popular strategies are compared in van der Marel (2020): Precise Point Positioning (PPP), regional network processing using the Bernese GPS software, and the state-space Real-Time-Kinematic processing used by 06-GPS to process the NAM GNSS data.

2.2. The quality of the position estimates

In this section we discuss the metrics that are used to describe the quality of the InSAR and the GNSS position estimates. There are a few ways with which we can obtain apriori values for the quality of the InSAR and the GNSS position estimates. Based on the choice of the stochastic model, the agreement level of the results of the two techniques will be influenced. The quality metrics used for the GNSS position estimates can be found in subsection 2.2.1 and the quality metrics used for the InSAR position estimates can be found in subsection 2.2.2.

2.2.1. Quality of the GNSS position estimates

For the quality of the GNSS position estimates the variance-covariance matrix Q_x of the east-north-up (e, n, u) components of the coordinates of the GNSS antenna is available per station and per epoch and is computed as

$$Q_{\hat{x}} = \begin{bmatrix} \sigma^2_{\hat{e}} & \sigma_{en} & \sigma_{eu} \\ \sigma_{ne} & \sigma^2_{\hat{n}} & \sigma_{nu} \\ \sigma_{ue} & \sigma_{un} & \sigma^2_{\hat{u}} \end{bmatrix}. \tag{2.5}$$

This matrix is used under the assumption that the variances and the covriances remain the same over time. The method of computation is given by van der Marel (2020). These are empirical estimates of the co-variance matrix based on the decompositions and analysis of the GNSS timeseries. The actual values for the IGRS stations (which are not included in the 2020 publication) have been computed by Van der Marel (2021). It should also be noted here, that in order to get the variances and the covariances of the e, n, u components of the GNSS position estimates, an annual and semi-annual signal have been removed from the time-series. If this signal hadn't been removed, the error statistics would have been larger due to the high seasonality in the data and, thus, not representative of the quality of the observations.

In order to directly compare the GNSS observations with the InSAR, the displacement vector should be projected to the radar LoS. The error propagation law is then applied for the quality of the LoS observations to be computed.

The variance of the LoS observations for one station can be computed as

$$\sigma^2_{GNSS_{\text{LoS}}} = p^T Q_x p, \tag{2.6}$$

where $p = \begin{bmatrix} \sin\theta \sin\alpha_d & \sin\theta\cos\alpha_d & \cos\theta \end{bmatrix}$ is a projection vector and θ and α_d are the incidence angle and the azimuth angle of the Zero Doppler Plane (ZDP) respectively. Details on the use of these angles are presented in section 3.2.

In order to make the GNSS observations comparable with the InSAR, we formed arcs between the stations. This is because we could not directly compare InSAR with GNSS observations, since InSAR is inherently a relative technique. The intention is to compare each arc of GNSS and InSAR observations of the network independently. So, for the variance of an arc between two stations a and b, based on the error propagation law for subtracting independent observations it is

$$\sigma^2_{DD_{GNSS_{\text{LoS}}}} = \sigma^2_{GNSS_{\text{LoS}_a}} + \sigma^2_{GNSS_{\text{LoS}_b}}, \tag{2.7}$$

where $\sigma^2_{GNSS_{\text{LoS}_a}}$ is the variance of station a and $\sigma^2_{GNSS_{\text{LoS}_b}}$ is the variance of station b.

2.2.2. Quality of the InSAR position estimates

The variance of the InSAR position estimates is not known apriori. The variances and covariances of the phase displacement depend on external factors, like the clutter (i.e., the unwanted background noise), which differ per area of study. Therefore, they must be obtained empirically from the observations.

This study uses the Normalized Amplitude Dispersion (NAD) to get an apriori estimate for the quality of the InSAR observations (van Leijen, 2014). The Normalized Amplitude Dispersion was preferred as an apriori estimate for the quality of the InSAR observations over the Signal-to-Clutter Ratio (SCR), since the IGRS are mounted on an artificial terrain (i.e., a concrete plate), thus, the clutter estimation would not be representative for other studies which can possibly have IGRS with different background noise. Having the time-series of the amplitude data a in dB, we can convert back to power A by

$$a = 10\log_{10} A \Rightarrow A = 10^{\frac{a}{10}}. \tag{2.8}$$

Then, the standard deviation σ_A and the mean μ_A of the amplitude of the time-series were computed for each IGRS (after their installation date) as

$$\sigma_A = \sqrt{\frac{\sum_{i=1}^{m}(\underline{A}_i - \bar{A}_i)^2}{m}}, \tag{2.9}$$

$$\mu_A = \frac{\sum_{i=1}^{m}\underline{A}_i}{m}, \tag{2.10}$$

where m is the number of epochs.

Then, the Normalized Amplitude Dispersion D_A can be computed for each scatterer as

$$D_A = \frac{\sigma_A}{\mu_A}. \tag{2.11}$$

It has been shown by Ferretti et al. (2000) that the relation between the phase standard deviation σ_ϕ and the Normalized Amplitude Dispersion D_A is

$$\sigma_\phi \simeq \tan\phi = \frac{\sigma_A}{\mu_A} = D_A. \tag{2.12}$$

Hence, a scatterer with a relatively constant amplitude in time (as the IGRS) is expected to have a low phase dispersion. Figure 2.3 is showing that indeed, the Normalized Amplitude Dispersion serves as a good approximation for the interferometric phase standard deviation, but only when the Normalized Amplitude Dispersion is not more than 0.25. In this scatterplot, a simulated relation between the Normalized Amplitude Dispersion and the the phase is shown, together with a black line indicating a linear relationship.

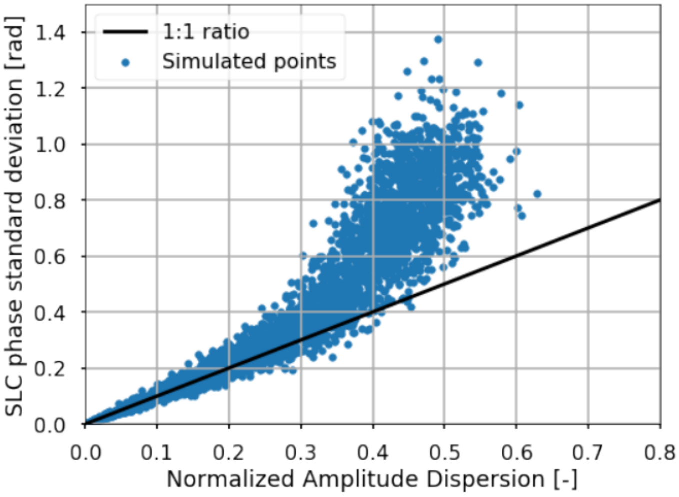

Figure 2.3: Relation between the Normalized Amplitude Dispersion and the phase standard deviation. Here we see a numerical simulation of the relation between the Normalized Amplitude Dispersion and phase standard deviation. Small values of the Normalized Amplitude Dispersion are a good approximation for phase stability (van Leijen, 2014).

In this study, we computed the Normalized Amplitude Dispersion of all the IGRS and it was found that all of these points have values smaller than 0.25. Because of this, we used the NAD as an approximation for the standard deviation of the interferometric phase. In order to compute the standard deviation of the phase in mm we used (Hanssen, 2001)

$$\sigma_d = \sigma_\phi \frac{\lambda}{4\pi} \text{ [mm]}, \tag{2.13}$$

where σ_ϕ is the phase standard deviation in radians and λ is the wavelength of the satellite (for Sentinel-1 C-band is: $\lambda = 55.5$ mm).

For an arc between two stations a and b, based on the error propagation law for subtracting independent observations it is

$$\sigma^2_{DD_{InSAR}} = \sigma^2_{d_a} + \sigma^2_{d_b}, \tag{2.14}$$

where $\sigma^2_{d_a}$ is the variance of station a and $\sigma^2_{d_b}$ is the variance of station b.

2.3. IGRS set-up

In this section we discuss some background information about the set-up of the IGRS and its design specifications. The IGRS hosts benchmarks for several geodetic techniques. We will take advantage of this fact in order to develop a methodology to properly evaluate a comparison between the results of InSAR and GNSS observations. Before that, we give a description of the instrument itself. The set-up of the IGRS is shown in Figure 2.4. The GNSS antenna is attached on a 2.40 m pole. On to it, a GSM/4G antenna is mounted and connected to the data modem which lays into the cabinet. Then, there are two corner reflectors (specifically oriented to radar satellites) for ascending and descending satellite tracks. The top plate (horizontal surface of about 0.5 m^2) can be used as a reference surface for airborne laser altimetry. A frame is being used to lift the weight of the reflectors which would otherwise bend the top plate. The instrument cabinet (containing GNSS electronics) is placed under the level of the top plate to keep the footprint small and the unwanted signal low.

The local e, n, u coordinate system which is defined can also be seen in Figure Figure 2.4. The origin is the point where the horizontal plate meets the vertical pole, the up vector is defined by the vertical pole and the system is completed by two axes pointing at the north and at the east direction. A more detailed description of the IGRS specifications can be found in Appendix A.

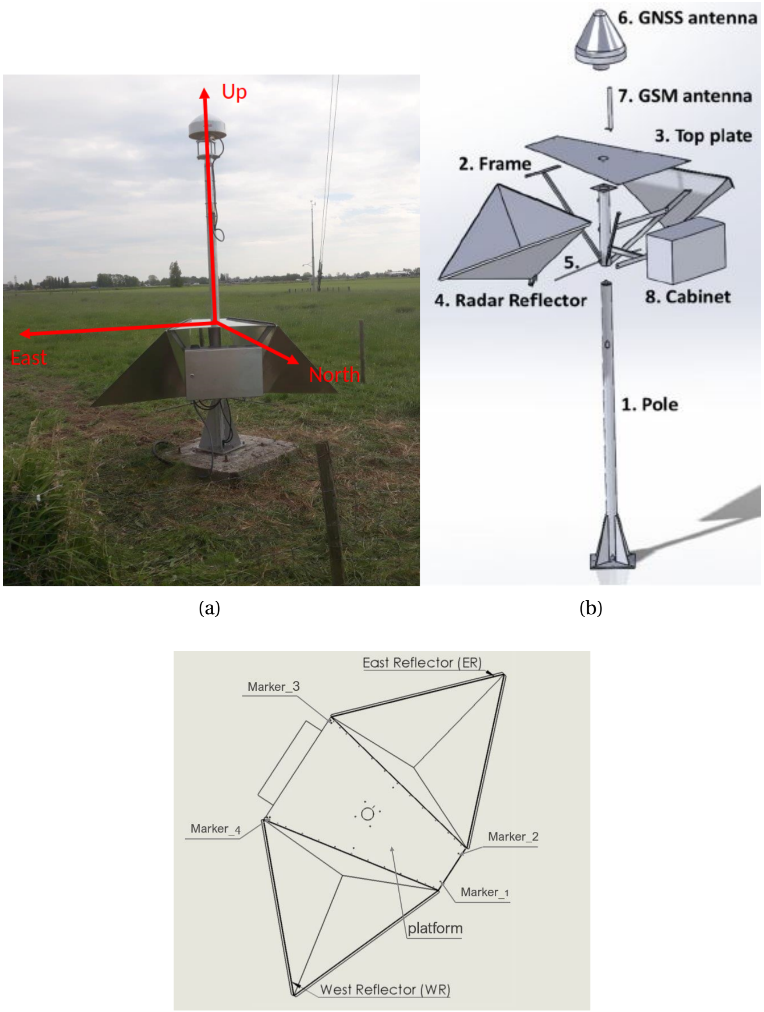

(a) (b)

(c)

Figure 2.4: Set-up of the IGRS station. (a) IGRS in field with the definition of the local e, n, u coordinate system. On the top of the mast is the GNSS antenna, supported by a pole which is firmly connected to three poles in the subsurface. The horizontal reference plate is in the middle with two radar reflectors at each side, for ascending and descending orbits. (b) IGRS components, platform and the radar reflectors on both sides. (c) Four markers are seen on the platform and two on either of the reflectors (Kamphuis, 2019).

3

Methodology

In this chapter we describe the methodology developed to assess the agreement level between the results of the InSAR and the GNSS observations from a network of IGRS. At first, we show the available data in section 3.1. Then, in section 3.2 and section 3.3 we explain the steps needed to be taken to make the observations comparable. The comparison methodology is described in section 3.4. More specifically, subsection 3.4.1 includes the description of the functional and the stochastic model used for comparison of the results of the two geodetic techniques and in subsection 3.4.2 we specify how the hypothesis testing is done.

3.1. Data availability

In this section the data which is available and used is presented.

In Table 3.1 we can see the SAR data available. The first column states the satellite mission, the second and the third refer to the heading and the track respectively, the fourth and the fifth refer to the start and end date of the PSI processing. Finally, the number of available images in the stacks is shown in the last column. We can observe that we have four Sentinel-1 tracks fully covering the broader Groningen area. The overview of these satellite tracks can be seen in Figure 3.1, where the broader Groningen area is depicted with red. The InSAR data are processed by SkyGeo.

Table 3.1: Independent interferometric time-series analysis data. In this table we can see all the available SAR data coming from four Sentinel-1 tracks.

	Mission	Heading	Track	Start date	End date	# Images
1	S1a/b	Descending	37	2018/01/02	2021/02/21	191
2	S1a/b	Ascending	88	2018/01/05	2021/02/18	185
3	S1a/b	Descending	139	2018/01/09	2021/02/22	188
4	S1a/b	Ascending	15	2018/01/06	2021/02/19	178

In Table 3.2 we can see an overview of the IGRS data together with the relevant radar data available. The station names are noted together with their respective IDs and the date on which they started operating. The number of available SAR images per station after each IGRS installation is shown in the last four columns of the table.

The GNSS data are processed by 06-GPS, on behalf of NAM, using a state-space Real-Time-Kinematic (RTK) processing method with software from the German company Geo++. The GNSS network, which consists of monitoring and reference stations, and the method of processing is described in detail by van der Marel (2020). The IGRS stations were not yet included in the 2020 publication, but have been processed used the same method. The hourly position estimates were provided by 06-GPS (Dentz, 2021). The stochastic model for the IGRS stations has been computed by Van der Marel (2021)

Finally, in Figure 3.2, one can see graphically all the available data from each IGRS. It is clear that not all IGRS were installed or starting operating on the same date. Besides this, in some cases there are some data missing. This is means that either the sensor was turned off (i.e., maintenance etc.) or data was not recorded at these times.

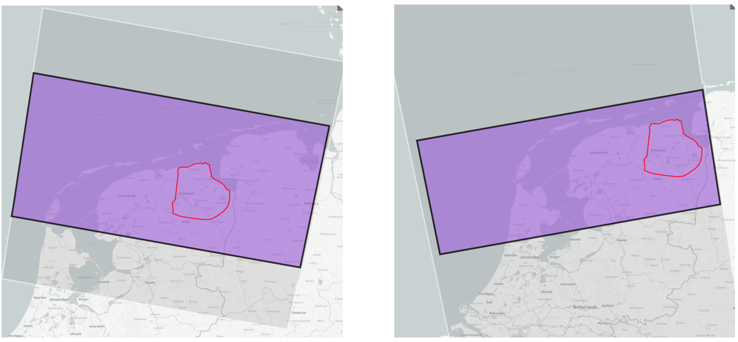

(a) Track 37, descending (b) Track 88, ascending

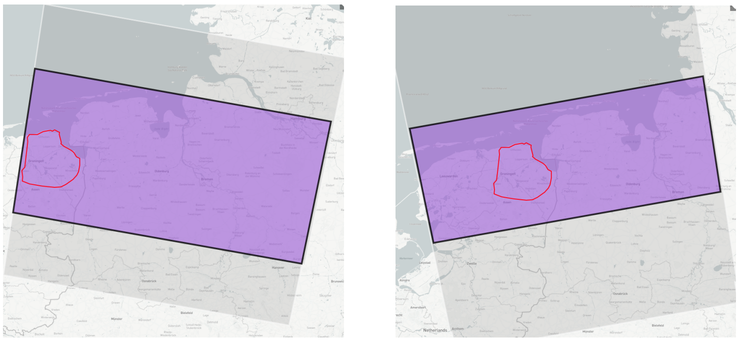

(c) Track 139, descending (d) Track 15, ascending

Figure 3.1: Sentinel-1 tracks processed. In this figure we can see an overview of all the Sentinel-1 tracks that were processed for this analysis. The Area of Interest (AOI) is shown in red.

Table 3.2: Overview of the IGRS data availability. The dates of installation and the number of satellite acquisitions available per station are shown (until 22/02/2021).

Station Name	Station ID	Alignment	Track 37 (dsc)	Track 88 (asc)	Track 139 (dsc)	Track 15 (asc)
SAPPEMEER	sapp	04/04/2018	164	156	161	155
NIEUW-SCHEEMDA	nsch	05/04/2018	162	153	159	152
HEILIGERLEE	heil	17/04/2018	157	150	155	145
OOSTWOLD	oosw	17/04/2018	163	155	160	154
BIERUM	bier	18/04/2018	156	148	152	147
LEERMENS	leer	18/04/2018	163	154	160	153
SCHILDWOLDE	schw	18/04/2018	152	148	150	144
OLDORP	oldo	19/04/2018	163	155	160	154
UITHUIZERMEEDEN	uith	19/04/2018	159	152	157	150
BARNHEEM	barn	24/04/2018	156	150	153	147
BORGSWEER	borg	24/04/2018	161	154	159	152
KOLHAM-1	kolh	24/04/2018	144	139	141	135
WARFFUM	warf	30/05/2018	149	143	146	141
ZUIDLAARDERVEEN	zldv	30/05/2018	141	138	140	135
NORG-3	nor3	31/05/2018	147	142	145	140
RODEN-1	rdn1	31/05/2018	147	142	144	140
STEENTIL	stil	24/07/2018	138	134	135	131
HOOGEZAND	hoog	24/07/2018	139	136	136	132
MIDLAREN	midl	24/07/2018	123	119	120	116
BEERTA	beer	25/07/2018	112	109	109	105
ENGELBERT (G69)	enge	25/07/2018	118	115	115	110
BEDUM	bedu	04/10/2018	134	131	132	127
RANUM	ranu	04/10/2018	134	131	131	127
WESTERNIELAND	wtnl	04/10/2018	124	121	120	116
HAREN (G66)	hare	02/04/2019	106	102	103	98
EEXT	eext	10/12/2019	62	58	61	57
GANZEDIJK	ganz	10/12/2019	65	61	64	60
BLIJHAM	blij	01/09/2020	18	17	17	17
EEMSHAVEN	emsh	01/09/2020	19	18	18	18

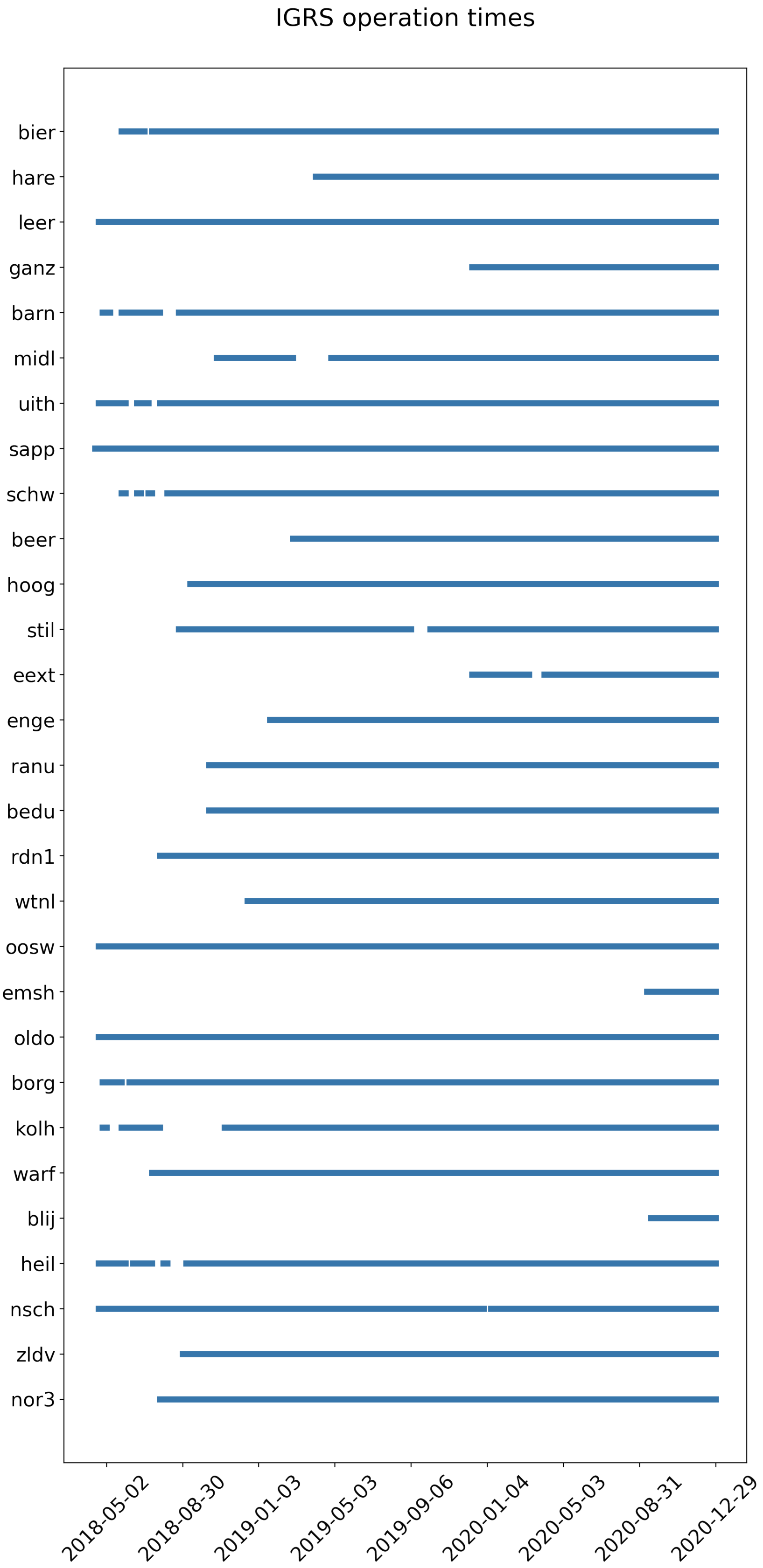

Figure 3.2: IGRS operation times. This graph shows the operation times of all the IGRS. A horizontal blue line next to each station means that there are data available for this station over the period for which the line runs. It can be observed that not all stations started their operation on the same date.

3.2. GNSS data handling

In this section we describe the steps that need to be taken to transform the GNSS data from ellipsoidal positions to a displacement vector comparable with the InSAR observations. The GNSS dataset was kindly provided by NAM and was processed by 06-GPS. It includes hourly data from the date of installation of each IGRS station until December 2020, when the study period of this thesis ends. In fact, the sampling frequency of the sensors is higher, acquiring one value per second. Then, during processing, the data are smoothed with a Kalman filter, resulting in hourly data (van der Marel, 2020). For this analysis, out of the filtered data we are using the GNSS value per day (i.e., hourly solutions) that is the closest to the respective SAR acquisition. The exact times of the acquisitions can be seen in Table 3.3.

Table 3.3: Sentinel-1 acquisition times. In this table we see the exact acquisition times of the Sentinel-1 images used in this analysis.

Track	Acquisition Time (UTC)	Acquisition time (local, summer)	Time used (local, summer)
37 (dsc)	05:50	7:50	08:00
88 (asc)	17:24	19:24	19:00
139 (dsc)	05:40	07:40	08:00
15 (asc)	17:15	19:15	19:00

The steps that need to be taken for the GNSS data to become comparable with the InSAR data are summarized schematically in Figure 3.3.

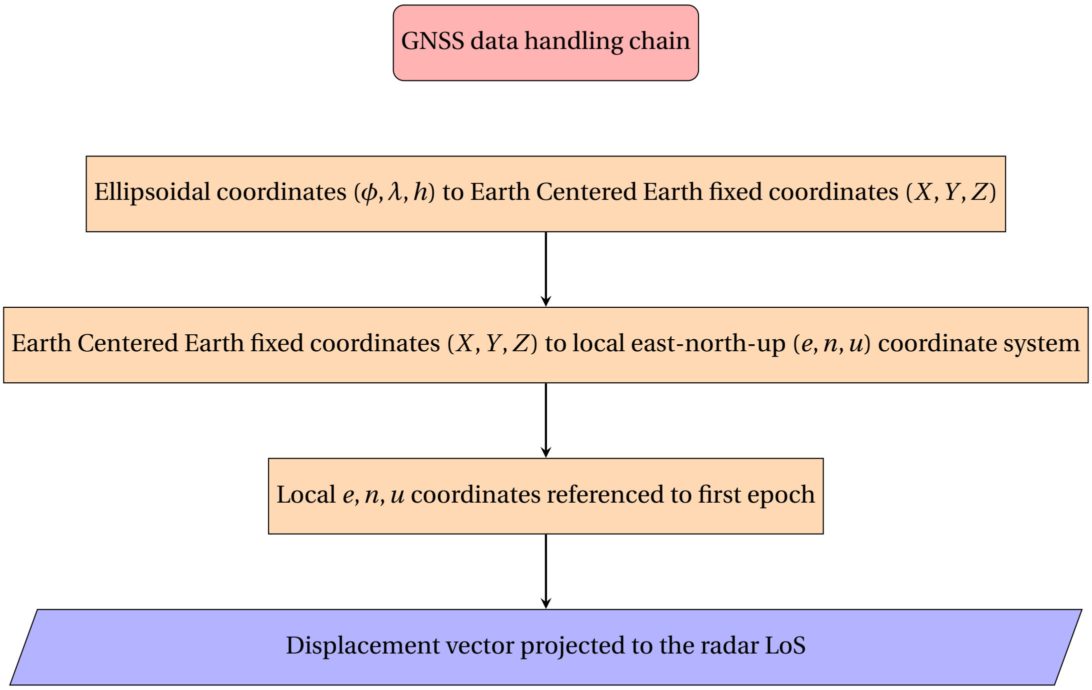

Figure 3.3: Flow chart of the GNSS data handling chain. This chart shows the processing steps that need to be taken in order to transform the GNSS coordinates from ϕ, λ, h to the radar LoS displacement vector.

The first step is to convert from the ellipsoidal coordinates ϕ, λ, h to Earth Centered Earth Fixed (ECEF) coordinates X, Y, Z. Provided that ϕ, λ, h are known, for this conversion it is

$$X = (N + h)\cos\phi\cos\lambda, \tag{3.1}$$

$$Y = (N + h)\cos\phi\sin\lambda, \tag{3.2}$$

$$Z = (N - Ne^2 + h)\sin\phi. \tag{3.3}$$

In the above equations, two additional terms are used: N and e. The radius of curvature in the prime vertical plane is indicated by N and can be calculated by

$$N = \frac{a}{\sqrt{1 - e^2 \sin^2 \phi}}. \tag{3.4}$$

The eccentricity of the ellipsoid used is indicated by e and can be calculated by

$$e^2 = 1 - \frac{b^2}{a^2}, \tag{3.5}$$

where a and b are the semi-major and semi-minor axis of the ellipsoid, respectively.

In order to be able to project the GNSS displacement vector to the LoS of the satellite, there is a need to make another conversion from the ECEF coordinates to a local e, n, u reference system. For this conversion we use (van der Marel, 2020; Van der Marel, 2021):

$$e = -\sin\phi x_d + \cos\phi y_d, \tag{3.6}$$

$$n = -\cos\phi \sin\lambda x_d - \sin\lambda \sin\phi y_d + \cos\lambda z_d, \tag{3.7}$$

$$u = \cos\lambda \cos\phi x_d + \cos\lambda \sin\phi y_d + \sin\lambda z_d, \tag{3.8}$$

where

$$x_d = X - (h_0 + N)\cos\lambda \cos\phi, \tag{3.9}$$

$$y_d = Y - (h_0 + N)\cos\lambda \sin\phi, \tag{3.10}$$

$$z_d = Z - (h_0 + (1 - e^2)N)\sin\lambda. \tag{3.11}$$

In the above equations the values for ϕ, λ and h_0 are the values that correspond to the first epoch of observations for each station. The radius of curvature in the prime vertical plane and the eccentricity of the ellipsoid are denoted in Eq.(3.4) and in Eq. (3.5) respectively.

At this point, the LoS projection is possible. For this we use a projection vector p as

$$d_{\text{LoS}} = p^T d_{enu}, \tag{3.12}$$

where

$$p = \begin{bmatrix} \sin\theta \sin\alpha_d \\ \sin\theta \cos\alpha_d \\ \cos\theta \end{bmatrix} \tag{3.13}$$

and

$$d_{enu} = \begin{bmatrix} \text{east} \\ \text{north} \\ \text{up} \end{bmatrix}. \tag{3.14}$$

In Eq. (3.13), θ indicates the incidence angle of the radar and α_d indicates the azimuth angle of the Zero Doppler Plane.

A graph showing the incidence angle of the satellite can be seen in Figure 3.4. This is the angle between the normal vector on the local ellipsoid, at the position of the target, and the LoS vector towards the satellite. The incidence angle varies in the range direction, so it is different for every pixel in a SAR image. This difference is taken into account when performing the LoS projection.

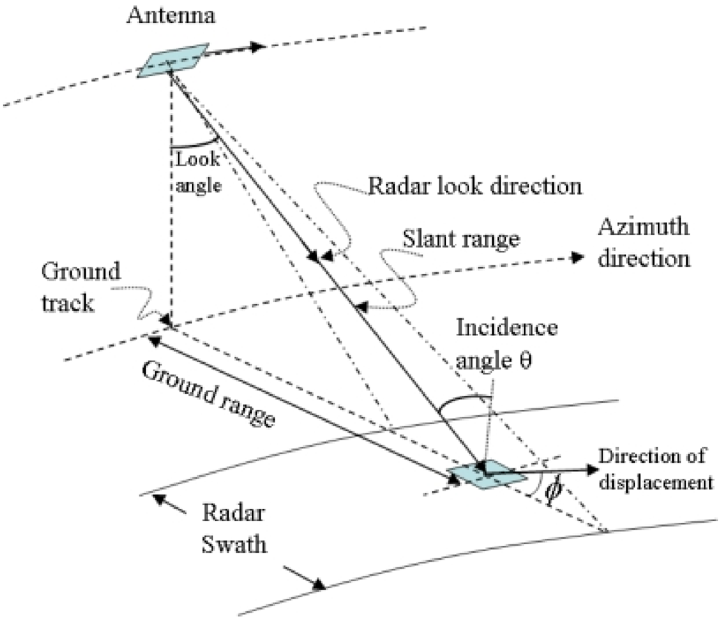

Figure 3.4: Satellite incidence angle θ. In this graph we depict the incidence angle θ of the radar which is formed between the radar wave incident direction and the normal direction to the scattering surface (Zhou et al., 2009).

The Zero Doppler Plane can be seen in Figure 3.5. This is the plane defined when the target is illuminated at its point of closest approach to the satellite.

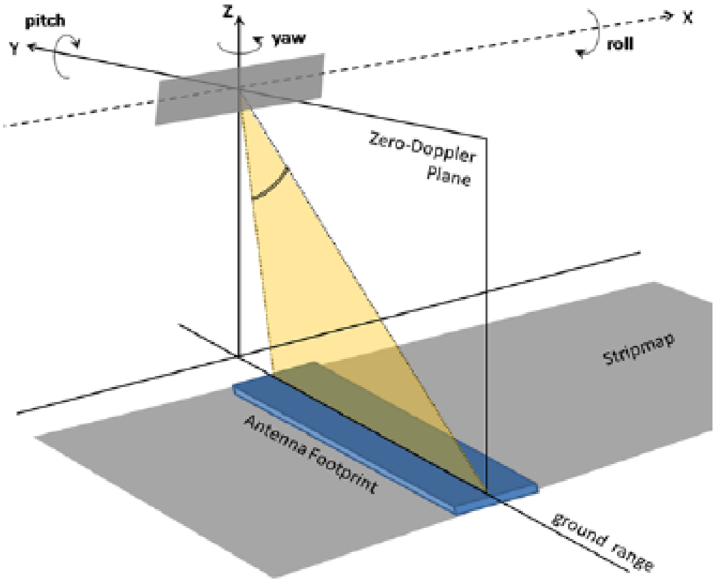

Figure 3.5: SAR Zero Doppler Plane. This graph shows the plane which is defined when the target is illuminated at its point of closest approach to the satellite (Nitti et al., 2012).

Each satellite's orbit forms an angle between the velocity vector of the satellite and the geometrical north vector. This angle is called the heading angle a_h of the satellite. The ZDP is perpendicular to the heading of the satellite. Due to the meridian convergence, the azimuth of the ZDP of the satellite at the Earth surface α_d is greater than the heading of the satellite α_h. This geometry is summarized in Figure 3.6 and is also taken into account when performing the LoS projection. A more detailed analysis of these angles can be found in Brouwer (2021).

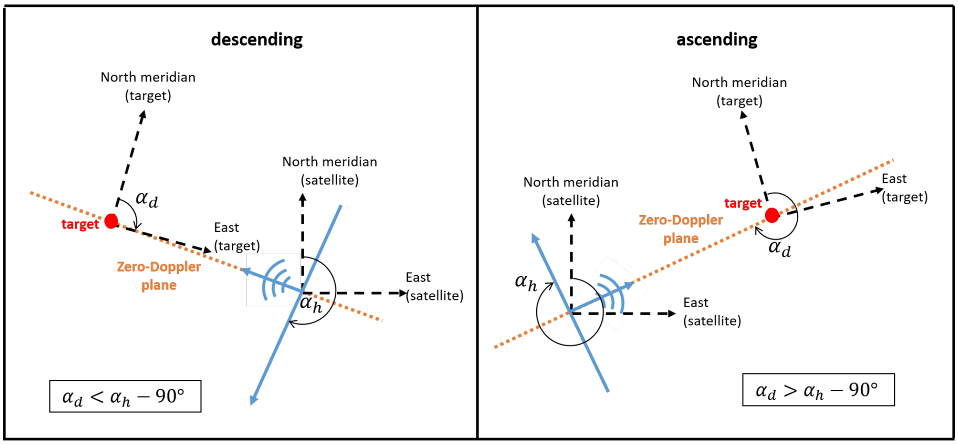

Figure 3.6: Angle of the Zero Doppler Plane. Due to the meridian convergence, the azimuth of the ZDP on Earth differs from the heading of the satellite (Brouwer, 2021).

3.3. InSAR data handling

For the Persistent Scatterer Interferometry processing, ascending tracks 88 and 15 and descending tracks 37 and 139 are used. The results from the PSI processing of the four datasets show the LoS displacement of millions of scatterers. Out of all the scatterers it is important to identify which point represents the IGRS. The optimal way to retrieve the IGRS coordinates in the radar image is to use a radar-coding algorithm. Due to lack of time, in this study a radar-coding algorithm was not developed and used. Instead, the points that correspond to the IGRS were identified manually. Below, we can find the description of a radar-algorithm followed by the explanation of the manual identification that we used in this project.

Using a single SAR image, the position of a scatterer can only be described in two dimensions, azimuth and (slant) range. The transformation, known as geocoding, to map the position of a scatterer from the radar geometry to a 3D Terrestrial Reference Frame is explained in detail in Dheenathayalan et al. (2016). Here, we need to do the opposite (i.e., from known 3D coordinates to the radar geometry.) This step is possible, since the 3D coordinates of the IGRS are known (with high precision), from the GNSS observations. The position of a radar scatterer P in 2D radar coordinates (a_P and r_P) is measured by performing a complex 2D Fast Fourier Transform, zero padding and detecting the sub-pixel location of its amplitude peak (Dheenathayalan et al., 2016). This coordinate system has its origin in the phase center of the GNSS antenna. Therefore, the 2D position of the IGRS in radar coordinates can be obtained from a single Single Look Complex image. According to Dheenathayalan (2019), the 2D position of a scatterer P in radar coordinates (a_P and r_P) can be computed as

$$\begin{aligned} r_P &= \frac{v_0}{2}\tau_0 + \mu_P(\Delta\tau + \tau_{lo}) + \tau_{pd_p} + \tau_{set_p} + \tau_{tect}) + r_{cal}, \\ a_P &= v_{s/c}(t_0 + v_P(\Delta t + t_{lo}) + t_{bi_p} + t_{set_p} + t_{tect}) + a_{cal}, \end{aligned} \tag{3.15}$$

where v_0 is the velocity of microwaves in vacuum, $v_{s/c}$ is the local velocity of the spacecraft, t_0 is the time of transmission of first pulse of focused image, τ_0 is the time to the first range pixel, Δ_τ is the range sampling interval, Δ_t is the azimuth pulse repetition interval, τ_{lo}, t_{lo} are the corrections applied to Δ_τ and Δ_t due to local-oscillator drift, τ_{set_p}, t_{set_p} are timing correction factors due to solid earth tides in range and azimuth, respectively, τ_{tect}, t_{tect} are corrections due to plate tectonics, in range and azimuth, respectively, τ_{pd_p} is the range path delay, t_{bi_p} is the azimuth bistatic correction, r_{cal}, a_{cal} are the residual unmodeled calibration offsets.

In this study, the points that correspond to the IGRS were identified manually out of all the scatterers included in the analysis. This had to be done separately, four times, for each one of the four satellite tracks processed. This was not ideal for several reasons. First of all, it requires manual labor, which would take much more time for another project including even more stations. In this way, the project can't be easily "scaled-up". Secondly, we cannot be certain whether the right point is selected (aiming for the one with the highest amplitude within the time series) or if it is confused with a signal coming from a strong sidelobe. Thirdly, it is possible that the PSI algorithm does not select the desired point to be a PS. Since the PSI processing starts before the installation of all stations, it can be that some of the stations may not be detected as PS from the algorithm, since before their installation, the respective point on the ground may hadn't been able to pass the quality threshold. In order to avoid this issue the quality thresholds of the PSI algorithm for selecting PS points were removed. This caused the algorithm to be computationally expensive. In order to make the algorithm computationally efficient we designed buffers of approximately 100 m surrounding each IGRS in order to process data, not over the entire the AOI, but only in close proximity around the IGRS.

In this way we were able to locate each one of the IGRS in the dataset (both in ascending and descending orbits) and, thus, to know their line and pixel coordinates. This approach worked for this project, but the problem cannot be considered solved. In order for this methodology to "scale-up", a radar-coding algorithm should be developed and used.

The plots showing the amplitude and the relative displacement time-series of all the IGRS in all satellite tracks used can be found in Appendix B.

3.4. Comparison methodology

In this section we describe the functional and the stochastic model used for the comparison of the results of the two techniques (see subsection 3.4.1) and we specify how the hypothesis testing is done (see subsection 3.4.2).

In order to compare between the results of the InSAR and the GNSS observations we are using a conditioned linear model. Based on Teunissen (2009), the linear systems of equations (in the implicit form) is defined as

$$B^T E(\underline{y}) = b_0, \tag{3.16}$$

where B is a given $m \times r$ matrix of rank$(B) = r$ and b_0 is a given vector, and is called a conditioned linear model for $E(\underline{y})$.

The expression for the Best Linear Unbiased Estimate (BLUE) of $\underline{y}$ is

$$\underline{\hat{y}} = \underline{y} - Q_{yy}B(B^T Q_{yy} B)^{-1}(B^T \underline{y} - b_0), \tag{3.17}$$

where Q_{yy} is the variance-covariance matrix of the observations.

The vector

$$\underline{t} = B^T \underline{y} - b_0 \quad \text{with} \quad E(\underline{t}) = 0, \quad D(\underline{t}) = B^T Q_{yy} B \tag{3.18}$$

is called the vector of misclosures.

This vector provides a direct measure for inconsistency. If the elements of $\underline{t}$ are large, we may have a reason to believe that the assumptions underlying the model have been misspecified. The vector of misclosures provides therefore a means of checking the validity of the model.

3.4.1. Functional and stochastic model

In order to compute metrics that will allow us to judge if the results of the InSAR and the GNSS observations are matching, it is needed to choose a functional and a stochastic model for the comparison. In this study, the vector of observations consists of the InSAR and the GNSS (projected in the LoS) double-difference arcs created by subtracting the time-series of each IGRS from the time series of all others (space differences) and for all available epochs (time differences). For each satellite track, there are $s = 29$ stations available within the AOI (with ascending and descending orbits), so for each technique, this yields:

$$N = \frac{s(s-1)}{2} = \frac{29(29-1)}{2} = 406 \text{ arcs} \tag{3.19}$$

In total, with four Sentinel-1 tracks used, this results in 406 × 4 = 1624 arcs. The number of available epochs for each arc is not the same for all arcs. With the study period spanning roughly from April 2018 to December 2020 and the first IGRS (sapp) being installed in April 2018 and the last ones (blij, emsh) being installed in September 2020, the number of available epochs per arc varies from about 160 images to around 20 images.

Before defining the functional and the stochastic model for the comparison between the results of the two techniques it is important to look at the definition of the functional and the stochastic model of each technique separately. Both for the InSAR and the GNSS observations we referenced the time-series data to the first epoch of available observations. So for InSAR, with $m+1$ indicating the number of epochs for which data are available the functional model is defined as

$$\phi = A\psi, \tag{3.20}$$

where ϕ indicates the interferometric phase, A is the design matrix and ψ refers to the SAR phase values. In a matrix formation the same equation can be written as

$$\begin{bmatrix} \phi_{21} \\ \phi_{31} \\ \vdots \\ \phi_{m1} \end{bmatrix} = \begin{bmatrix} -1 & 1 & 0 & \cdots & 0 \\ -1 & 0 & 1 & \cdots & 0 \\ \vdots & \vdots & \vdots & \ddots & \vdots \\ -1 & 0 & 0 & \cdots & 1 \end{bmatrix} \begin{bmatrix} \psi_1 \\ \psi_2 \\ \vdots \\ \psi_{m+1} \end{bmatrix}, \tag{3.21}$$

where ϕ_{m1} is the interferogram between epoch m and the first epoch and ψ_{m+1} refers to the phase value at epoch $m+1$.

Then, the stochastic model for the interferometric phase values is defined as

$$Q_\phi = A Q_\psi A^T, \tag{3.22}$$

where A is the design matrix and Q_ψ is the variance-covariance matrix of the SAR phase values. This matrix is defined as

$$Q_\psi = \begin{bmatrix} \sigma^2_{\psi_1} & 0 & \cdots & 0 \\ 0 & \sigma^2_{\psi_2} & & \vdots \\ \vdots & & \ddots & 0 \\ 0 & \cdots & 0 & \sigma^2_{\psi_{m+1}} \end{bmatrix}, \tag{3.23}$$

where $\sigma^2_{\psi_{m+1}}$ is the variance of the phase values at epoch $m+1$.

With this formulation, the variance-covariance matrix of the interferometric phase values is a full matrix. With the exact same handling, the variance-covariance matrix of the GNSS observations is also a full matrix.

In this study the goal is to address the agreement level of the results of the InSAR and the GNSS arcs individually. In this case the observations are the time-series data of the InSAR and the GNSS double-difference arcs between the stations. Under this intention only we can assume a diagonal variance-covariance matrix for the observations (i.e., disregarding the covariances between the arcs of the network) even though it doesn't represent reality, since we are not interested in the relations between the arcs, but only about treating them and comparing them independently. In this case, the relationship of an arc to the other arcs in the network is not relevant for the comparison that we do, thus, we can assume a diagonal variance-covariance matrix for the observations. Treating each arc independently means that we are not doing a network adjustment.

In order to evaluate each one of the 406 arcs (for each satellite track), the following mathematical model is designed. This conditioned linear model is described for one arc, but the same holds for all the arcs of the network.

With $m+1$ indicating the number of epochs for which data are available and t_0 indicating the first epoch of available observations, the vector of observations y $[2m \times 1]$ is defined as

$$\underline{y} = \begin{bmatrix} [\underline{y}_{InSAR}]^{t_1} \\ [\underline{y}_{GNSS}]^{t_1} \\ [\underline{y}_{InSAR}]^{t_2} \\ [\underline{y}_{GNSS}]^{t_2} \\ \vdots \\ [\underline{y}_{InSAR}]^{t_m} \\ [\underline{y}_{GNSS}]^{t_m} \end{bmatrix}, \tag{3.24}$$

where $[y_{InSAR}]^{t_m}$ indicates the InSAR double-difference between epochs t_0 and t_m among the two IGRS that are forming the arc and $[y_{GNSS}]^{t_m}$ indicates the GNSS double-difference between epochs t_0 and t_m among the two IGRS that are forming the same arc.

Then, the condition matrix B $[2m \times m]$ is defined as

$$B = \begin{bmatrix} 1 & -1 & 0 & 0 & \cdots & 0 & 0 \\ 0 & 0 & 1 & -1 & \cdots & 0 & 0 \\ \vdots & \vdots & \vdots & \vdots & & \vdots & \vdots \\ 0 & 0 & 0 & 0 & \cdots & 1 & -1 \end{bmatrix}. \tag{3.25}$$

Finally, the variance-covariance matrix of the observations Q_{yy} $[2m \times 2m]$ is assumed to be diagonal, since each arc is evaluated independently, and is defined as

$$Q_{yy} = \begin{bmatrix} \sigma^2_{InSAR} & 0 & 0 & 0 & \cdots & 0 & 0 \\ 0 & \sigma^2_{GNSS} & 0 & 0 & \cdots & 0 & 0 \\ 0 & 0 & \sigma^2_{InSAR} & 0 & \cdots & 0 & 0 \\ 0 & 0 & 0 & \sigma^2_{GNSS} & \cdots & 0 & 0 \\ \vdots & \vdots & \vdots & \vdots & & \vdots & \vdots \\ 0 & 0 & 0 & 0 & \cdots & \sigma^2_{InSAR} & 0 \\ 0 & 0 & 0 & 0 & \cdots & 0 & \sigma^2_{GNSS} \end{bmatrix}, \tag{3.26}$$

where σ^2_{InSAR} is the InSAR variance among the two IGRS forming the arc and σ^2_{GNSS} is the GNSS variance among the two IGRS that are forming the same arc. It is important to remember here what are the inputs of the variance-covariance matrix of the observations. For the GNSS observations, we use a variance-covariance matrix which is computed after an annual and semi-annual trend were removed. For the InSAR observations we use the Normalized Amplitude Dispersion as a good approximation for the observations quality. The variances of the InSAR and the GNSS observations are assumed to not be dependent on time and remain the same for all epochs of each arc.

With this formulation, the differences between the results of the two techniques, the vector of misclosures $\underline{t}$ $[m \times 1]$ can be computed as

$$\underline{t} = B^T \underline{y}. \tag{3.27}$$

The variance-covariance matrix of the vector of misclosures Q_{tt} $[m \times m]$ can then be computed as

$$Q_{tt} = B^T Q_{yy} B. \tag{3.28}$$

3.4.2. Hypothesis testing

With these observations we want to perform a statistical hypothesis testing. The goal is to provide a metric with which we can judge if the results between the two techniques are showing a "good" agreement.

An Overall Model Test (OMT) is performed in order to detect disturbances, errors, and anomalies in the observed data. For this test, the test statistic T is given by

$$T = \frac{\underline{t}^T Q_{tt}^{-1} \underline{t}}{m}, \tag{3.29}$$

where m is the number of epochs.

This test statistic T is computed for every one of the 406 arcs of the network and for all four tracks processed. It should be noted that just through the test statistic we cannot decide upon sustaining or rejecting the null hypothesis (H_o). Rejection can be caused either by large (functional) errors in the observed data (that are not covered by H_o), an inappropriate model for the data at hand or by poor specification of the observables' noise characteristics in the stochastic model (through matrix Q_{yy}). Just the test statistic alone can't provide the answer. In order to decide if the null hypothesis is sustained or rejected for each arc of the network a critical value should be used. As defined in Eq. (3.29), T has an F-distribution and the critical value K_α is taken from the relevant table, according to a chosen level of significance α. Then, the test reads

$$\text{reject } H_o \text{ if } T > K_\alpha.$$

The significance level α refers to the probability of rejecting the null hypothesis when it is true. It is also known a "false alarm" or type-I error, when the null hypothesis is falsely rejected.

After the Overall Model Test, we perform a w-test, in order to assess all the observations in each arc, per epoch. An important application of this test is outlier detection. An outlier affects just a single observation. To screen the observations, in order to identify those that are grossly affected by outliers, all the alternative hypotheses formed are tested against the default or nominal model, represented by H_o. This screening of the observations is also referred to as data snooping. When the test for observation i is rejected, it is concluded that observation i is affected by some extraordinarily large error. A common and practical way of dealing with an outlier is to leave the observation that was concluded to be subject to an outlier, out from further processing (Teunissen, 2009).

The expression for the w-test statistic (normalized residual) under the assumption of independent observations reads as

$$w_i = \frac{\underline{t}_i}{\sigma_t} \quad \text{for} \quad i = 1, \ldots, m, \tag{3.30}$$

where $\underline{t}_i$ is the misclosure between the InSAR and the GNSS results at epoch i and σ_t is the standard deviation. In order to compute σ_t we use the error propagation law for subtracting independent observations (InSAR and GNSS double-difference time-series). For each arc this writes as

$$\sigma_t = \sqrt{\sigma^2_{InSAR} + \sigma^2_{GNSS}} \tag{3.31}$$

and remains constant for all the epochs of the arc.

Using the same critical value as before the test becomes two-sided. This yields

$$\text{reject } H_o \text{ if } w < -\sqrt{K_\alpha} \text{ or } w > \sqrt{K_\alpha}.$$

Overall, in this chapter we discuss the methodology developed in order to evaluate the comparison of the results of the InSAR and the GNSS observations. We explain the steps that need to be done in order for the InSAR and GNSS observations to be comparable and the methodology used to assess the level of agreement between the results of the two geodetic techniques. In chapter 4 we discuss the results of this comparison. We will at first see the quality of the position estimates for both the InSAR and the GNSS observations and then explore the results of the hypothesis testing.

4

Results and discussion

In this chapter the quality of the GNSS and the InSAR position estimates are evaluated and the results of the hypothesis testing are presented, followed by a discussion around them. We discuss the quality of the GNSS and InSAR position estimates in section 4.1. In section 4.2 we address the performance of the InSAR functional model regarding a leakage of signal into the stochastic model. Finally, the results of the hypothesis testing can be found in section 4.3.

4.1. Quality of position estimates

In this section we can see the quality of the GNSS and the InSAR position estimates in subsection 4.1.1 and subsection 4.1.2 respectively. For a better interpretation of the results we made tables, histograms and we also present some of the LoS displacement plots.

4.1.1. Quality of GNSS position estimates

For the GNSS observations we used the variance-covariance matrix of the e, n, u components of the coordinates of each station, (see subsection 2.2.1). This matrix is used under the assumption that the variances and the covariances remain the same over time. These error statistics are computed after removing an annual and semi-annual trend. Using the error propagation law (see subsection 2.2.1) after projecting the observations to the satellite LoS we obtained the results per station and per epoch shown in Table 4.1.

To make the comparison of the quality estimates between the projection on each track easier, we made the histograms shown in Figure 4.1. Each histogram corresponds to one satellite Sentinel-1 track (two ascending and two descending tracks). The mean value μ of each histogram is depicted with a dashed black vertical line.

It shows that for almost all the stations the standard deviation is in the sub-mm level. Some of the exceptions are marked in bold in Table 4.1. One of these exceptions is station **NOR3**, whose LoS projection is shown in Figure 4.2.

Table 4.1: GNSS position estimates quality. In this table we can find the GNSS position estimates quality of all the IGRS projected to the LoS of each satellite track.

	t37 (dsc)	t88 (asc)	t139 (dsc)	t15 (asc)	
Station	$\sigma_{\text{GNSS,LoS}}$ [mm]	$\sigma_{\text{GNSS,LoS}}$ [mm]	$\sigma_{\text{GNSS,LoS}}$ [mm]	$\sigma_{\text{GNSS,LoS}}$ [mm]	(e,u) covariance [-]
barn	**0.8**	0.3	**0.8**	0.4	+0.23
bedu	0.6	0.5	0.6	0.5	-0.01
beer	0.5	0.5	0.4	0.5	-0.03
bier	0.6	0.5	0.6	0.5	+0.05
blij	0.5	0.4	0.5	0.5	-0.03
borg	0.9	1.1	0.9	1.0	-0.14
eext	0.3	0.6	0.3	0.6	-0.13
emsh	**0.8**	0.2	**0.8**	0.2	+0.37
enge	0.6	0.3	0.6	0.4	+0.11
ganz	0.6	0.6	0.5	0.7	-0.06
hare	0.5	0.7	0.5	0.7	-0.14
heil	0.5	0.7	0.5	0.7	-0.14
hoog	0.5	0.5	0.4	0.5	-0.02
kolh	**1.1**	**1.2**	**1.2**	**1.1**	+0.11
leer	**1.1**	0.2	**1.1**	0.3	+0.56
midl	0.5	0.6	0.5	0.6	-0.07
nor3	0.4	**1.1**	0.4	**1.1**	-0.54
nsch	0.7	0.6	0.7	0.6	+0.04
oldo	0.7	0.4	0.7	0.4	+0.2
oosw	0.7	0.5	0.7	0.6	+0.05
ranu	0.6	0.5	0.5	0.6	+0.05
rdn1	**0.8**	0.2	**0.8**	0.2	+0.37
sapp	0.5	0.7	0.4	0.7	-0.1
schw	0.4	0.6	0.4	0.7	-0.12
stil	0.5	0.6	0.5	0.6	-0.02
uith	0.6	0.4	0.6	0.4	+0.12
warf	0.6	0.5	0.6	0.5	+0.05
wtnl	0.6	0.5	0.6	0.5	+0.04
zldv	0.5	0.6	0.5	0.6	-0.04

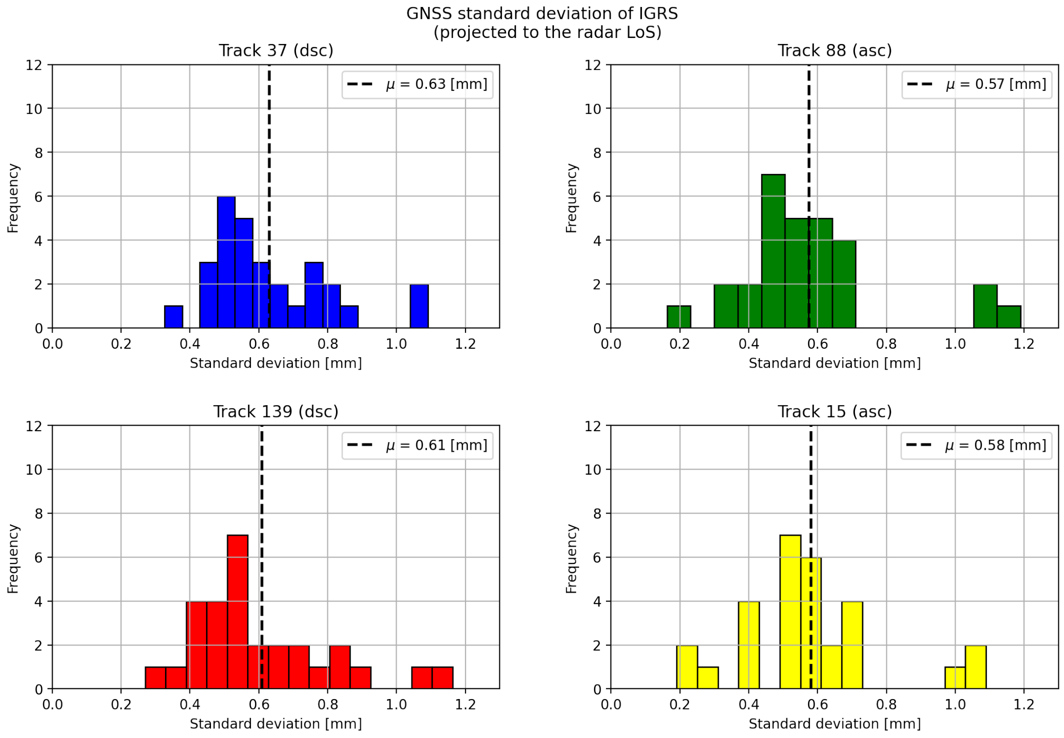

Figure 4.1: Quality of GNSS position estimates. These histograms show the standard deviation of the projected to the LoS GNSS position estimates on each processed satellite track.

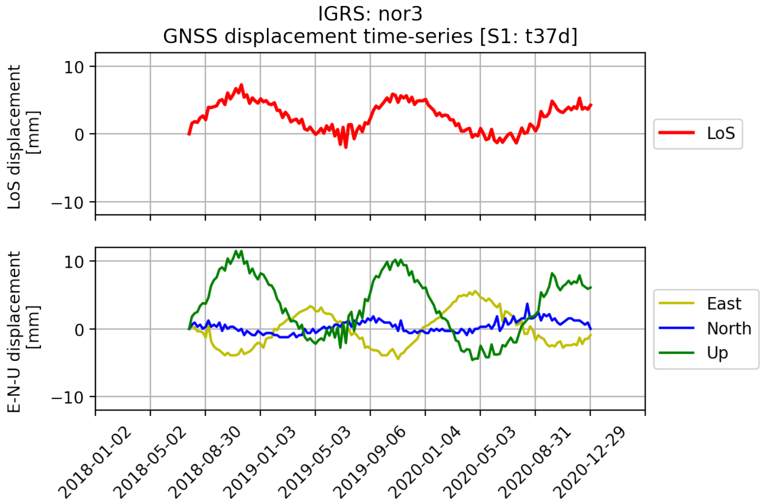

Figure 4.2: East, north, up and LoS time-series data for station **NOR3**. In this figure we can observe the high seasonality which is present both at vertical and at the horizontal directions.

In the bottom of the plot, we can see the e, n, u components plotted. For these time-series, the elevation of the first epoch of the available observations is used as a reference. It is shown that there is seasonality in this signal. More specifically, the station appears to have an upward-westward movement in summer months and the opposite movement in winter, while seasonality is also noted in the north-south direction. This was expected since the station lays very close to an active underground gas storage field, as seen in Figure 4.3. During summer, natural gas for which there is less demand is injected into the reservoir. Therefore, the IGRS is moving upwards and tilting westwards for more than 10 mm. During winter gas is extracted so the station is moving downwards and tilting eastwards.

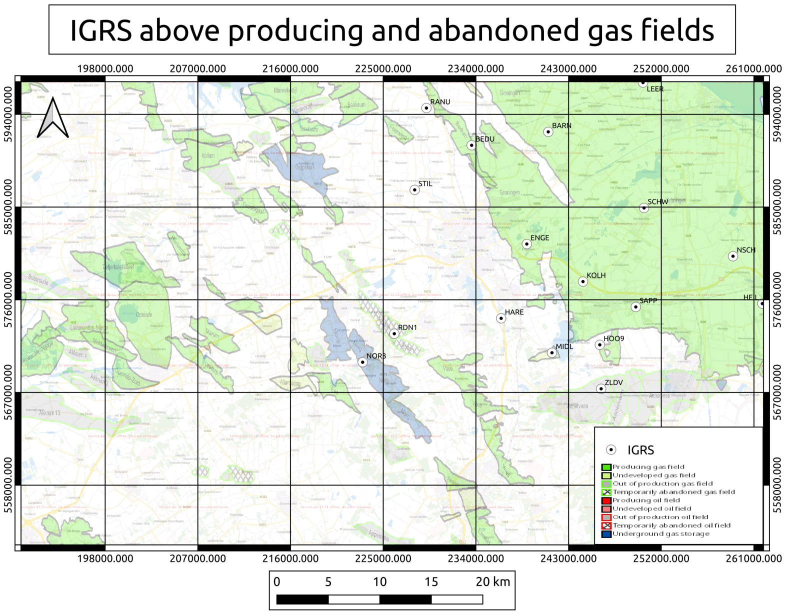

Figure 4.3: Groningen gas field. This map shows part of the gas field in the broader Groningen area depicted with green, together with gas storage facilities depicted with blue. We see that station **NOR3** is on top of an active underground gas storage facility, while station **RDN1** is over a temporarily abandoned gas field.

A similar behavior can be seen for station **RDN1**. Its time-series is shown in Figure 4.4. In this case, the magnitude of the seasonal signal is less, not more than 7–8 mm. This is because station **RDN1** is further away of the underground gas storage field. What is also different than station **NOR3**, is that station **RDN1** is moving upwards-eastwards in summer instead of upwards-westwards like **NOR3** does. Since the gas field is located in between the two stations, see Figure 4.3, when filled with gas, a displacement in opposite directions (eastwards and westwards) will occur for the two stations.

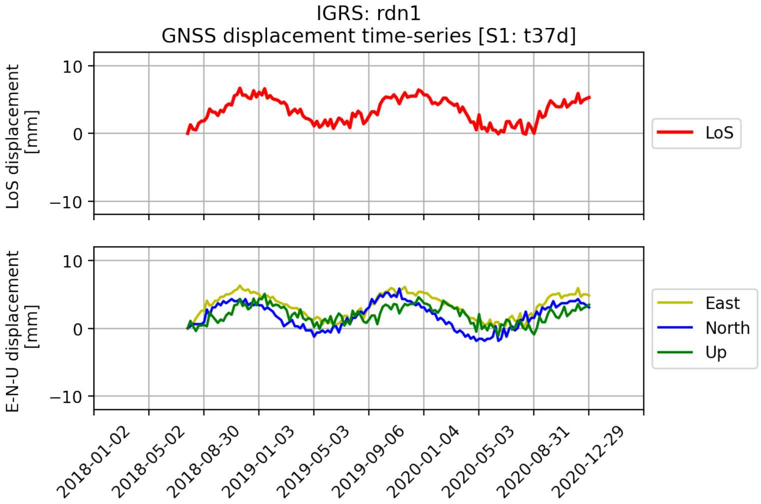

Figure 4.4: East, north, up and LoS time-series data for station **RDN1**. This figure shows the seasonal displacement of station **RDN1**.

Another find was that a high covariance between the e, u components of the coordinates of the stations, see Table 4.1, influences the quality of the GNSS position estimates in different ways. More specifically, when a high positive covariance was found between the e, u components of the coordinates of the stations, we noticed that the standard deviation amplifies in the descending tracks and reduces in the ascending tracks. On the contrary, when a high negative covariance was found, the standard deviation amplifies in the ascending tracks and reduces in the descending tracks.

Finally, station **KOLH** is the only one showing over-millimeter precision in all tracks. The time-series of this station is shown in Figure 4.5. This station shows a high seasonal signal in the northern-southern and in the eastwards-westwards direction but in the upwards-downwards direction a very different behavior is observed.

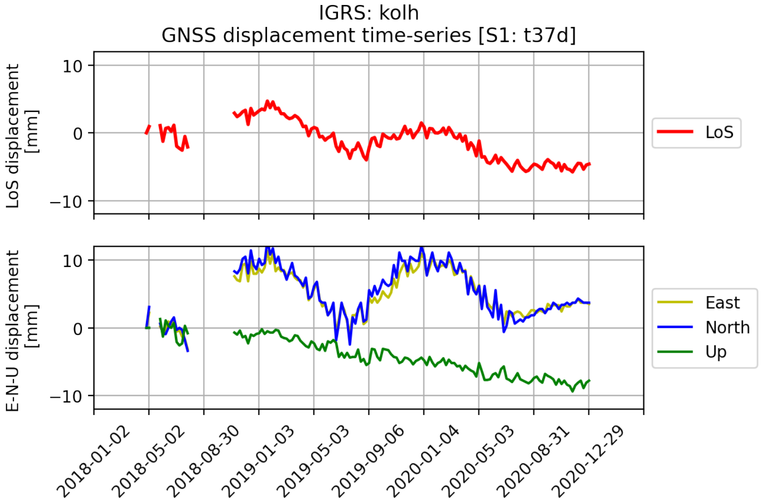

Figure 4.5: East, north, up and LoS time-series data for station **KOLH**. This station is experiencing a different behaviour from the other stations, most likely due to lateral forces acting on the concrete platform base plate. After an intervention on 26 June 2020, when a buffer zone was established, the station stabilizes (Piening, 2021).

Most likely, the observed behaviour is due to lateral pressure from the horizontal pavement onto the side of the concrete platform on which the IGRS is positioned, see Figure 4.6. This pressure may be a consequence of thermal expansion of the pavement material, and in June 2020 a buffer zone was established around the station (Piening, 2021). What is important for this project is that, apparently, the quality estimates (i.e., the stochastic model) of the GNSS results is influenced by the displacements (i.e., the functional model). In other words, there is a leakage of signal from the functional to the stochastic model.

Figure 4.6: Potential lateral forces working on the concrete base plate of the platform of station **KOLH**, e.g. due to thermal expansion of the pavement structures. After an intervention on 26 June 2020, when a buffer zone was established, the station stabilized (Piening, 2021).

4.1.2. Quality of InSAR position estimates

For the InSAR observations, the estimates obtained for the quality of each IGRS can be seen in Table 4.2 and the relevant histograms are shown in Figure 4.7. The IGRS have a relatively stable amplitude and a low phase dispersion. For this reason, the Normalized Amplitude Dispersion was used as an approximation of the quality of the InSAR position estimates. An alternative that could have been used is the Signal-to-Clutter Ratio. We preferred to use the NAD since the stations were positioned at low clutter locations (i.e., concrete plates) and thus, the estimation of the clutter would not have been representative for other projects with different clutter conditions.

In Table 4.2, we can see that almost all InSAR position estimates show a sub-millimeter precision, except station **STIL** on the ascending tracks. Most likely this happened because vegetation was covering this reflector for a few months within the study period, resulting in lower reflection from the reflector, thus, a higher value for the standard deviation of the amplitude time-series, which is used to compute the standard deviation (see Eq. (2.12). In general, the estimates seem to have slightly better precision when compared with the GNSS LoS equivalent. This means that where IGRS are available we could have InSAR measurements with a quality that is at least equal if not even better than the ones coming from the GNSS, albeit in only one direction and in a relative sense. Yet, this is an important result and proves that the corner reflectors are able to reach the sub-millimeter accuracy according to their specifications as it was found by Patel (2020).

Table 4.2: InSAR position estimates quality. In this table we can find the InSAR position estimates quality of all the IGRS, based on the Normalised Amplitude Dispersion, per satellite track.

	t37 (dsc)	t88 (asc)	t139 (dsc)	t15 (asc)
Station	σ_{InSAR} [mm]	σ_{InSAR} [mm]	σ_{InSAR} [mm]	σ_{InSAR} [mm]
barn	0.5	0.4	0.3	0.6
bedu	0.5	0.5	0.4	0.5
beer	0.5	0.4	0.4	0.4
bier	0.4	0.4	0.3	0.5
blij	0.5	0.3	0.7	0.4
borg	0.8	0.6	0.6	0.7
eext	0.4	0.5	0.5	0.7
emsh	0.5	0.3	0.4	0.4
enge	0.5	0.5	0.8	0.7
ganz	0.5	0.5	0.4	0.5
hare	0.4	0.4	0.4	0.6
heil	0.7	0.3	0.3	0.5
hoog	0.4	0.4	0.3	0.5
kolh	0.4	0.7	0.4	0.7
leer	0.4	0.3	0.4	0.4
midl	0.4	0.3	0.3	0.5
nor3	0.5	0.3	0.3	0.5
nsch	0.4	0.4	0.4	0.4
oldo	0.4	0.3	0.3	0.5
oosw	0.6	0.4	0.4	0.4
ranu	0.5	0.4	0.5	0.7
rdn1	0.3	0.3	0.3	0.4
sapp	0.4	0.4	0.3	0.5
schw	0.5	0.3	0.3	0.5
stil	0.6	**1.1**	0.9	**1.1**
uith	0.4	0.5	0.4	0.4
warf	0.4	0.3	0.3	0.5
wtnl	0.7	0.5	0.5	0.5
zldv	0.4	0.3	0.3	0.6

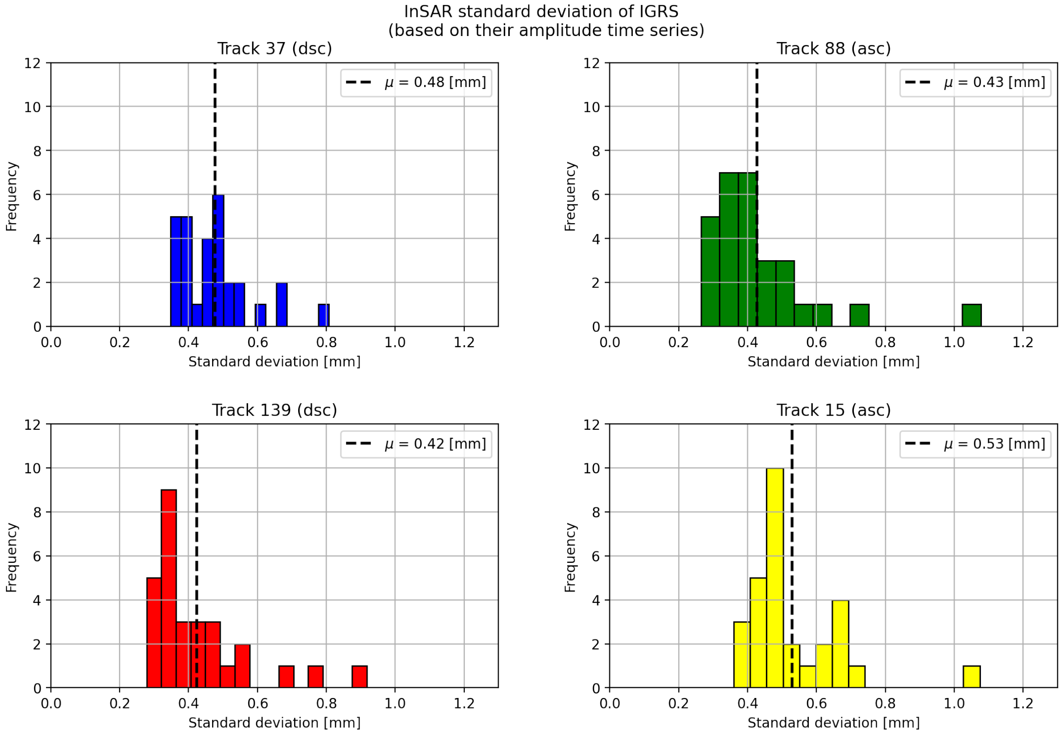

Figure 4.7: Quality of InSAR position estimates. These histograms show the standard deviation of the InSAR position estimates for each processed satellite track.

4.2. Performance of the InSAR functional model

With 29 IGRS available in the AOI, hence 58 corner reflectors, we were able to form a network of arcs, connecting each station with all the others. Having 29 stations, this yields 406 arcs per satellite track. This can be seen schematically in Figure 4.8. By using data from four different satellite tracks (two descending and two ascending) there are 4 × 406 = 1624 arcs that we can compare individually. Obviously, these arcs are not independent, as they share common stations. Yet, each arc has its own unique position, length, and orientation, and therefore a unique atmospheric signal component that we wish to evaluate. The distribution of the arc lengths is shown in Figure 4.9. The lengths of the arcs range from 4.13 km to 51.41 km, having a mean value of 24 km.

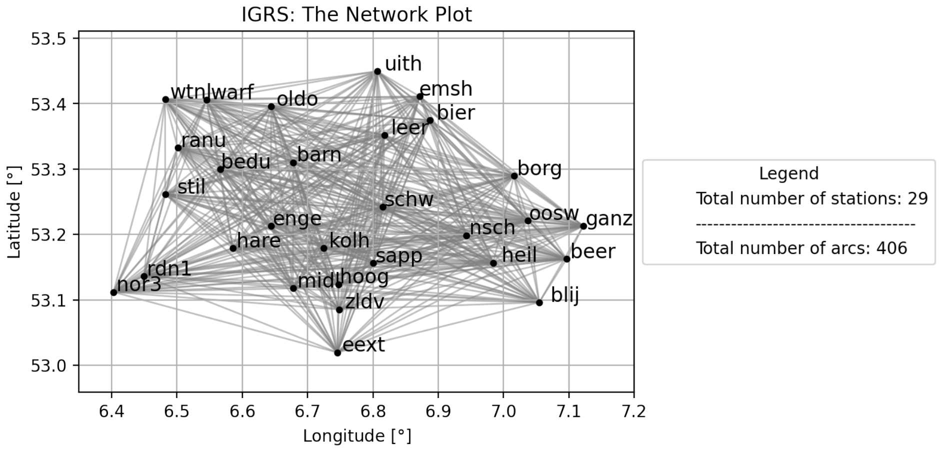

Figure 4.8: The IGRS network. This graph shows all the available arcs per satellite track. All the arcs that are formed are already showing the high density of the available data.

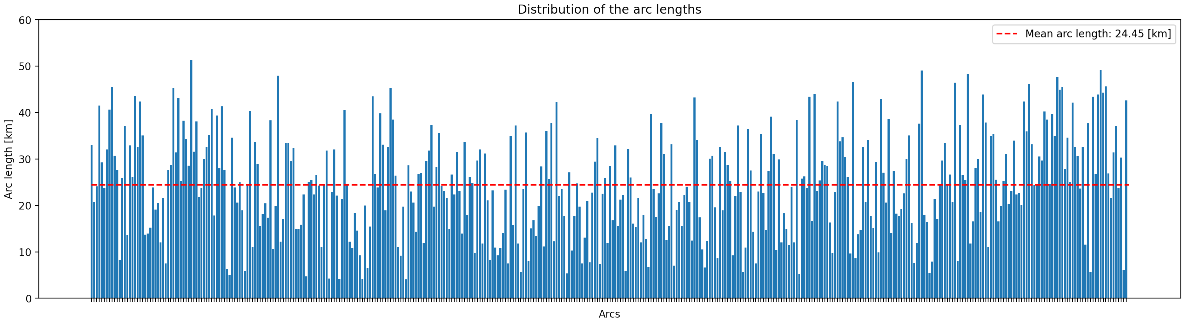

Figure 4.9: The distribution of the arc lengths. This graph shows the length of all the arcs formed in the network. Their mean value is depicted with a red horizontal dashed line.

With the IGRS being designed to serve as benchmarks for both the GNSS and the InSAR techniques, it is expected that any GNSS double-difference arc formed by two stations would give the same time-series with the respective InSAR double-difference arc of the same two stations. With several other parameters (e.g. temperature and atmosphere) and noise influencing the estimates, the InSAR and GNSS time-series can only agree up to the level of the precision of the techniques. In order to compare between the InSAR and the GNSS observations we computed the residuals from their double-differenced observations as

$$\text{Residuals} = DD_{\text{InSAR}} - DD_{\text{GNSS}}, \tag{4.1}$$

where DD_{InSAR} is the double-difference between the InSAR observations and DD_{GNSS} is the double-difference between the GNSS observations.

We can see an overview of the residuals between the results of the two techniques for track 37 in Figure 4.10. For the other three tracks, the residuals look similar and the corresponding plots can be found in Appendix C.

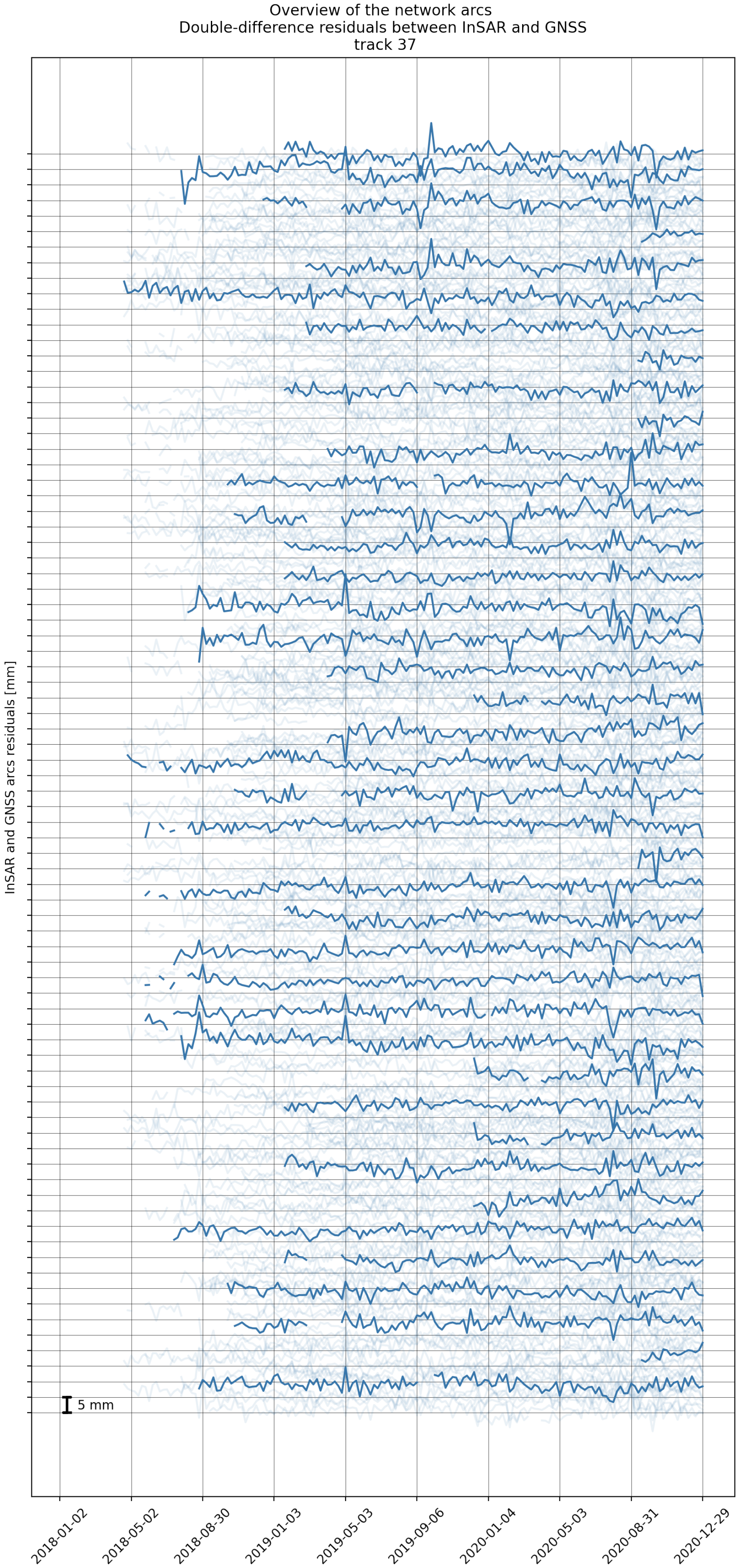

Figure 4.10: Residuals between InSAR and GNSS time-series of all 406 arcs, track 37. Here we see an overview of the time-series of the difference between InSAR and GNSS observations for all 406 arcs of the IGRS network. For visualization purposes only some of the arcs are plotted in blue, while others are depicted with a transparent grey color. We can observe that the residuals between the InSAR and the GNSS observations exceed the level of precision of the techniques.

In Figure 4.10, in order to have a better overview, only some of the arcs are plotted in blue, while the rest are shown in the background in an almost transparent grey color. It is clear from this plot that all the time-series deviate from zero and the residuals exceed the level of precision of the techniques. Some arcs indicate a seasonal signal to be present and some show outliers which appear as spikes. The treatment of these outliers is discussed in section 4.3, with the hypothesis testing.

When discussing the seasonality, we need to focus mainly on two stations; **NOR3** and **RDN1**. For this, we can look at one very indicative arc, between **NOR3** and **BIER**. Figure 4.11 shows that this seasonal effect is indeed captured by the GNSS results, while in the InSAR observations this effect is missing.

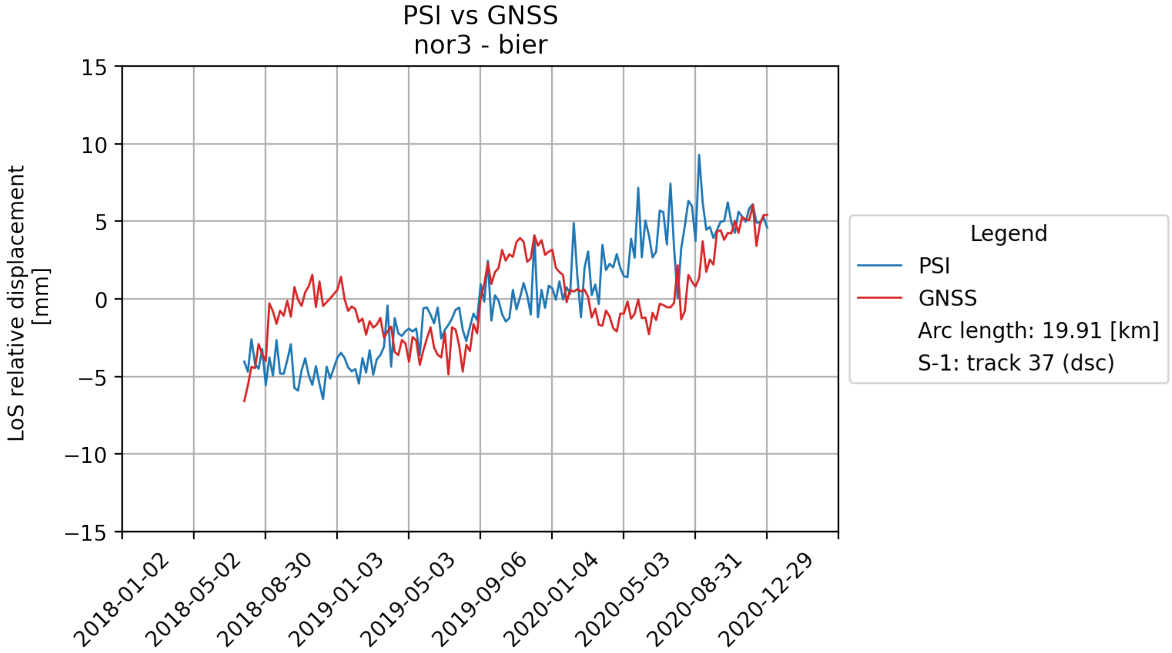

Figure 4.11: InSAR and GNSS double-difference arc comparison between **NOR3** and **BIER**. Here we see that the seasonal signal is captured by the GNSS but not by InSAR.

We know that the IGRS are designed to measure the same target. The periodicity is missing in one of the two techniques, so this initiated an investigation in the InSAR functional model to see where the differences are coming from.

In Figure 4.12a, the Atmospheric Phase Screens computed for every image in the stack of the descending track 37 are shown. The APS estimation is a very critical step in the application of interferometric synthetic aperture radar techniques (Chen et al., 2021). The APS is showing the residuals between the observed and the estimated interferometric phase. The estimated phase is modeled by a linear fit in time, under the assumption of a displacement rate which is constant in time. So in other words, Figure 4.12a shows the estimated atmospheric contribution in the interferometric signal. The area covered is around 60 × 60 km and the values run from $-\pi$ to π. The colors of this plot indicate the atmospheric phase delay between all the points in the image. For example, between two points depicted with blue in the image, there is a 2π atmospheric delay. In order to see the IGRS distribution over the AOI, a map depicting the area (around 60 × 60 km) over which the APS is computed can be seen in Figure 4.12b.

Increased attention should be given to Figure 4.13. This figure depicts the Atmospheric Phase Screens that are computed for track 37 from 2018-09-23 to 2018-11-16. It can be observed that a big red bulb appears in almost all screens at the south-west part of the AOI, indicating that the atmospheric behavior over this area remains rather stable over a two-month period. In other words, this states that the atmosphere is correlated over time around this area for two months. This cannot be true, based on the atmosphere's turbulent and random nature. Time-series analysis methods have proven successful in mitigating turbulent atmospheric signals and such methods assume that the Atmospheric Phase Screen is random in time (Jolivet et al., 2014). In an attempt to explain this, we can look back to Figure 4.11. The dates corresponding to the temporally correlated atmosphere match with the dates where the GNSS results are showing a strong uplift of station **NOR3**, due to the injection of gas in the storage facility. Also, when looking at the map with the IGRS locations

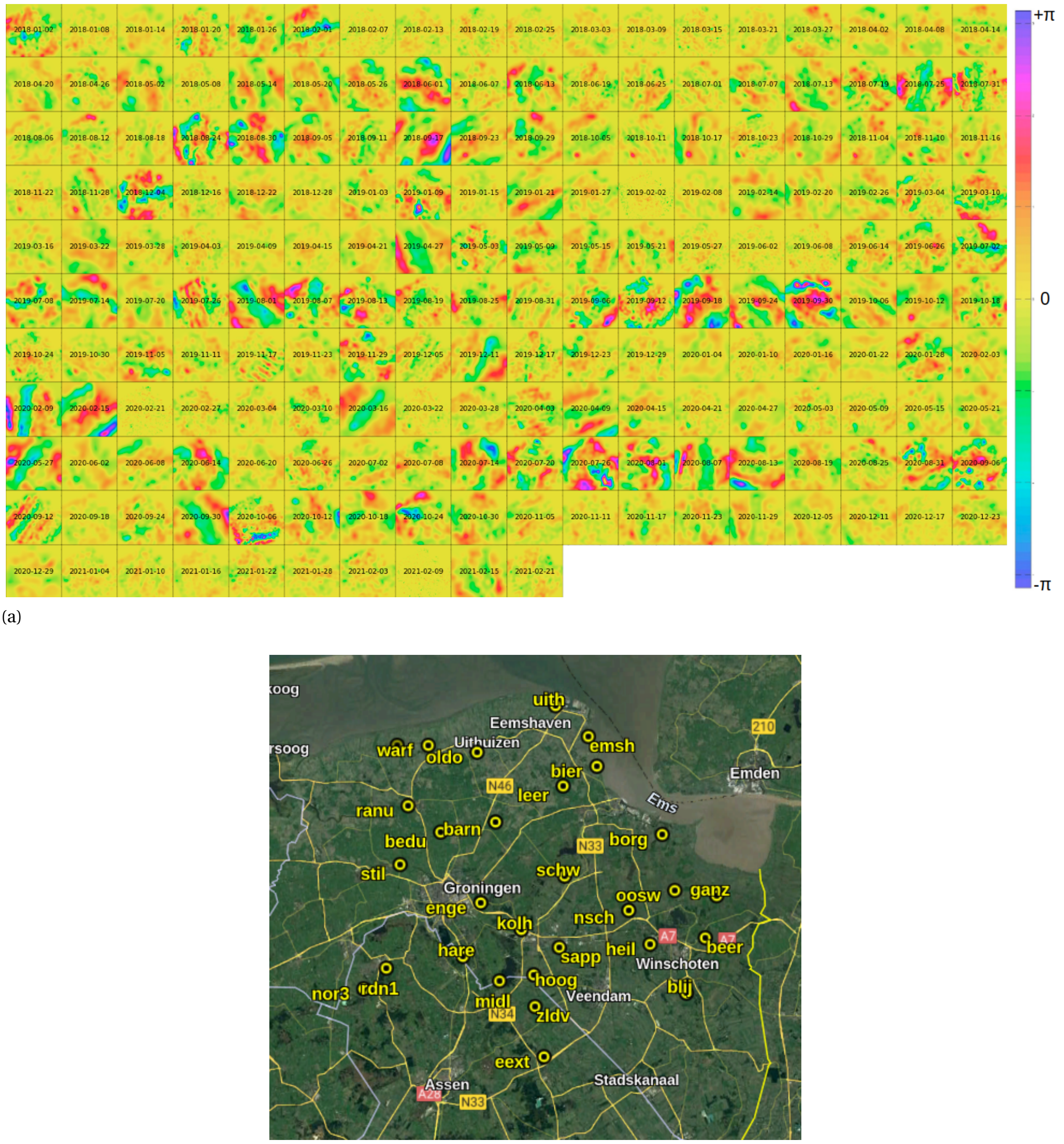

(a)

(b)

Figure 4.12: Atmospheric Phase Screens, track 37. In (a) we see the APS computed for track 37 from 2018-01-02 to 2021-02-21. The APS show the atmospheric contribution to the interferometric signal. The area covered is around 60 × 60 km and the values run from $-\pi$ to π. In (b) we see the IGRS distribution over the same area.

(Figure 4.12b), it proves that the area that seems to experience a correlated atmosphere over time is indeed over station **NOR3**, one of the two stations involved in the arc shown in Figure 4.11. With this analysis, it is now evident that there is a "leakage" of the true signal in the atmospheric estimation of the PSI algorithm. In other words, the PSI algorithm did not properly estimate the atmospheric contribution and falsely added some of the physical signal to the atmosphere.

In this case, with most of the stations being above the active Groningen gas field, a seasonal signal was expected, since big quantities of gas are being extracted during the winter months. Because the GNSS signal already showed a seasonal behavior over other areas as well, this led us to exclude these areas from the atmospheric estimation of the PSI algorithm. The areas excluded are depicted in red in Figure 4.14. Besides the western part of the AOI, another area at the east is excluded from the atmospheric estimation. This area

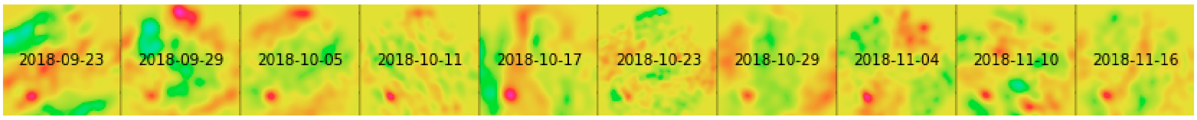

Figure 4.13: Atmospheric Phase Screens: 2018/09/23 - 2018/11/16, track 37. Here we see that the atmosphere appears to be correlated over time, since the red bulb at the south-west part of the image is not changing over time.

is closest to the stations **HEIL**, **BEER**, **NSCH**, **OOSW**, **GANZ**. For the atmospheric estimation step of the PSI processing, this means that the algorithm did not select any points within the designated areas to estimate the atmospheric effects. Since a linear model assuming a constant displacement rate over time is used to compute the modeled phase, we decided not to estimate the APS on network points in the areas that are mostly showing a seasonal displacement behavior [1]. After the estimation is computed for all other points, an interpolation is used to compute the Atmospheric Phase Screen over the entire image. It should be noted that this may improve the estimation of the APS in some cases, but it may also produce large interpolation errors over the areas that are excluded from the estimation. The Atmospheric Phase Screens computed for the dates discussed before are shown in Figure 4.15, compared with the estimation before excluding any areas. The atmosphere does not show any correlation over time anymore.

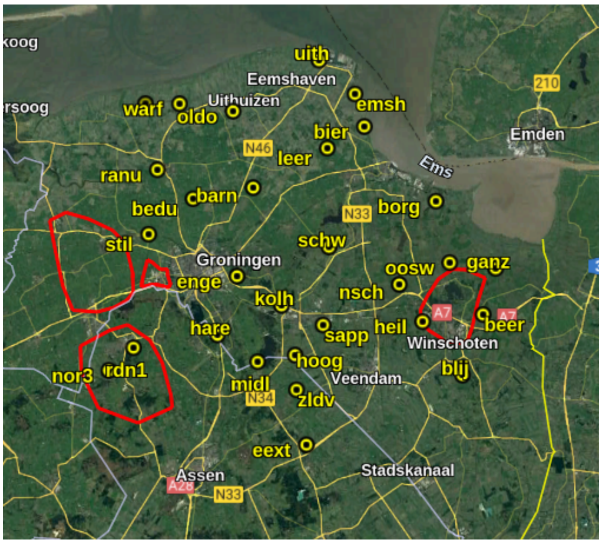

Figure 4.14: Areas excluded from the atmospheric estimation. In this map the reader can see the areas depicted in red which are excluded from the atmospheric estimation of the PSI algorithm, since an atmospheric "leakage" was detected.

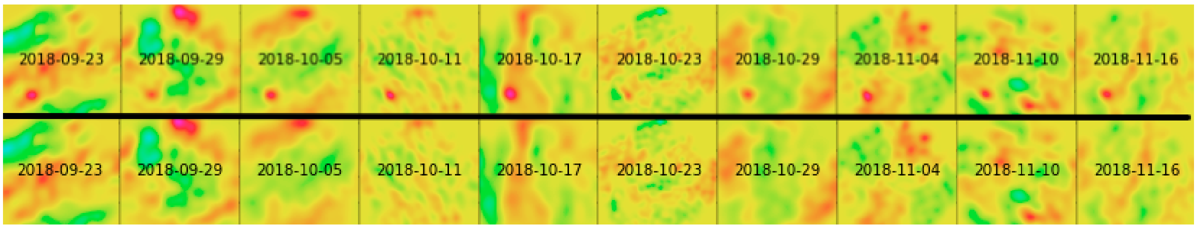

Figure 4.15: Atmospheric Phase Screens: 2018/09/23 - 2018/11/16, track 37. At the top we see the APS before excluding any areas from the estimation and at the bottom we see the APS after excluding the areas depicted with red in Figure 4.14. It is clear that after the "guided" PSI algorithm run, the area that showed an atmospheric correlation over time is now uncorrelated.

The result for the InSAR and GNSS comparison for this specific arc (**NOR3**- **BIER**) after this change in the atmospheric estimation is shown in Figure 4.16. The results show now a better agreement of the two techniques, with the InSAR results also depicting a seasonal signal. In this case, excluding an area that has

---

[1] Perhaps, a better approach would be to estimate the APS on the network points in the areas that are mostly showing a seasonal displacement behavior with a different model (i.e., Gaussian), not assuming a constant displacement rate over time.

a strong seasonal signal involved, helped the PSI algorithm to better estimate the true signal, but this might lead to large interpolation errors in other cases.

A similar issue was found to be present also in track 139, the other descending track used in this project. What we found after processing data from four satellite tracks is that, while in the two descending tracks there is a strong leakage of the atmospheric signal in the atmosphere, in the two ascending tracks this is not present. In general, the ascending tracks (88 and 15) appear to have a more turbulent atmosphere, but an atmospheric correlation over time is not present. The APS estimation of these tracks can be seen in Appendix D.

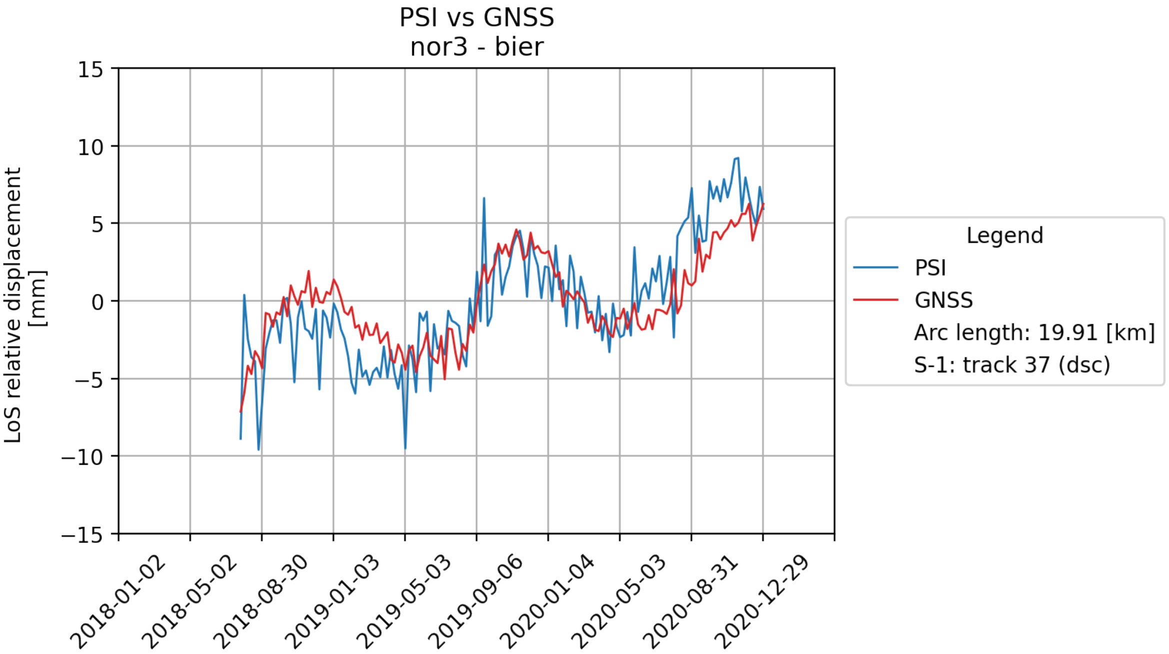

Figure 4.16: Result with the "guided" PSI algorithm. This plot shows the InSAR and GNSS arc comparison between stations **NOR3** and **BIER** after some areas are excluded from the APS estimation.

4.3. Hypothesis testing

After obtaining the results that are corrected for the atmospheric flaw, we need to develop a robust methodology to assess the level of agreement between the InSAR and the GNSS results of the IGRS. For this, we perform an Overall Model Test, where we hypothesize that

$$DD_{\text{InSAR}} = DD_{\text{GNSS}}, \tag{4.2}$$

where DD_{InSAR} is the vector of double-differences for one arc of the InSAR observations, and DD_{GNSS} is the vector of double-differences for the same arc of the GNSS observations. In other words, the null hypothesis is that an arc (in time and space) of InSAR double-difference displacement estimates and an arc of GNSS double-difference displacement estimates over the same epochs and the same stations will show identical results. This assumption is valid to begin with, since this is the main purpose of the IGRS.

In order to perform the Overall Model Test per arc we need to decide on the significance level α. This refers to the probability of incorrectly rejecting the null hypothesis, when it is in fact true. For a significance level of 5% in order to be on the conservative side the critical value is $K_\alpha = 3.841$, as obtained from the relevant F-distribution table.

We used four satellite tracks (two ascending and two descending), but here we are showing the one which shows the best agreement between the two techniques. Figure 4.17a shows the arcs that pass the Overall Model Test depicted in green and Figure 4.17b shows the arcs that don't pass the test depicted in red. In this case 85% of the observations pass the statistical testing, since 59 out of the 406 observations have a test statistic which is greater than the critical value. In these results, the areas depicted in red in Figure 4.14 were excluded from the estimation of the Atmospheric Phase Screens in the PSI analysis, before the hypothesis testing.

Since some observations fail to pass the Overall Model Test, the next step is to investigate the cause of these failures. From Figure 4.17, it is not exactly clear which stations are involved in the most of the arcs that fail to pass the test, besides **NOR3** and **RDN1**. For this reason, a bar plot is created, showing the number of times that a particular station is involved in failing arcs, see Figure 4.18. Stations **NOR3** and **RDN1** are involved in most of the failing arcs; i.e., 22 out of the 28 arcs from **NOR3** and 14 out of the 28 arcs from **RDN1**.

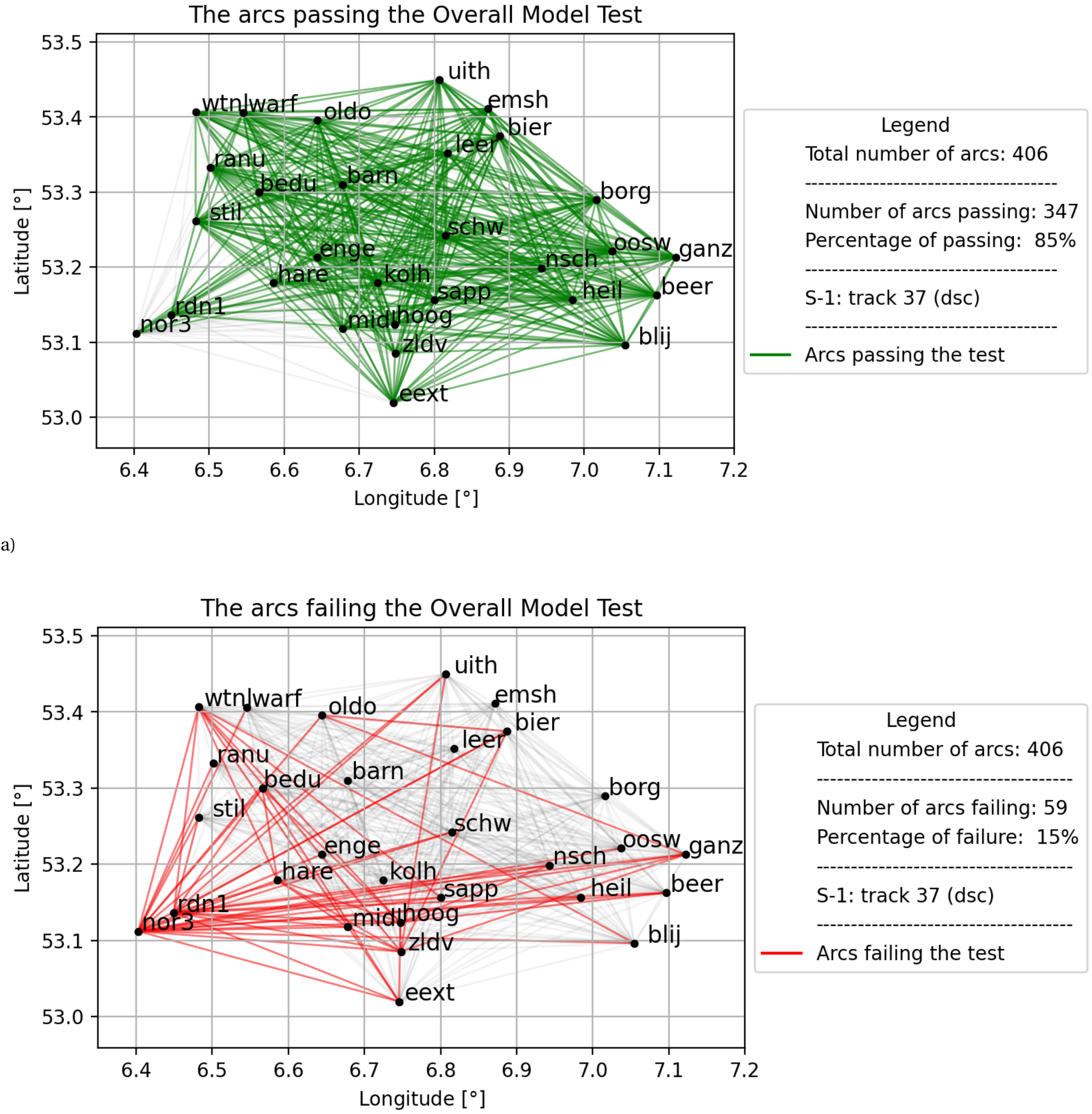

(a)

(b)

Figure 4.17: Arcs passing (a) and failing (b) the OMT, track 37. In this figure we can see all the observations which have a test statistic lower (top figure) and higher (bottom figure) than the critical value. This shows that several rejected arcs are related to a few specific IGRS.

In order to have a better understanding of the spatial characteristics of the problem, the same result can be seen in a spatial plot, in Figure 4.19, showing the magnitude of involvement of each IGRS in the failing arcs: larger symbols indicate more failing arcs. The biggest dots refer to **NOR3** and **RDN1**, because as seen before, these stations are indeed involved into many arcs that fail to pass the hypothesis testing. This plot shows that most of the failing arcs are located to the south-western part of the AOI, close to stations **NOR3** and **RDN1**. Again, these stations are the ones related to the underground gas storage facility and therefore subject to significant seasonal variability. This explains the seasonality that is being observed. This area was excluded from the estimation of the Atmospheric Phase Screens and this might have caused large interpolation errors.

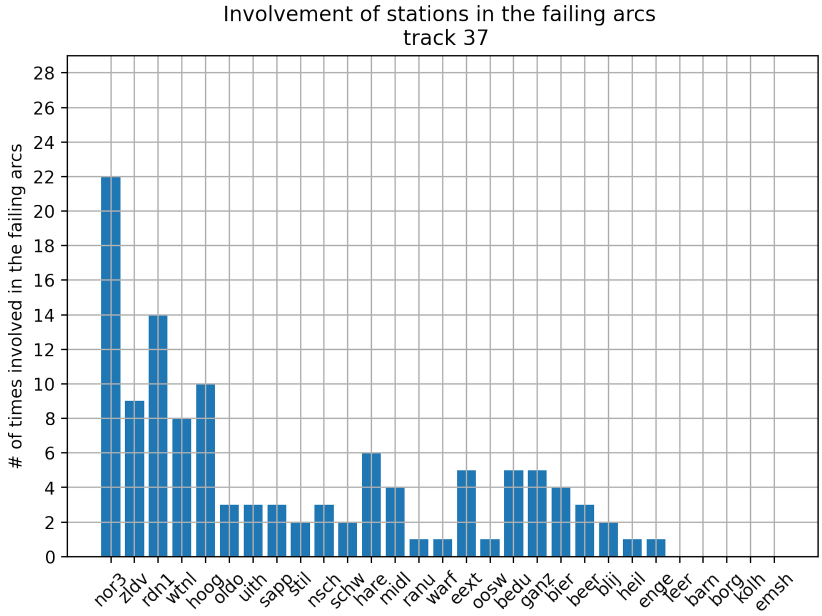

Figure 4.18: Involvement of the stations in failing arcs, track 37. This plot shows how many times each IGRS is involved into observations that have a larger test statistic than the critical value.

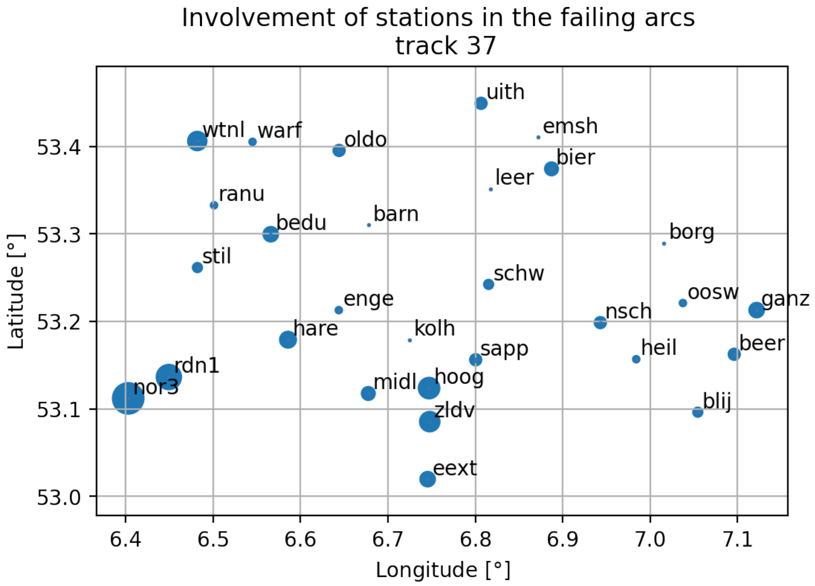

Figure 4.19: Spatial plot for the involvement of the stations in failing arcs, track 37. In this plot, the biggest dots refer to **NOR3** and **RDN1**, because these stations are involved into most of the arcs that fail to pass the hypothesis testing.

While investigating the arcs that failed to pass the Overall Model Test, it is also important to discuss the stochastic model that has been used. In Figure 4.20 we can see the arcs that failed the test being classified by their standard deviations. The arcs that have a standard deviation less than 1 mm are shown in black (23 out of 59), the arcs that have a standard deviation larger than 1 mm but less than 1.2 mm are shown in blue (21 out of 59) and the arcs with greater standard deviation are depicted with an orange color (15 out of 59). What becomes clear is that out of all the arcs that fail to pass the test, most of them are the ones which have a smaller standard deviation.

One other thing to discuss is the influence of outliers. In some cases, one single erroneous measurement

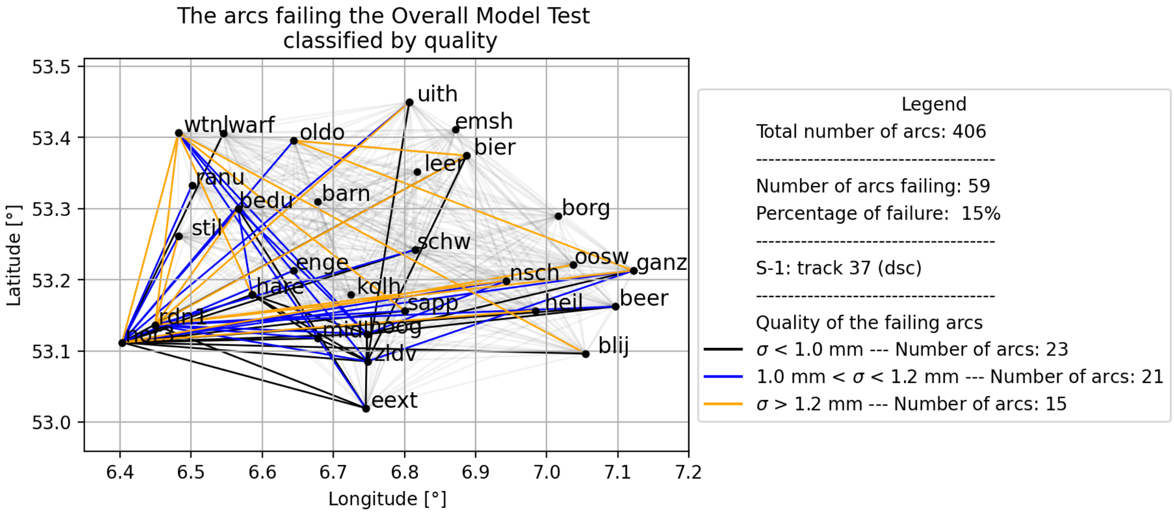

Figure 4.20: The arcs failing to pass the OMT classified by quality. This plot shows how many arcs have failed and what qiality they have.

within the time series may have a strong impact on the result of the Overall Model Test. For example, if one of the radar acquisitions suffers from a system malfunction or the GNSS observation faced a sudden unexpected incident or if the atmospheric residuals are very large in one specific epoch, then this arc may be categorised as one that failed to pass the test, leading to a more general statement about disagreement in the results. This is illustrated in Figure 4.21. This plot shows the InSAR double-difference arc in blue and the GNSS double-difference arc in red. There is a certain epoch where the InSAR time-series experiences a sudden jump of about 8 mm. For this arc, the test statistic T is larger than the critical value K_a, so the Overall Model Test is rejected.

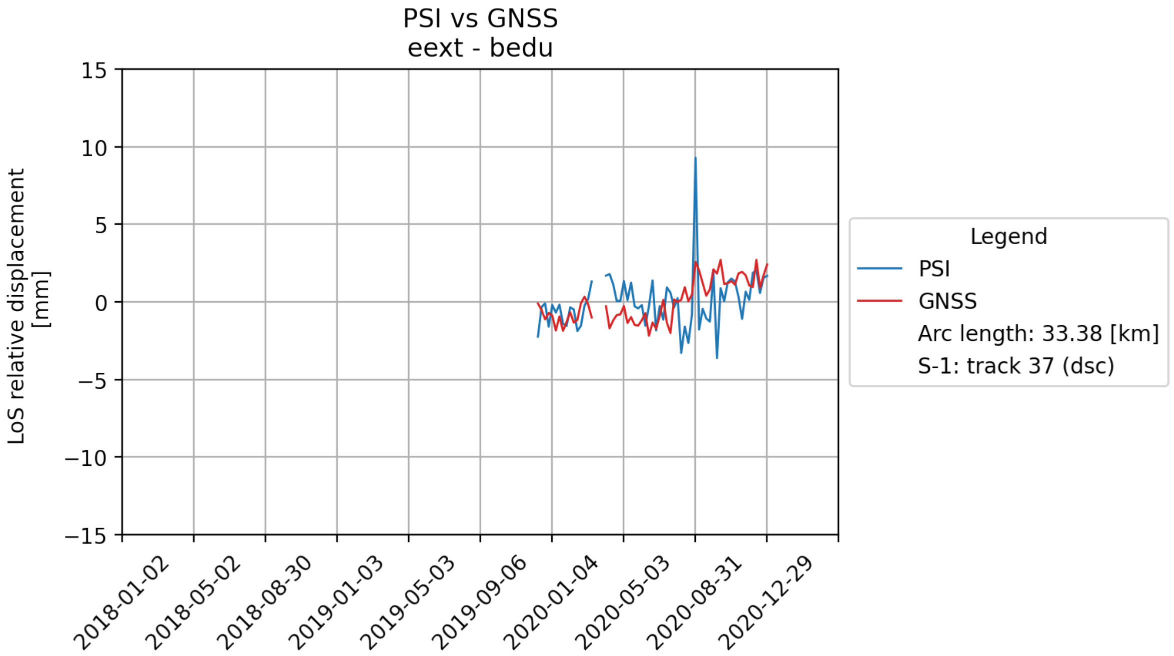

Figure 4.21: Time-series with one outlier. This time-series plot shows the effect of one outlier in the outcome of the Overall Model Test.

For this reason we decided to perform a w-test on all observations. This is a way to screen through all the epochs on every arc and do an outlier detection. We computed one normalized residual for each epoch in every arc. We decided to disregard up to 5% of data for the longer time-series available which are characterised as outliers from each arc. Then we did again an Overall Model Test with the remaining data. This decision was mainly based on the fact that some of the images in each stack seem to be affected by large atmospheric effects as seen in their Atmospheric Phase Screens computed. The results for track 37 can be seen in Figure 4.22. It is shown through the second OMT peformed that by only disregarding a small percentage of the worst data, there is a 96% level of agreement between the two techniques. In fact, the observations that still don't pass the hypothesis testing are almost all including arcs from station **NOR3**. Figure 4.23 clearly shows this in a bar plot.

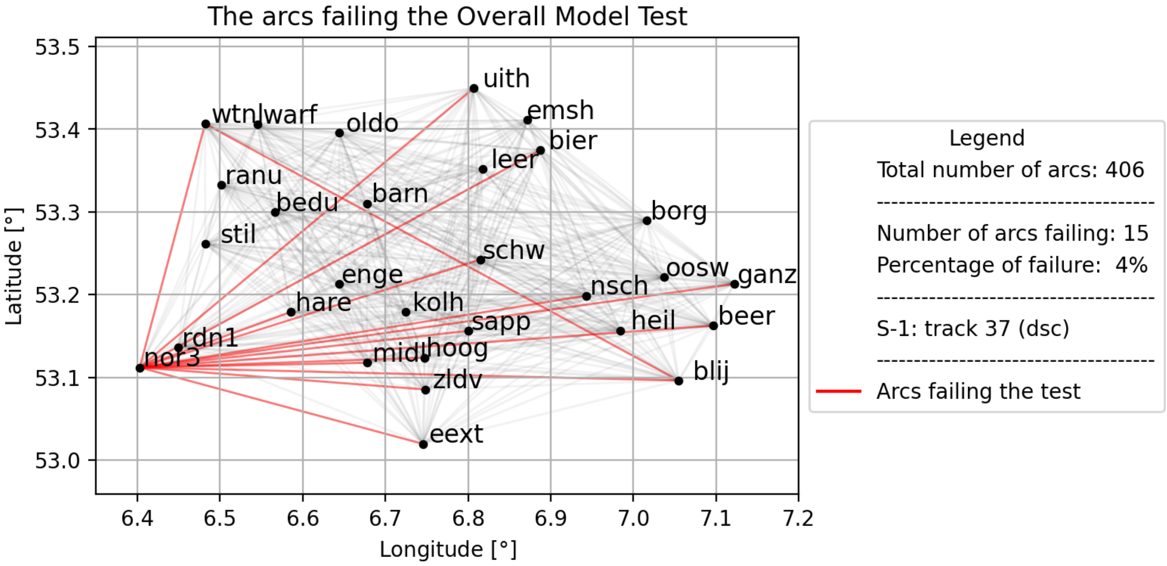

Figure 4.22: The arcs failing to pass the OMT after removing the worst results from the dataset, track 37. This plot shows that the percentage of the observations failing the OMT decreases if the worst observations are disregarded.

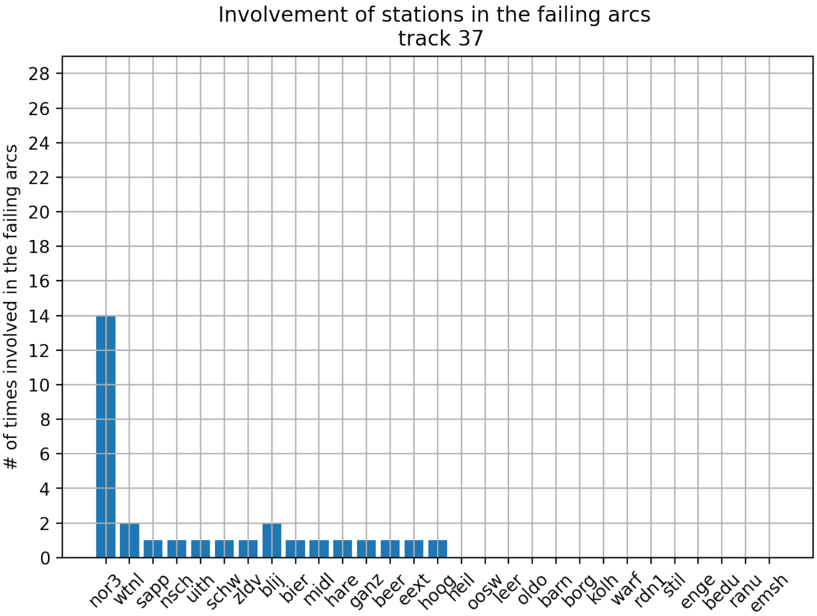

Figure 4.23: Involvement of the stations in failing arcs after removing the worst results from the dataset, track 37. This plot clearly shows the influence of the outliers to the results of the OMT.

In order to have an overview of the values that were computed from the w-test, we visualize all of them using a mesh grid. The result for track 37 can be seen in Figure 4.24. This plot shows in color all the absolute w values computed for all the arcs. The arcs are sorted based on the amount of epochs that both IGRS spanning the arc were active. The binary graph on the right hand side helps to connect the w-values with the stations involved in each arc.

We can observe a pattern with high (red) values of the normalized residuals around July 2020. For station **WTNL**, it appears that almost all arcs are having very high w values on certain epochs around September 2019 but also September 2020.

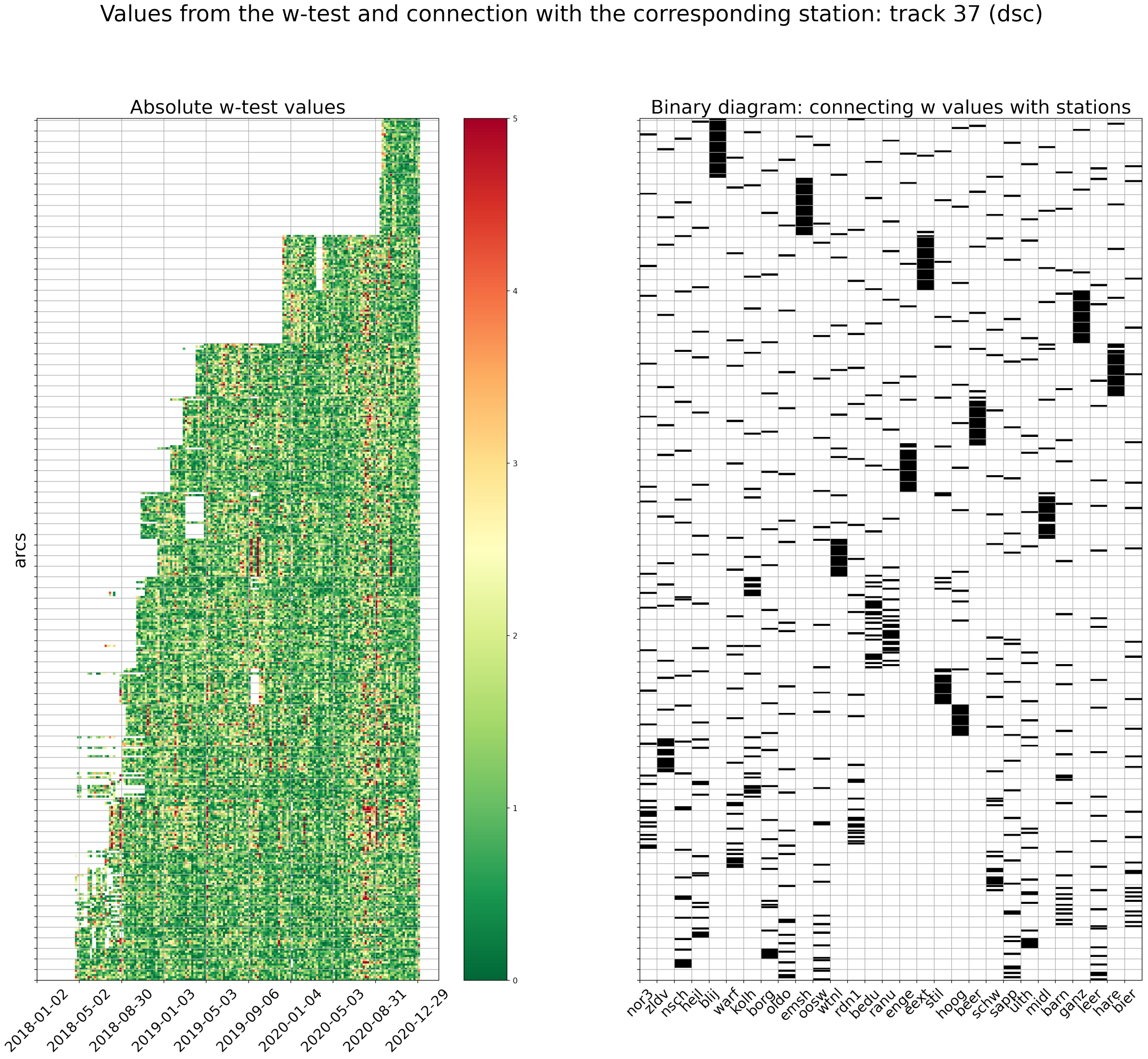

Figure 4.24: Plot with the w-test values for track 37. This graph, on the left hand side shows a mesh grid with the absolute value of the w-test and on the right hand side it shows in a binary diagram which stations are involved in each arc.

The results for the ascending track 88 are shown in Figure 4.25. They seem to be more noisy, but we can also observe patterns, especially in the bottom of the plot, where the most high (red) values appear. These values seem to have a repeating cycle, starting with red, followed with green. By using the binary graph on the right hand side we associate these high values with mainly two stations, **NOR3** and **RDN1**. This shows that for these two stations that have shown the biggest seasonality trends, the values that came out of the w-test show that the signals measured with InSAR and the signals measured with GNSS still show a disagreement. Similar patterns can also be spotted on the other two tracks used (139 and 15), whose relevant plots can be found in Appendix E.

These findings allow us to draw conclusions on the level of agreement between the results of GNSS and InSAR. In general, it shows that the results between the two techniques can reach a high level of agreement. With this methodology developed we show that with the use of IGRS, InSAR and GNSS observations can show similar results. Still, there are cases where the InSAR and the GNSS results are not in agreement. A disagreement between the results of the two techniques is mainly related with observations in which stations **NOR3** and **RDN1** involved. One explanation for this is that this is an area which was excluded from the atmospheric estimation in the PSI algorithm. The atmospheric residuals near these stations are interpolated with values from the surroundings and probably the interpolation error is so large that it still influences the end result, forcing these arcs to still fail the OMT. Another explanation for this disagreement is that because of the relatively large seasonal horizontal displacement that these stations face, the functional model designed for the comparison of the two techniques is not adequate. In other words, since the GNSS receiver is positioned higher than the corner reflector, when an IGRS is tilting, it will experience a larger motion, which is not accounted for in the functional model. One idea in order to take this tilting into account is to add a scaling factor in the functional model, for the stations that face large horizontal displacements. This is further discussed in chapter 5, which summarizes the conclusions of this project and includes recommendations for further developing this work.

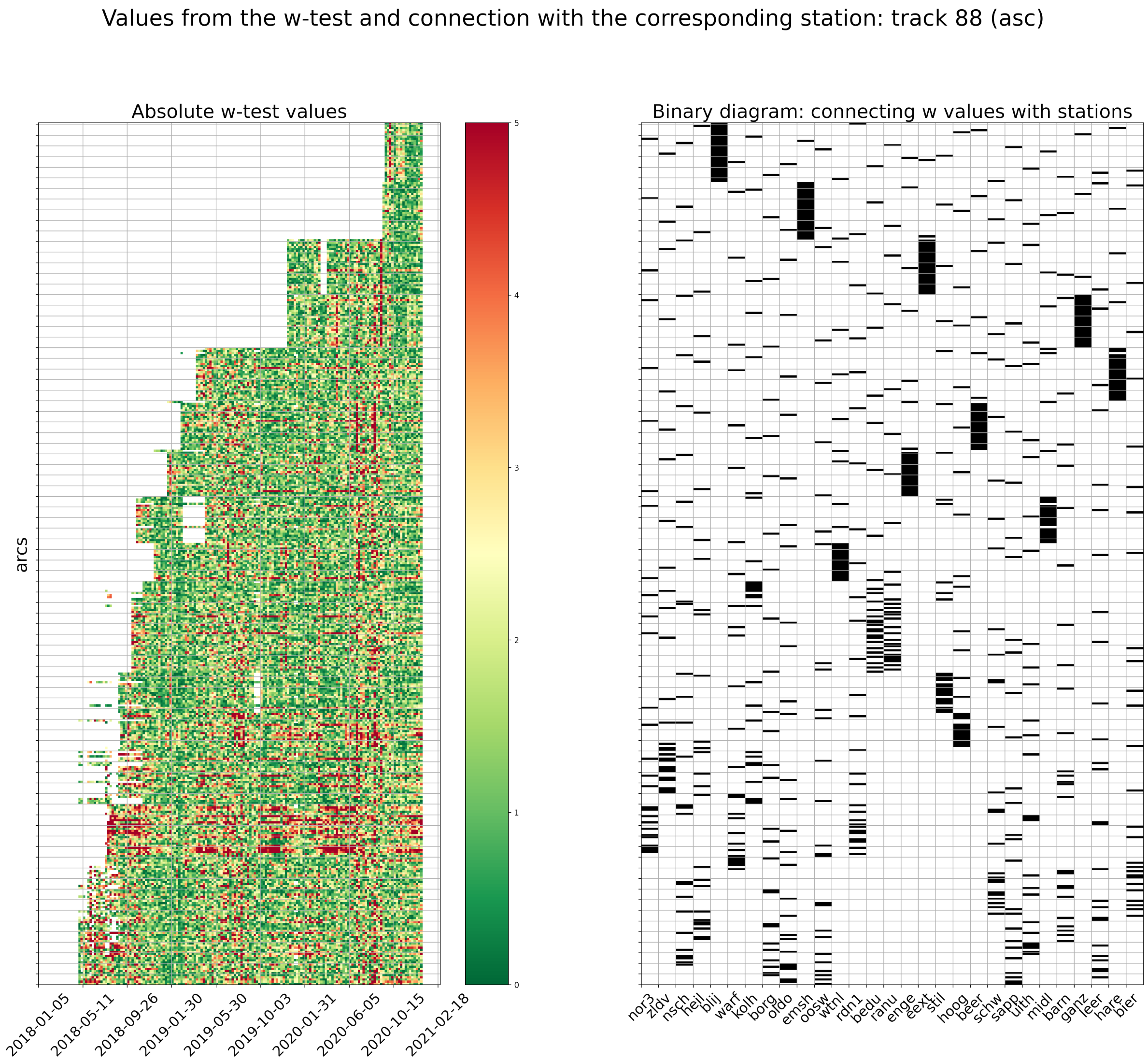

Figure 4.25: Plot with the w-test values for track 88. This graph, on the left hand side shows a mesh grid with the absolute value of the w-test and on the right hand side it shows in a binary diagram which stations are involved in each arc.

5

Conclusions and Recommendations

This chapter includes the conclusions that we drew from this project, together with recommendations for improving the results and further work.

5.1. Conclusions

The main research objective of this thesis is to answer the following question:

How can we prove the efficacy of the IGRS to connect different geodetic datums from InSAR and GNSS estimates, using empirical data acquired from a network of IGRS?

In this study we developed a methodology to assess the level of agreement between the InSAR and the GNSS results of the IGRS and also evaluated the precision of the two geodetic techniques when data from a network of IGRS are used.

For the InSAR data the Normalized Amplitude Dispersion was used as an approximation of their quality. We decided to use this metric over the Signal-to-Clutter Ratio, since the stations were positioned at low clutter locations (i.e., concrete plates) and thus, the estimation of the clutter would not have been representative for other studies which would use the same instruments but with different clutter conditions. Using the NAD we found a sub-millimeter precision for almost all IGRS in all processed tracks. These results showed that the quality of the InSAR position estimates are in line with the predicted (design) performance of the corner reflectors, as described in their design and installation study.

For the quality of the GNSS position estimates their variance-covariance matrices were used. In order for these matrices to be computed, the annual and semi-annual effect of the signal have been removed. The error statistics were assumed to be stable over all the epochs. An important finding is that apparently, the precision estimate of the periodically moving stations is worse than the non-periodically moving stations. Hence, the quality estimates (i.e., the stochastic model) of the GNSS results are influenced by the displacements (i.e. the functional model). Thus, the GNSS results show leakage of signal from the functional to the stochastic model.

The first thing revealed when comparing the results of the InSAR and the GNSS observations is that the IGRS can be used as a preliminary indicator for flaws in the algorithms used to process the data. In this case, the InSAR and the GNSS results that were firstly generated were significantly different for a number of stations. In the GNSS time-series we could clearly see seasonal signal effects, while the respective InSAR time-series were significantly different in some cases. The collocated IGRS observations unveiled these discrepancies and, in this study, helped us to make the necessary adjustments on the PSI algorithm, regarding the atmospheric estimation. More specifically, there was leakage of signal from the functional to the stochastic model and that was because a linear fit under the assumption of a constant displacement rate in time was used to estimate the atmospheric contribution in the signal, while in this area strong seasonal signals are present. Thus, we can conclude that more attention should be given to the functional model of the InSAR. In this case, regarding the estimation of the Atmospheric Phase Screens, a different model (i.e., Gaussian) without assuming a constant displacement rate in time might have been more adequate.

With the established methodology it is possible to make a quantitative comparison in the observation space, between the InSAR and GNSS results, towards proving that these techniques are measuring the same deformation signals. It was shown that the results of the techniques can reach a very high level of agreement, up to 96% when the worst 5% of the data are disregarded. We should not forget that the atmospheric estimation was differently treated for some areas within the AOI and this may lead some of the observations to still fail the test. Besides this, we also showed that some of the IGRS, like station **NOR3** and station **RDN1**, experience a high seasonal signal, not only in the up direction, but also in the east and north directions. The GNSS receiver is in a higher position than the radar corner reflector so it is possible that in these cases like station **NOR3** and station **RDN1**, where there is high horizontal displacement (i.e., up to 10 mm) in the east and north directions, the GNSS results are more affected than the InSAR results. In other words, the functional model used is not adequate for these observations, since it does not take into account the tilting behavior of the IGRS.

What is more, proving that InSAR and GNSS are indeed measuring the same signal is of vital importance. The greatest benefit is that through the use of the IGRS, it is possible to provide an absolute geodetic reference for an InSAR analysis. In other words, incorporating an IGRS corner reflector as a Persistent Scatterer with known absolute position in a Terrestrial Reference Frame, will make the rest of the Persistent Scatterers of the analysis to have an absolute reference. Thus, the IGRS will serve as a foundation for integrating InSAR measurements in an absolute geodetic datum. In this way, the concept of transforming the datum-free InSAR displacement time-series estimates into an absolute geodetic datum is possible.

5.2. Recommendations

This section includes recommendations for improving the results and for further work.

At first, it is highly recommended to develop a radar-coding algorithm for the automatic detection of an IGRS in a PSI dataset. In this study, due to lack of time, a sub-optimal way was used for this task, i.e., manually identifying the point for which the highest values in the amplitude time-series were observed. This required some manual labor and doesn't allow for the project to scale-up. In other words, in order for the same analysis to be performed with data from other sensors or data from a different area the radar-coordinates of the IGRS should be found through a radar-coding algorithm.

Regarding the precision estimates of the GNSS results, it was found that they are influenced by the displacement of the stations. In other words, the stochastic model of the GNSS results is influenced by the functional model, i.e., the GNSS results show leakage of signal from the functional to the stochastic model. Thus, attention should be given to way the error statistics for the GNSS position estimates are computed.

Besides this, it is important to improve the functional model used in the PSI processing. In this study, for the atmospheric estimation a linear model was used, assuming a constant displacement rate over time. Since there were large seasonal effects in the data this approach caused some of the signal to "leak" into the atmospheric contribution. It is therefore recommended to use a different model for the atmospheric estimation. For instance, a Gaussian model could be used (instead of a linear one), without assuming a constant velocity (i.e., stable displacement rate) through time.

What could also be improved is the functional model developed for the comparison of the results. In order to compare between the InSAR and the GNSS results, we developed a simple model, computing the differences of their time-series. We observed that for some stations (e.g., **NOR3**, **RDN1**) besides the up-down displacement there is also significant movement (up to 5 mm) in the other directions (i.e., east-west and north-south). In Figure 5.1, for a horizontal movement of 5 mm (i.e., from point A to point B, disregarding the curvature of the Earth) and taking into account the length of the IGRS pole (2.40 m) the tilt angle θ can be computed as: $\theta = (5/2400) \times (180/\pi) = 0.1°$. Assuming that the IGRS only translates and does not rotate might not be a valid assumption. For example, for station **NOR3** which has a tilt angle of 0.1°, using a scaling factor in the function model to account for the fact that the GNSS results are more affected than the InSAR results might be a more optimal choice.

One of the most important next steps is to perform a geodetic datum connection. This study proved the efficacy of the IGRS to connect different geodetic datums from InSAR and GNSS estimates. In InSAR, the position and the displacement of the scatterers are relative. With the IGRS available, it is possible to express the (virtual) center of each scatterer in a geodetic datum. This would make the interpretation of the InSAR results much easier and will allow for an absolute InSAR analysis.

Finally, a comparison of more geodetic techniques will be also valuable. In this project the effort was focused to make the comparison between the InSAR and the GNSS results. Deformation mechanisms can also be studied by other techniques for which the IGRS can serve as a benchmark. For instance, repeated leveling and/or repeated Airborne Laser Scanning could also contribute to deformation studies. In this AOI there are already available both leveling data and the AHN3 dataset. It is also recommended to experiment

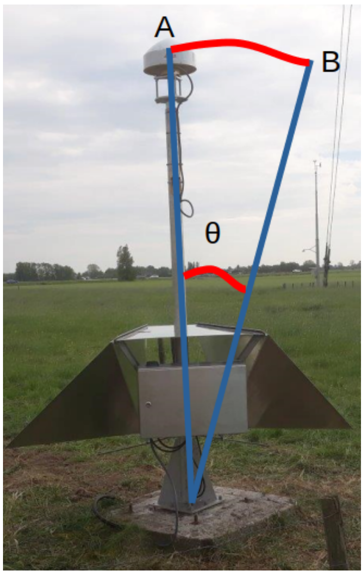

Figure 5.1: Tilt angle of the IGRS. Here we see the tilt angle θ that forms when the IGRS is experiencing horizontal movement.

with data from different satellite sensors. This study used satellite data only from ESA's satellite Sentinel-1. Two ascending (88 and 15) and two descending (37 and 139) tracks were used. For the same AOI, RADARSAT-2 and TERRASAR-X data are available. There is a possibility to investigate whether the results improve if different sensors are used.

Bibliography

Brouwer, W. (2021). An analysis of the InSAR displacement vector decomposition. Master's thesis, Delft University of Technology, Delft.

Carter, W. E., Shrestha, R. L., & Slatton, K. C. (2007). Geodetic laser scanning. *Physics Today*, 60(12), 41.

Chen, Y., Bruzzone, L., Jiang, L., & Sun, Q. (2021). Aru-net: Reduction of atmospheric phase screen in SAR interferometry using attention-based deep residual u-net. *IEEE Transactions on Geoscience and Remote Sensing*, 59(7), 5780–5793.

Czikhardt, R., van der Marel, H., & Papco, J. (2021). Gecoris: An open-source toolbox for analyzing time series of corner reflectors in insar geodesy. *Remote Sensing*, 13(5).

Dentz, F. (2021). personal communication.

Dheenathayalan, P. (2019). *Optimizing the exploitation of persistent scatterers in satellite radar interferometry*. PhD thesis, Delft University of Technology, Delft, the Netherlands.

Dheenathayalan, P., Small, D., Schubert, A., & Hanssen, R. (2016). High-precision positioning of radar scatterers. *Journal of Geodesy*, 90.

Enge, P. K. (1994). The global positioning system: Signals, measurements, and performance. *International Journal of Wireless Information Networks*, 1, 83–105.

Ferretti, A., Prati, C., & Rocca, F. (2000). Analysis of permanent scatterers in sar interferometry. In *IGARSS 2000. IEEE 2000 International Geoscience and Remote Sensing Symposium. Taking the Pulse of the Planet: The Role of Remote Sensing in Managing the Environment. Proceedings (Cat. No.00CH37120)*, volume 2 (pp. 761–763 vol.2).

Hanssen, R. F. (2001). *Radar Interferometry: Data Interpretation and Error Analysis*. Dordrecht: Kluwer Academic Publishers.

Hofmann-Wellenhof, B., Lichtenegger, H., & Collins, J. (1992). *Global Positioning System, Theory and Practice*. Wien: Springer-Verlag.

Hu, F., Wu, J., Chang, L., & Hanssen, R. F. (2019). Incorporating temporary coherent scatterers in multi-temporal InSAR using adaptive temporal subsets. *IEEE Transactions on Geoscience and Remote Sensing*, 57(10), 7658–7670.

Jolivet, R., Agram, P. S., Lin, N. Y., Simons, M., Doin, M.-P., Peltzer, G., & Li, Z. (2014). Improving insar geodesy using global atmospheric models. *Journal of Geophysical Research: Solid Earth*, 119(3), 2324–2341.

Kamphuis, J. (2019). Co-locating geodetic reference points; on the design and performance of an integrated geodetic reference station. Master's thesis, Delft University of Technology, Delft.

Nitti, D. O., Bovenga, F., Morea, A., Rana, F. M., Guerriero, L., Greco, M., & Pinelli, G. (2012). On the use of SAR interferometry to aid navigation of UAV. In C. R. B. Jr., S. P. Mertikas, X. Neyt, C. Nichol, D. Cowley, & J.-P. Bruyant (Eds.), *Remote Sensing of the Ocean, Sea Ice, Coastal Waters, and Large Water Regions 2012*, volume 8532 (pp. 11 – 19).: International Society for Optics and Photonics SPIE.

Oliver, M. A. & Webster, R. (1990). Kriging: a method of interpolation for geographical information systems. *International Journal of Geographical Information Systems*, 4(3), 313–332.

Patel, K. (2020). Performance analysis of conventional and next-generation artificial geodetic radar reflectors. Master's thesis, Delft University of Technology, Delft.

Pepe, A. & Calò, F. (2017). A review of interferometric synthetic aperture radar (insar) multi-track approaches for the retrieval of earth's surface displacements. *Applied Sciences*, 7(12).

Piening, H. (2021). powerpoint document from NAM.

Qin, Y. (2018). *Sentinel-1 Wide Swath Interferometry: Processing Techniques and Applications*. PhD thesis, Lyles School of Civil Engineering, West Lafayette, Indiana.

Teunissen, P. (2009). *Probability and Observation Theory*. Department of Geoscience and Remote Sensing: Delft University of Technology.

Teunissen, P. & Montenbruck, O. (2017). *Springer handbook of global navigation satellite systems*. Springer.

Timmen, L. (2010). Absolute and relative gravimetry. In *Sciences of Geodesy-I* (pp. 1–48). Springer.

Torge, W. & Müller, J. (2012). *Geodesy*. Walter de Gruyter.

van der Marel, H. (2020). *Comparison of GNSS Processing Methodologies for Subsidence Monitoring: NAM GNSS Alternative Processing Method Project*. Technical report, Nederlandse Aardolie Maatschappij.

Van der Marel, H. (2021). personal communication.

van Leijen, F. J. (2014). *Persistent scatterer interferometry based on geodetic estimation theory*. PhD thesis, Delft University of Technology, Delft, the Netherlands.

Wolfgang, J. & Peter, L. S., Eds. (2009). *Gravity Interpretation*. Springer-Verlag Berlin Heidelberg.

Zhou, X., Chang, N.-B., & Li, S. (2009). Applications of sar interferometry in earth and environmental science research. *Sensors (Basel, Switzerland)*, 9(3), 1876—1912.

A

IGRS design and specifications

In this appendix we can find a more detailed description of the IGRS design and specifications. The side and the top view of an IGRS corner reflector can be seen in Figure A.1 and the drawings for the top and the back plate which include the dimensions and specifications of the IGRS can be seen in Figure A.2. Finally, the equations to compute the coordinates of the apex are displayed.

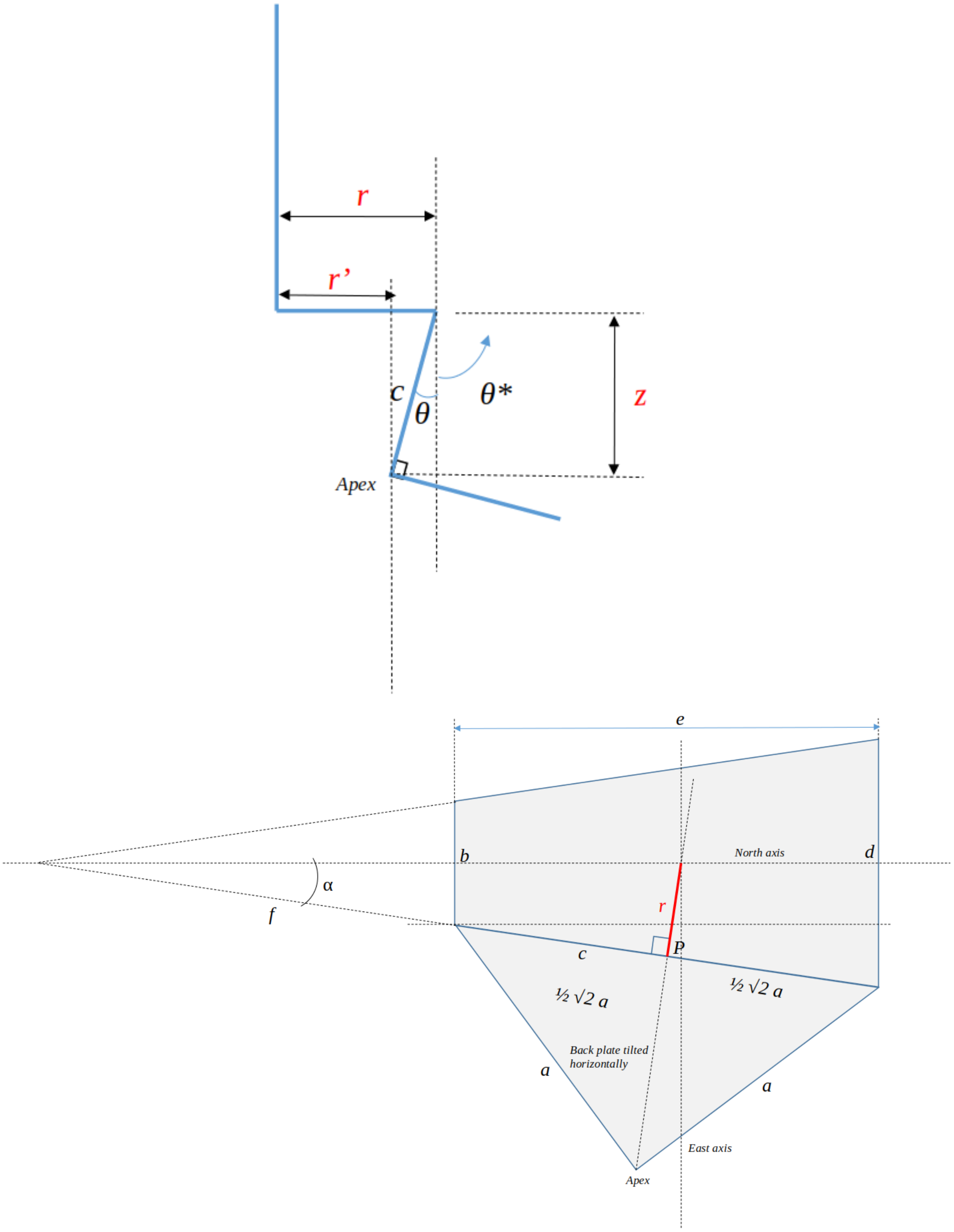

Figure A.1: IGRS side and top view of a corner reflector. In (a) we see the side view of the IGRS. The tilt angle θ is dependent on the maximum Radar Cross Section, the incidence angle of the satellite and the range. In (b) we see the top view of a corner reflector of the IGRS for the northern hemisphere. The horizontal distance r from the body frame origin to the point P is depicted in red.

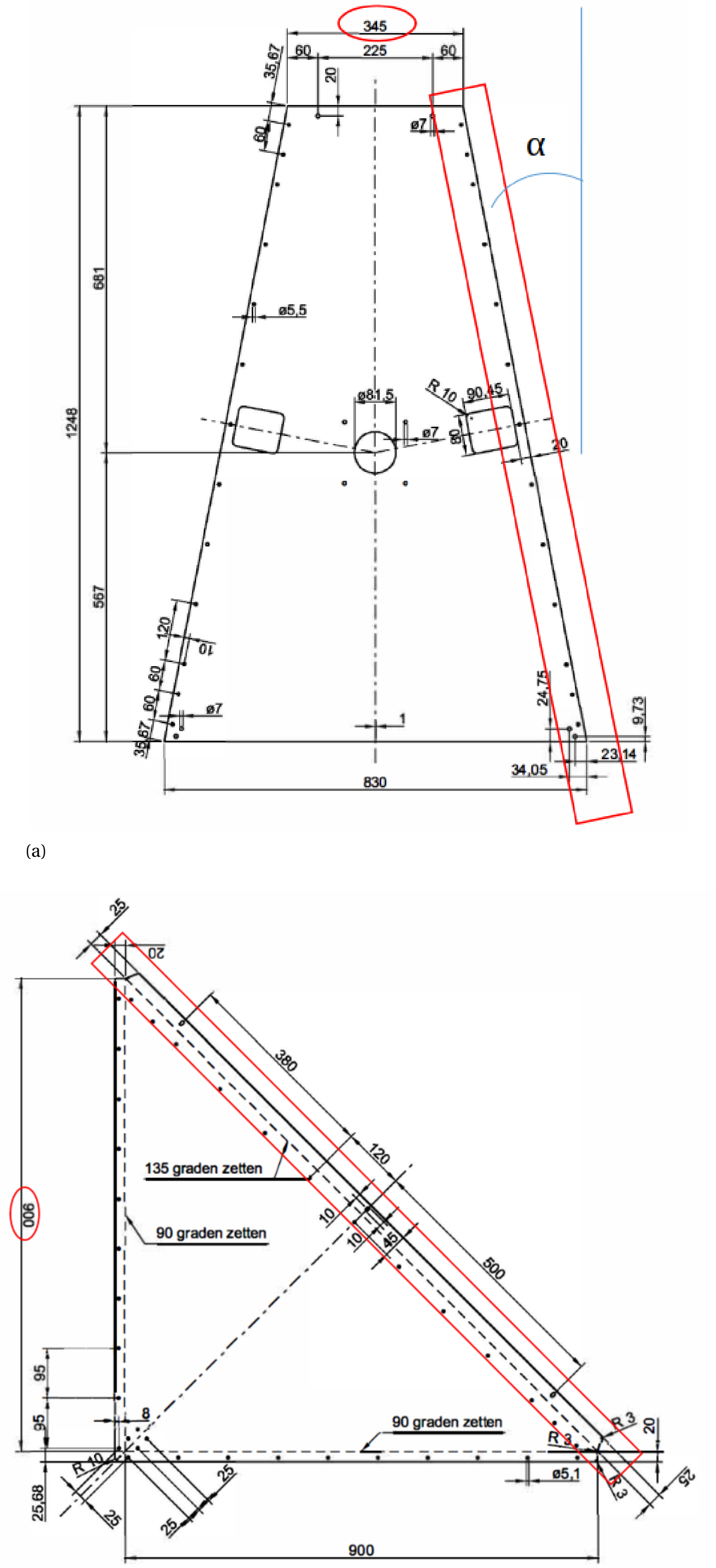

(a)

(b)

Figure A.2: Top and back plate of the IGRS. In (a) we see the top plate of the IGRS. The critical dimensions of the leg of the reflector *a* and the width of the top plate are marked with red. In (b) we see the back plate of the IGRS.

The e, n, u coordinates of the apices in the IGRS body frame are computed as a function of (i) the short size b of the top plate, (ii) the angle α which is the heading angle of the satellite, (iii) the tilt angle θ, related to the maximum Radar Cross Section and the local incidence angle and (iv) the length a of the reflector.

In Figure A.1, r denotes the horizontal distance from the body frame origin to point P and can be computed as

$$r = (f + c)\tan\alpha, \tag{A.1}$$

where

$$f = \frac{b}{\cos\alpha}, \quad c = \frac{1}{2}\sqrt{2}\alpha, \quad \alpha = \arctan\frac{d-b}{2e}. \tag{A.2}$$

The dimensions of the parts are:

- $b = 345$ mm (width of the top plate at the south side)
- $a = 900$ mm (length of the reflector leg)
- $d = 830$ mm (width of the top plate at the north side)
- $e = 1248$ mm (length of the top plate)

Looking at the side view of the IGRS from Figure A.1, we get: $r' = r + \sin\theta$ (for negative θ angles). Then, for the e, n, u components of the coordinates of the apex it is

$$\begin{aligned} e &= +r'\cos\alpha, \\ n &= -r'\sin\alpha, \\ z &= -c\cos\theta. \end{aligned} \tag{A.3}$$

Note that these formulas hold for an eastward-facing reflector, acquiring data from a descending orbit. For a westward-facing corner reflector, acquiring data from an ascending orbit, the equations change to

$$\begin{aligned} e &= -r'\cos\alpha, \\ n &= -r'\sin\alpha, \\ z &= -c\cos\theta. \end{aligned} \tag{A.4}$$

B

IGRS: Amplitude and Displacement plots

In this appendix we can find the amplitude and displacement plots for all the IGRS and for all the processed satellite tracks. From these plots it becomes clear both from the amplitude but also from the phase behaviour when each IGRS is installed. More specifically, after each IGRS installation, the amplitude of the signal on the respective scatterer experiences a "jump" and reaches a value of almost 30 dB in most scatterers. What is more, the LoS displacement which has an irregular behavior, seems to settle with significantly lower variance, in the order of 1-2 mm. The red line in the plots indicates the date of each IGRS installation. In some cases, the amplitude "jump" appears to be slightly before the red vertical line. This happens because the IGRS have already been placed at the location, but without being calibrated. Still, the reflection from the corner reflector is high so the "jump" appears before the operational date of installment.

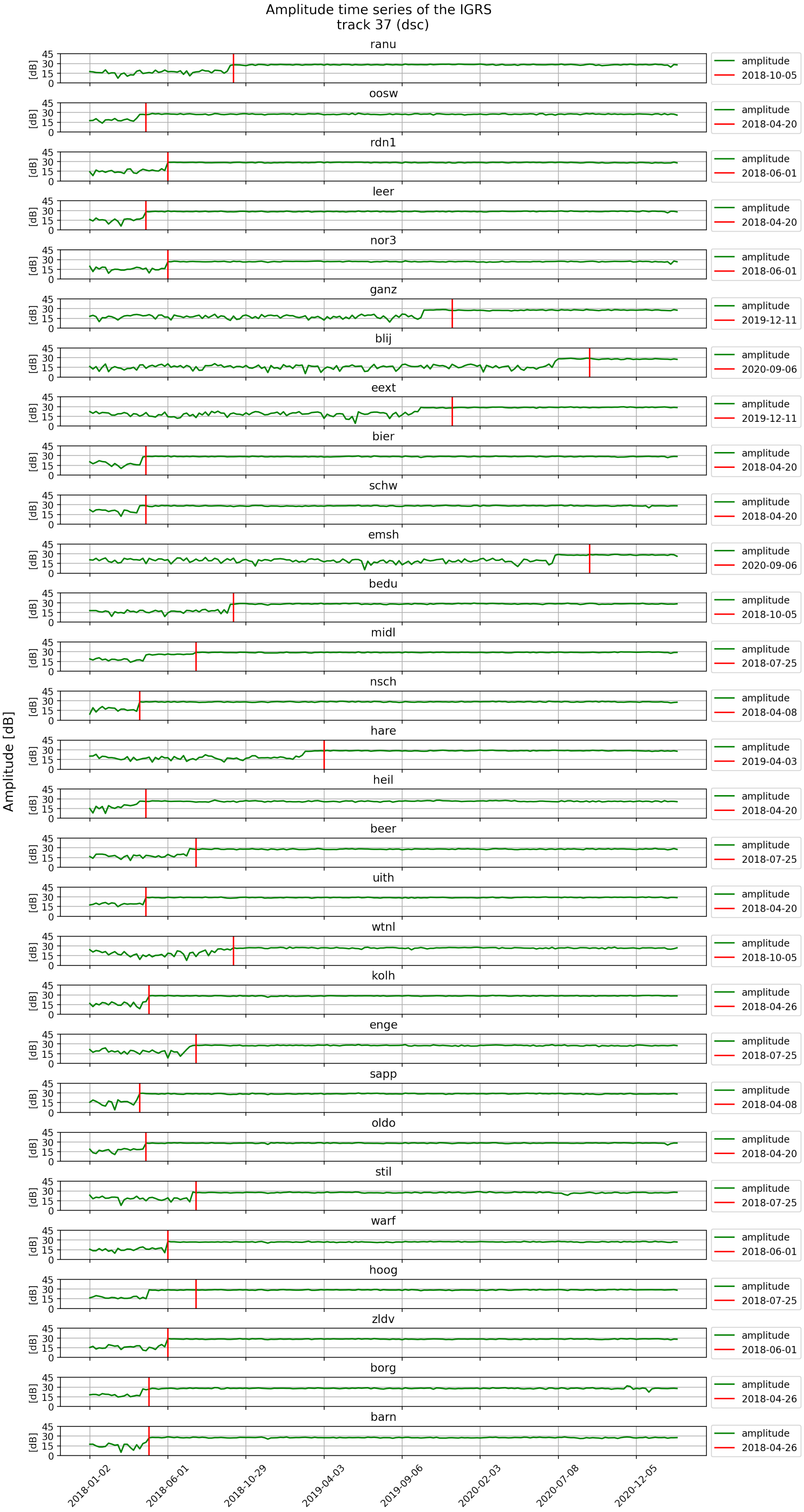

Figure B.1: Amplitude time series of all IGRS, track 37. This plot shows the amplitude time series of the IGRS, starting before their installation date. The installation date can be found in the legend of each plot and is indicated by the red line in the plots.

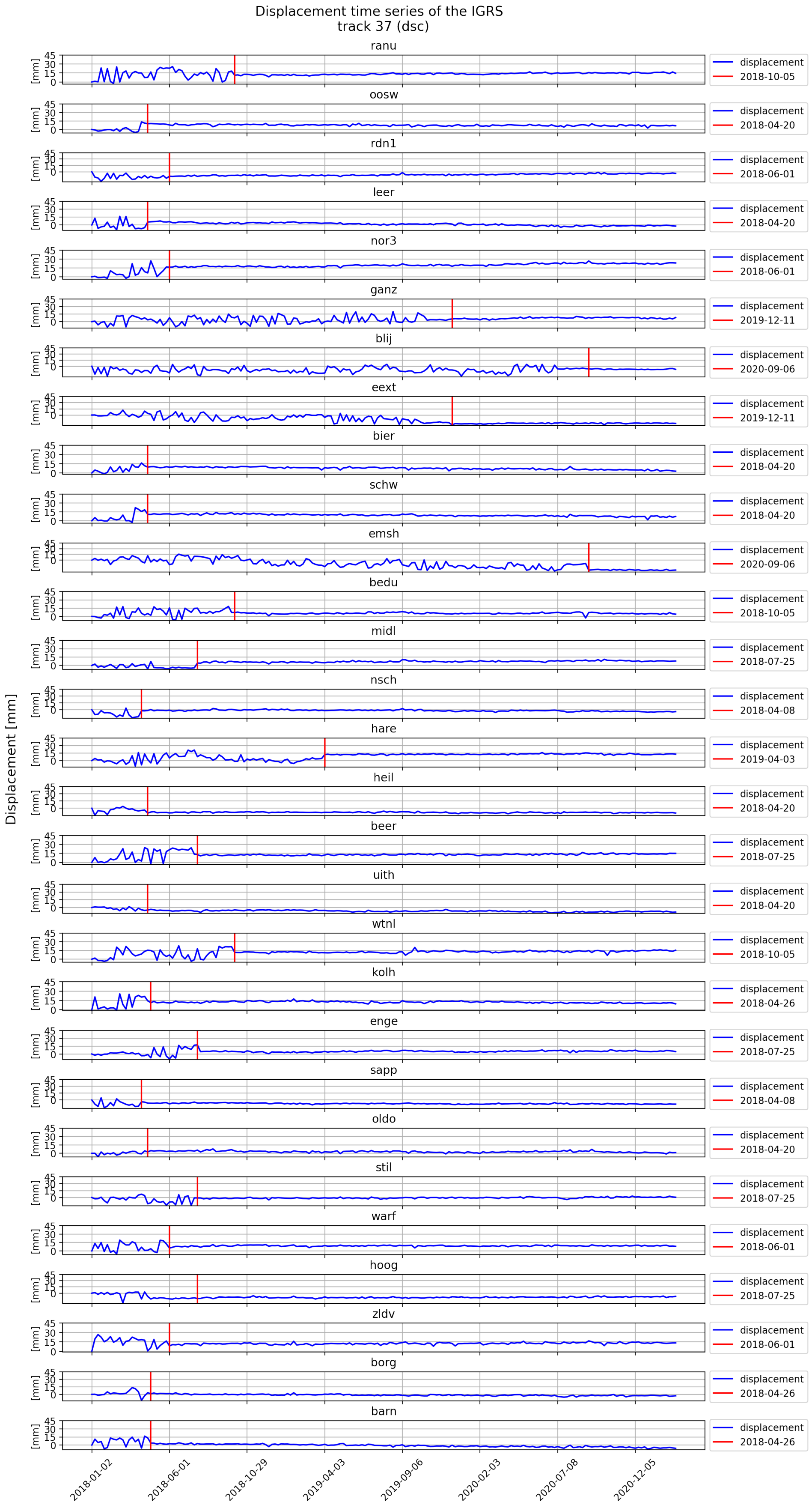

Figure B.2: Displacement time series of all IGRS, track 37. This plot shows the displacement time series of the IGRS, starting before their installation date. The installation date can be found in the legend of each plot and is indicated by the red line in the plots.

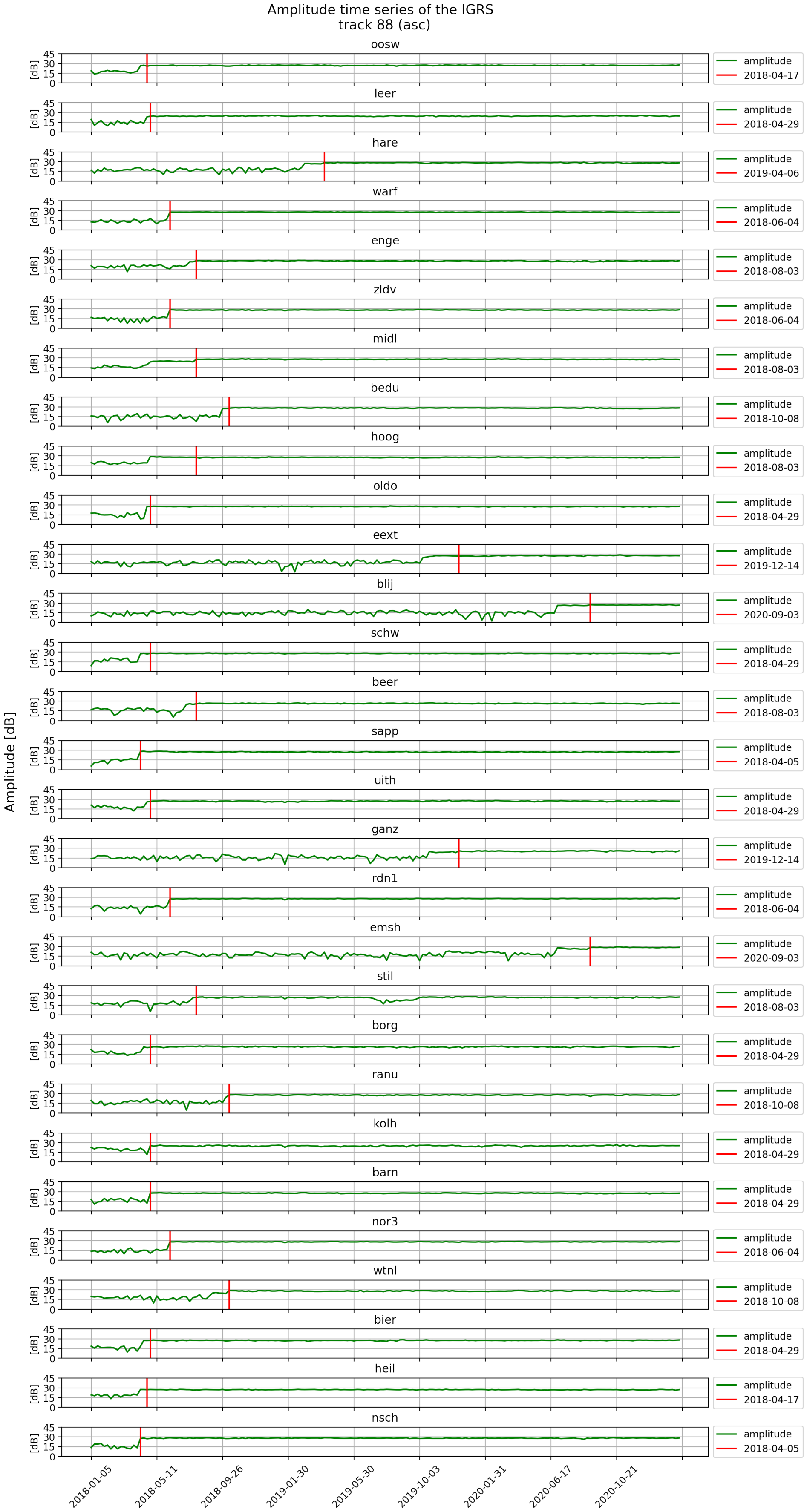

Figure B.3: Amplitude time series of all IGRS, track 88. This plot shows the amplitude time series of the IGRS, starting before their installation date. The installation date can be found in the legend of each plot and is indicated by the red line in the plots.

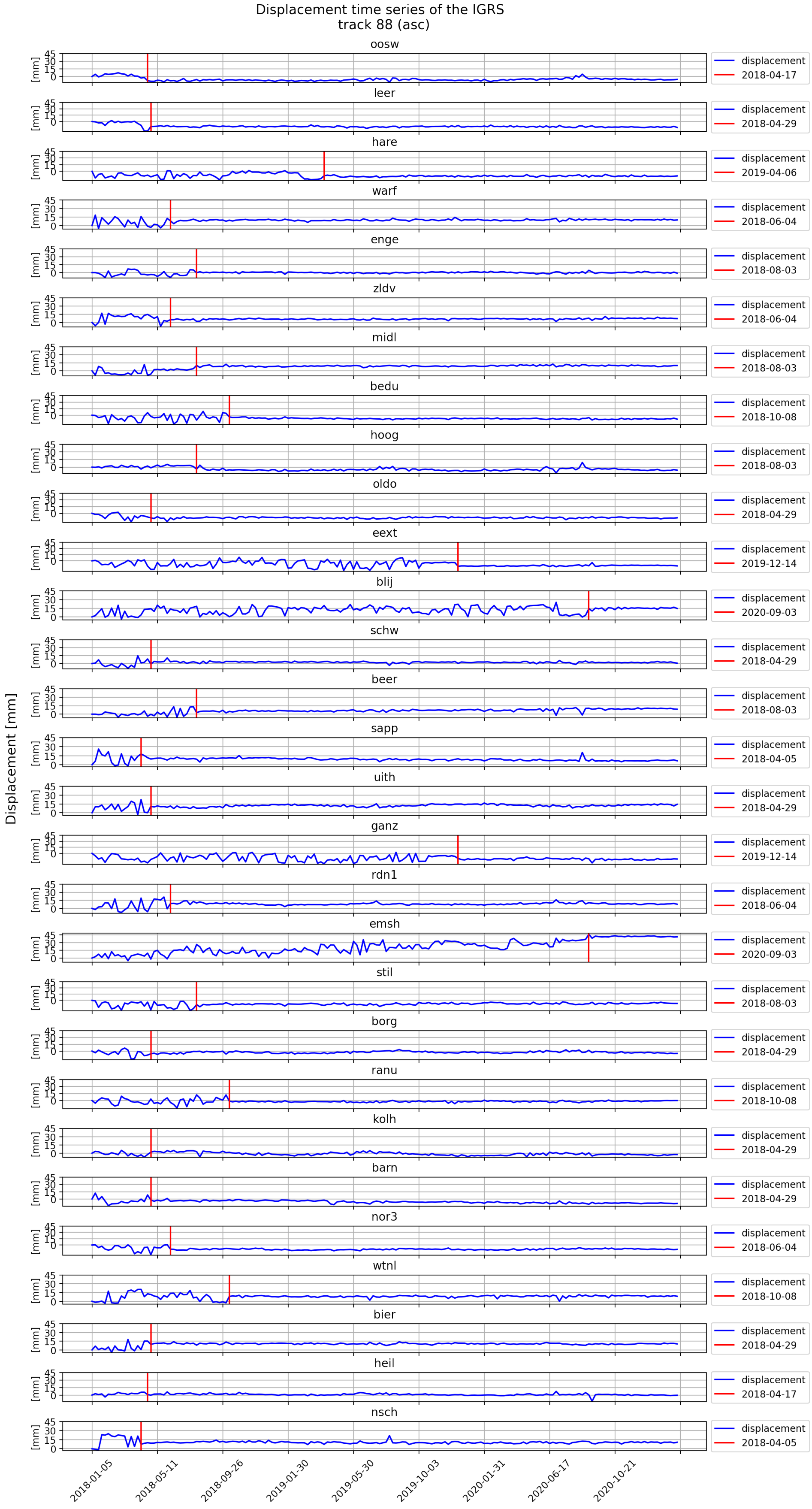

Figure B.4: Displacement time series of all IGRS, track 88. This plot shows the displacement time series of the IGRS, starting before their installation date. The installation date can be found in the legend of each plot and is indicated by the red line in the plots.

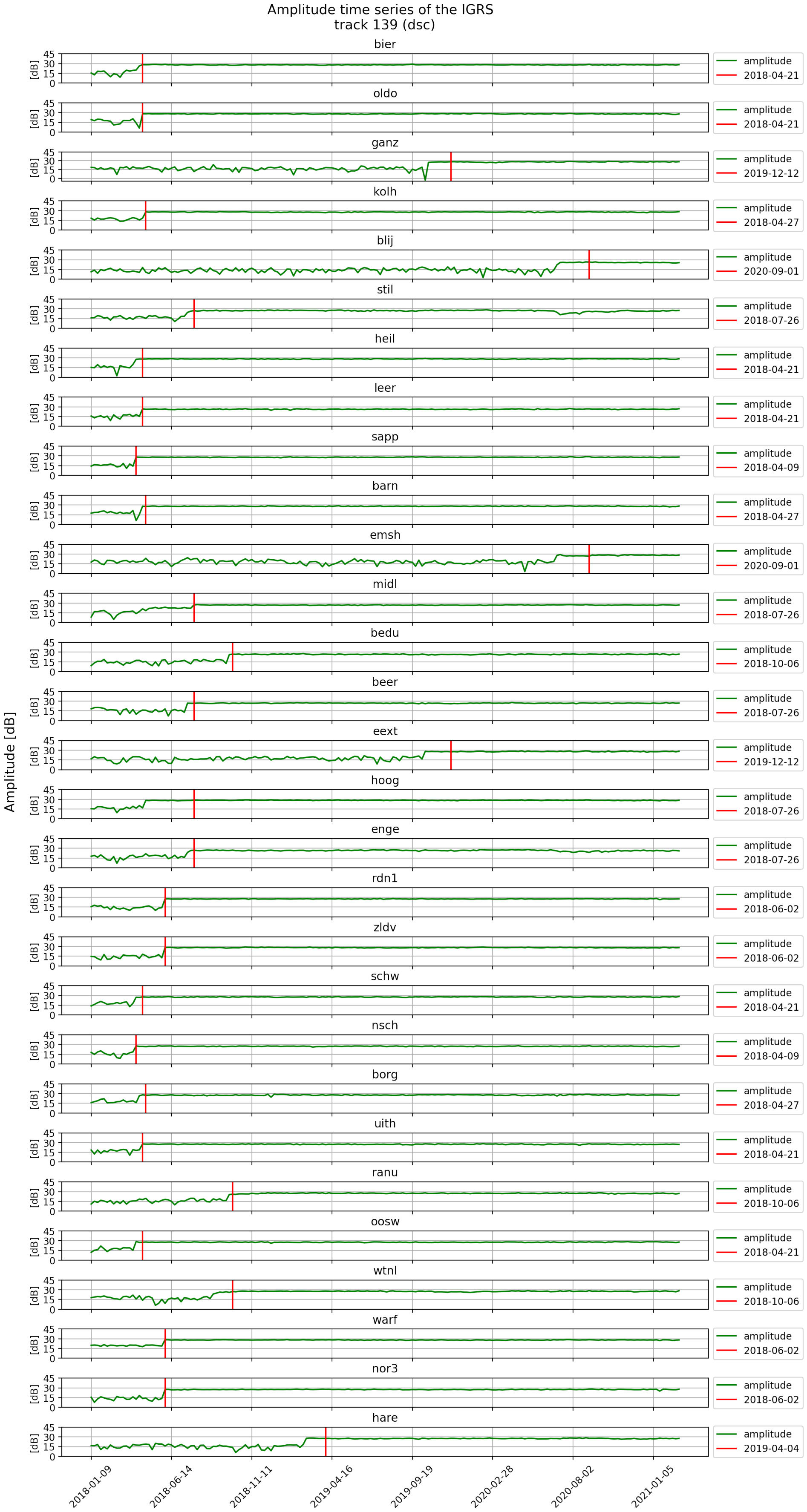

Figure B.5: Amplitude time series of all IGRS, track 139. This plot shows the amplitude time series of the IGRS, starting before their installation date. The installation date can be found in the legend of each plot and is indicated by the red line in the plots.

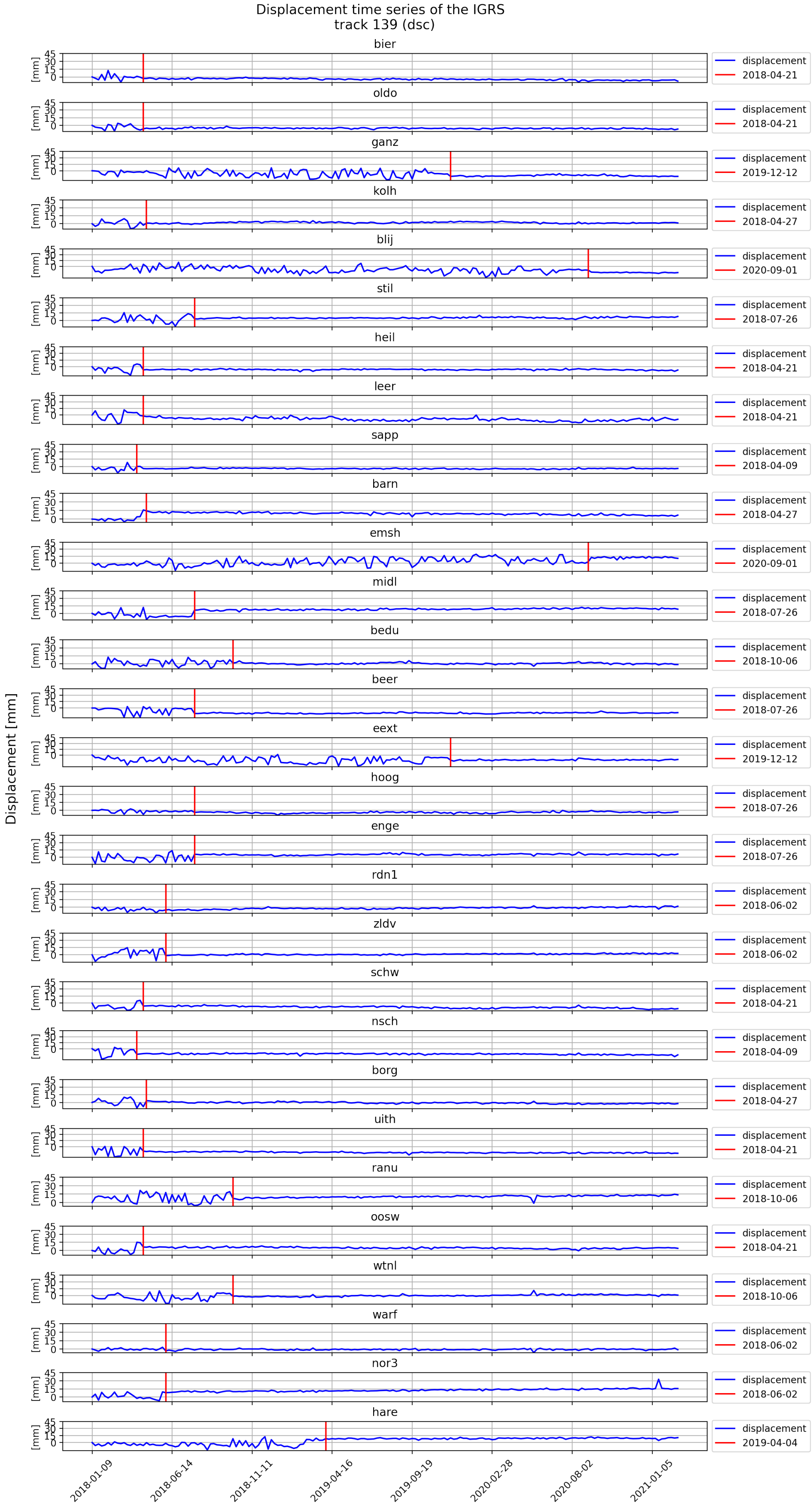

Figure B.6: Displacement time series of all IGRS, track 139. This plot shows the displacement time series of the IGRS, starting before their installation date. The installation date can be found in the legend of each plot and is indicated by the red line in the plots.

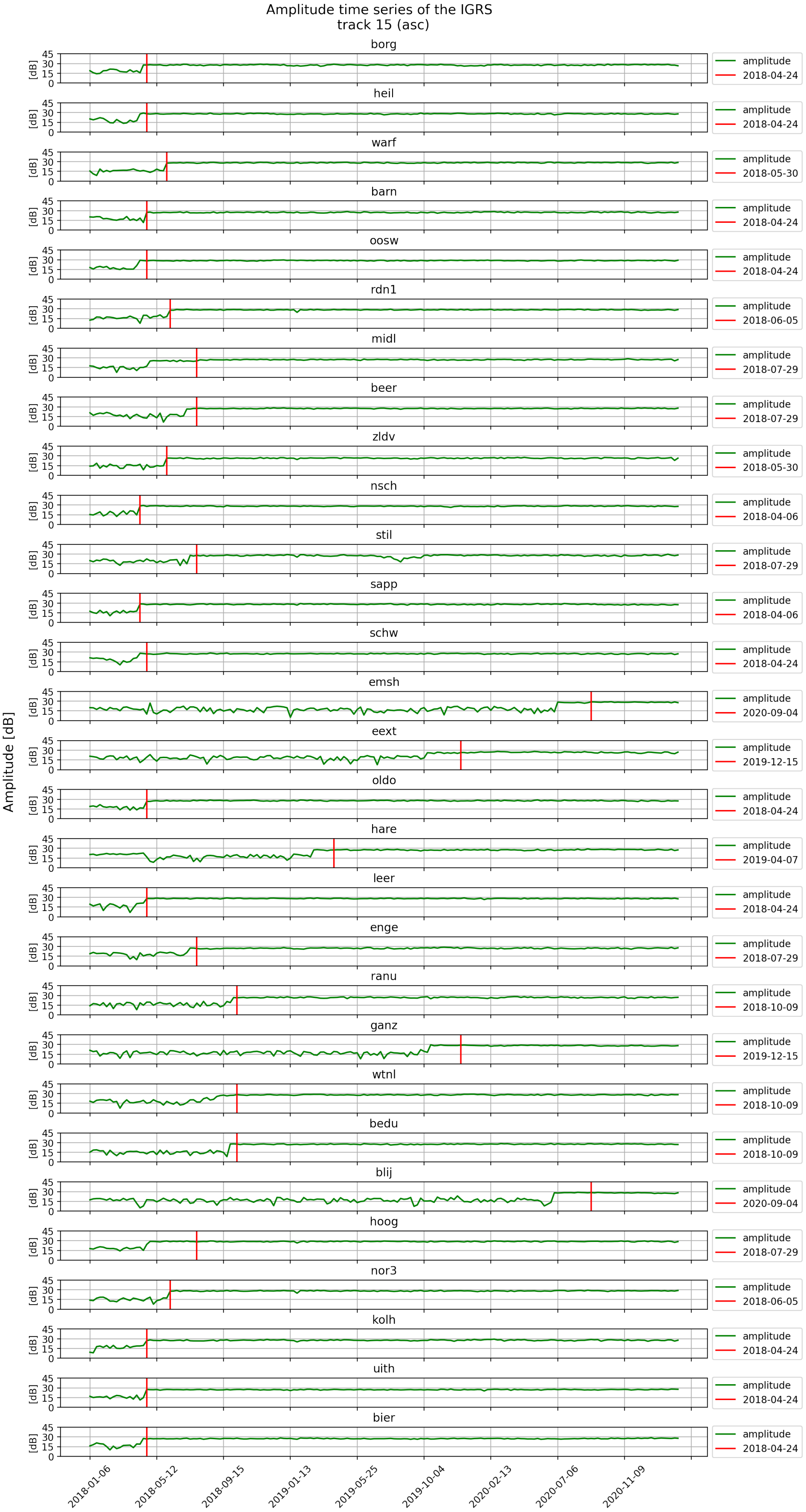

Figure B.7: Amplitude time series of all IGRS, track 15. This plot shows the amplitude time series of the IGRS, starting before their installation date. The installation date can be found in the legend of each plot and is indicated by the red line in the plots.

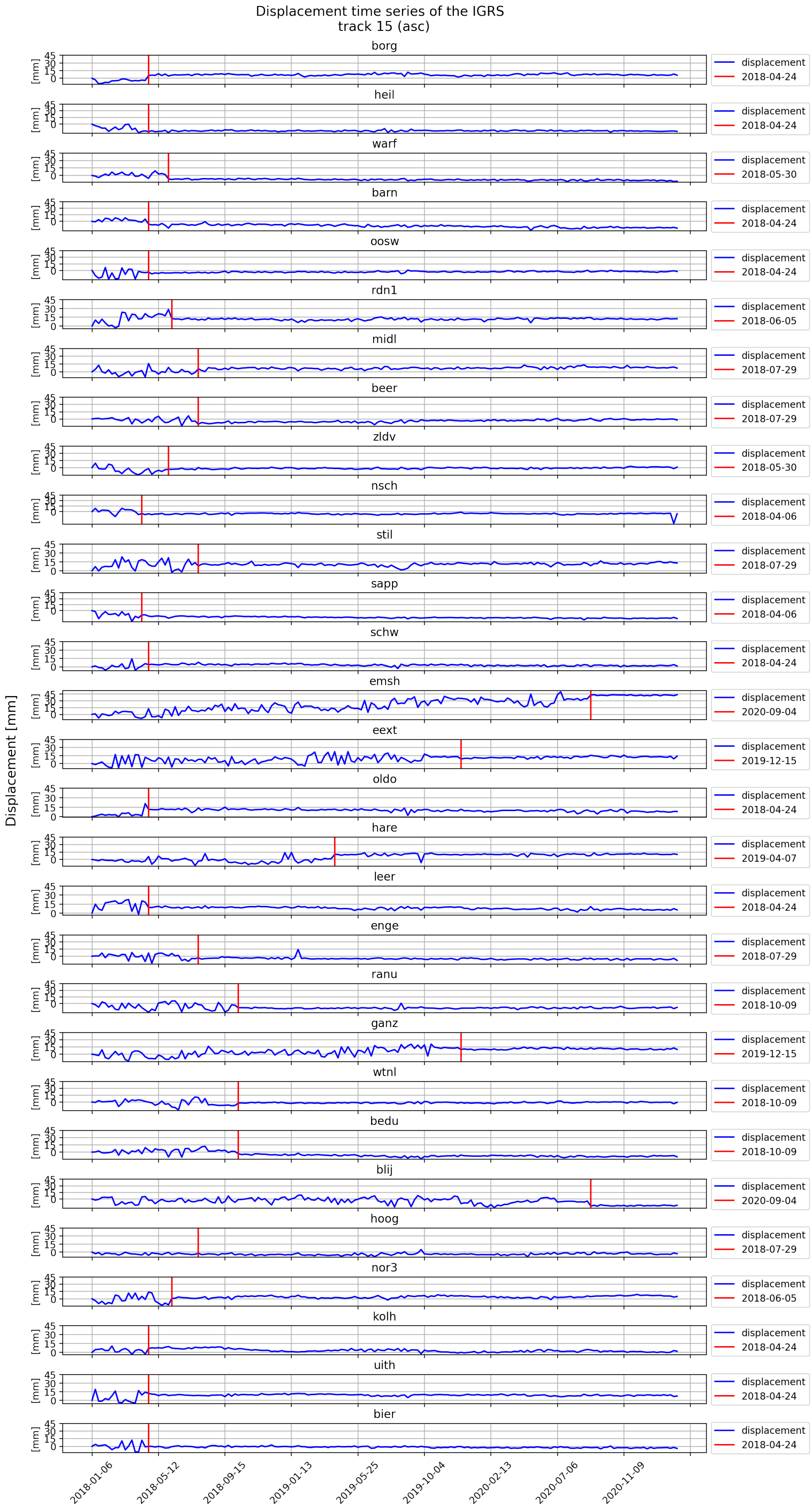

Figure B.8: Displacement time series of all IGRS, track 15. This plot shows the displacement time series of the IGRS, starting before their installation date. The installation date can be found in the legend of each plot and is indicated by the red line in the plots.

C

InSAR and GNSS residual arcs

In this appendix we can find the plots for tracks 88 (asc), 193 (dsc) and 15 (asc) showing the double-difference residuals of the time-series between the InSAR and the GNSS observations.

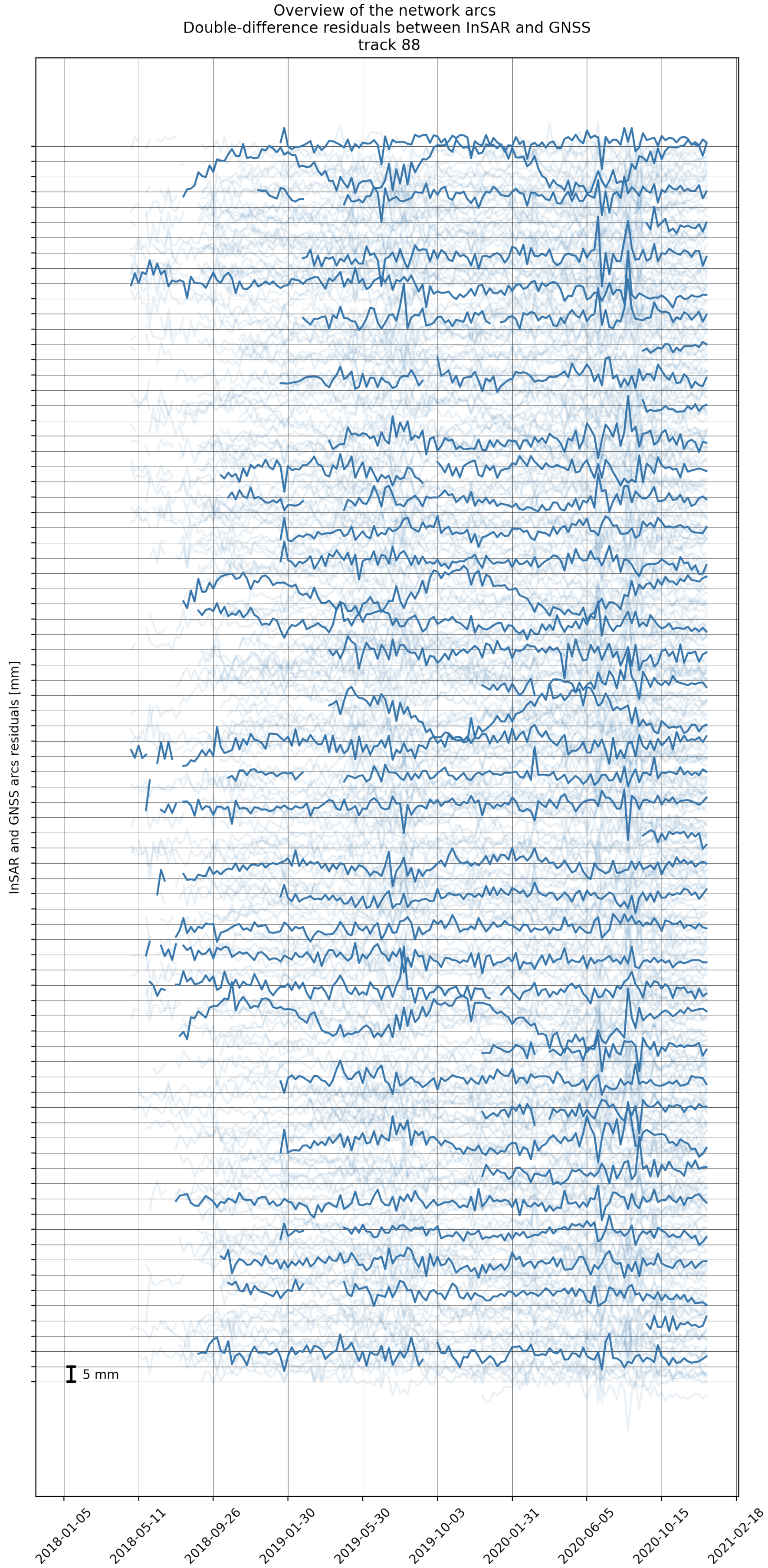

Figure C.1: Residuals between InSAR and GNSS time-series, track 88. Here we see an overview of the time-series of the difference between InSAR and GNSS observations for all (406) the arcs of the IGRS network. Some arcs are plotted with blue, while others are shown in the background to make the plot more clear. As expected, all the time series deviate from zero.

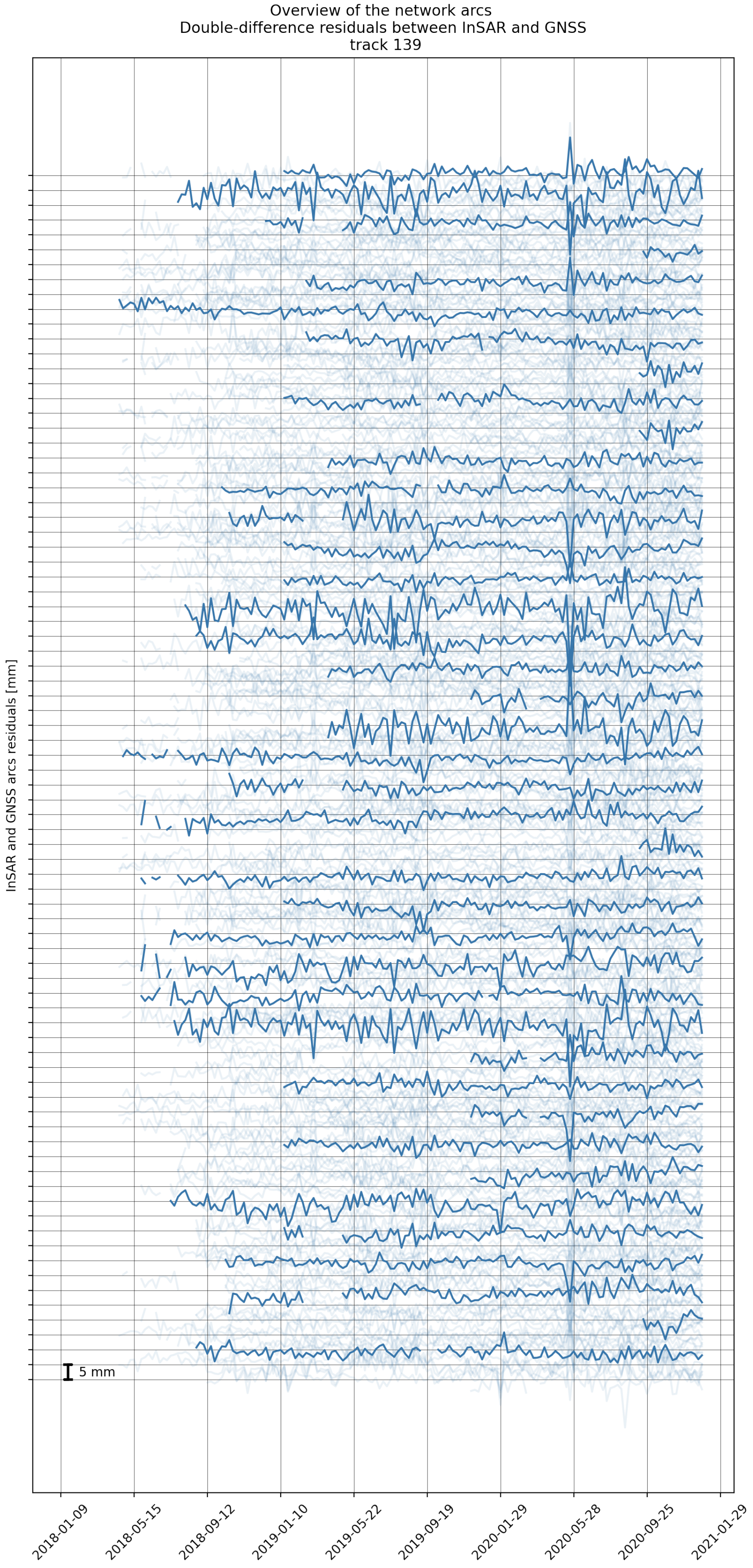

Figure C.2: Residuals between InSAR and GNSS time-series, track 139. Here we see an overview of the time-series of the difference between InSAR and GNSS observations for all (406) the arcs of the IGRS network. Some arcs are plotted with blue, while others are shown in the background to make the plot more clear. As expected, all the time series deviate from zero.

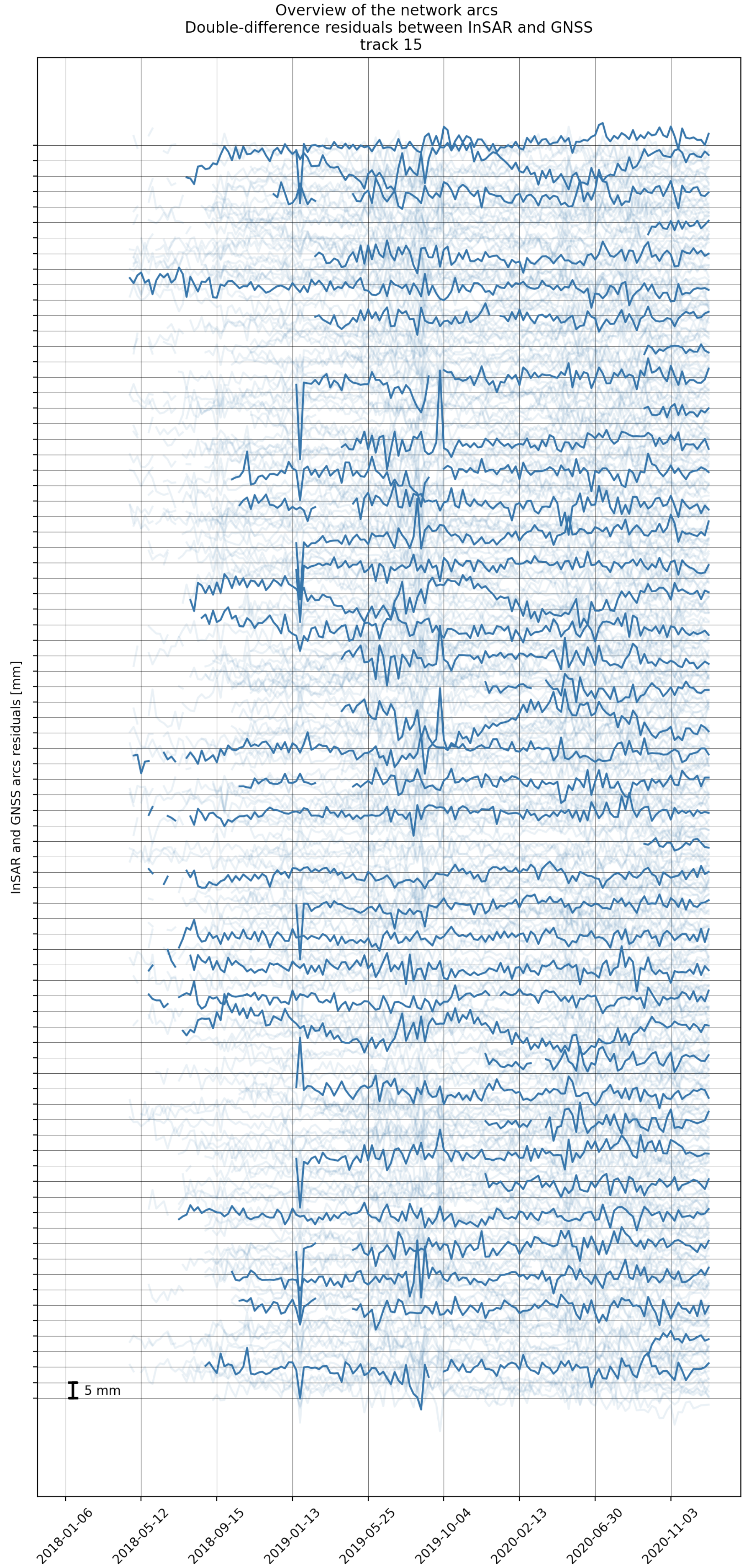

Figure C.3: Residuals between InSAR and GNSS time-series, track 15. Here we see an overview of the time-series of the difference between InSAR and GNSS observations for all (406) the arcs of the IGRS network. Some arcs are plotted with blue, while others are shown in the background to make the plot more clear. As expected, all the time series deviate from zero.

D

Atmospheric Phase Screens

In this appendix we can find the Atmospheric Phase Screens computed for satellite tracks 88 (asc), 139 (dsc), 15 (asc). The APS show the atmospheric contribution to the interferometric signal.

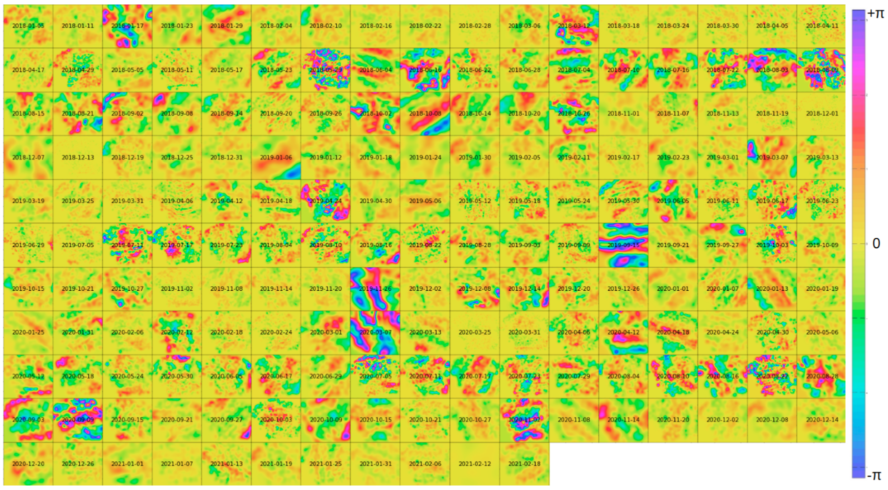

Figure D.1: Atmospheric Phase Screens, track 88. The APS show the atmospheric contribution to the interferometric signal. The area covered is around 60 × 60 km and the values run from $-\pi$ to π.

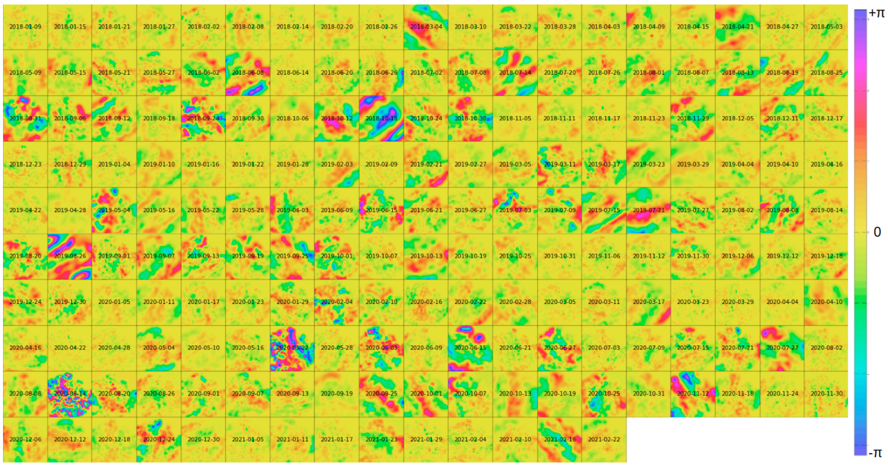

Figure D.2: Atmospheric Phase Screens, track 139. The APS show the atmospheric contribution to the interferometric signal. The area covered is around 60 × 60 km and the values run from $-\pi$ to π.

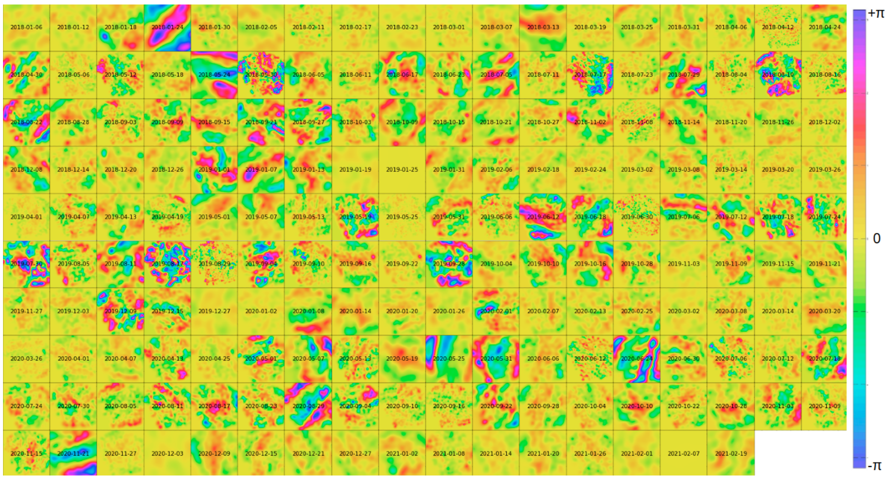

Figure D.3: Atmospheric Phase Screens, track 15. The APS show the atmospheric contribution to the interferometric signal. The area covered is around 60 × 60 km and the values run from $-\pi$ to π.

E

W-test results

In this appendix we can find the plots depicting the absolute w values computed for tracks 139 (dsc) and 15 (asc).

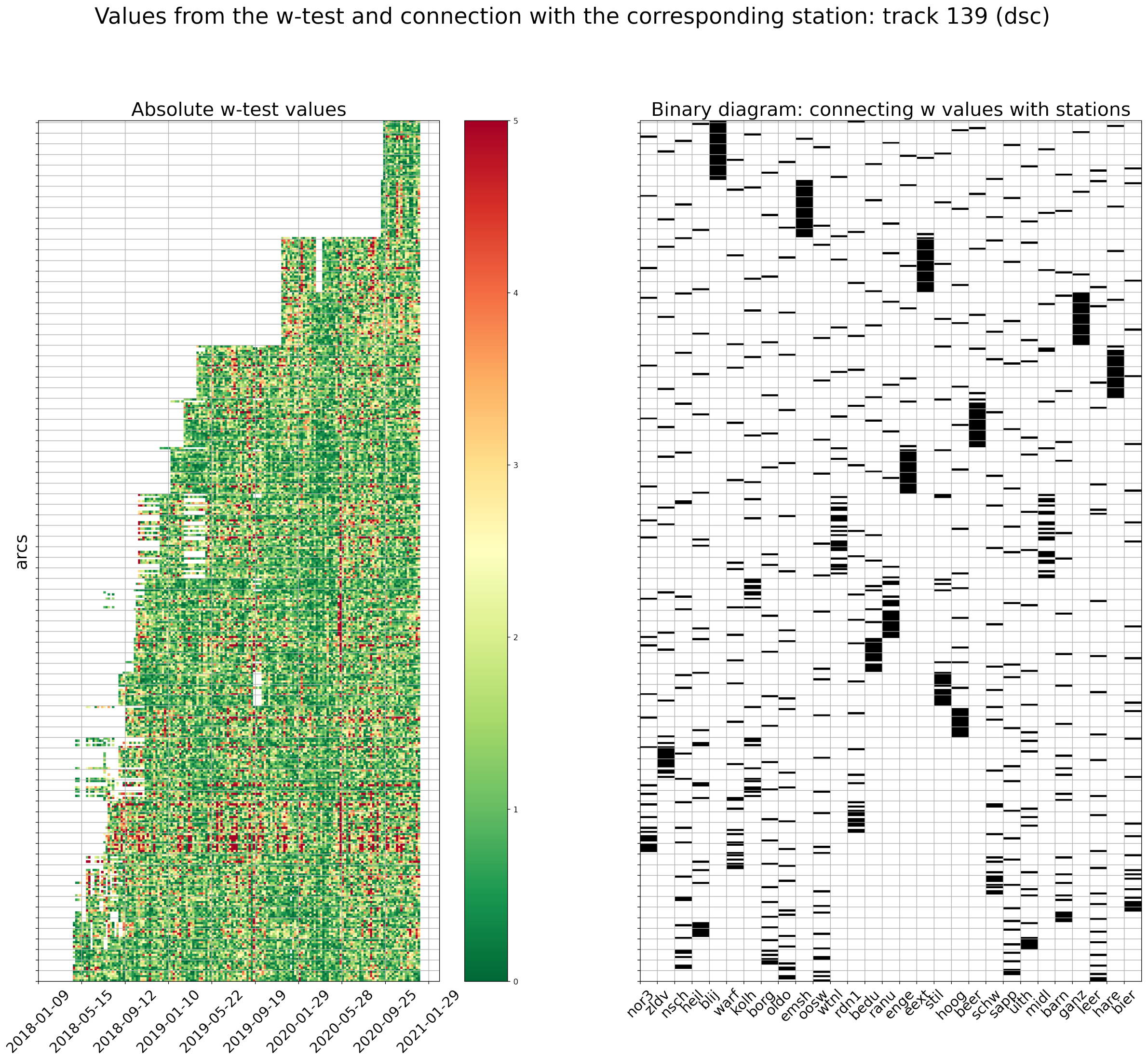

Figure E.1: Plot with the w-test values for track 139. On the left hand side we can see a mesh grid with the absolute value of the w-test and on the right hand side we can see in a binary diagram which helps us understand which stations are involved in each arc.

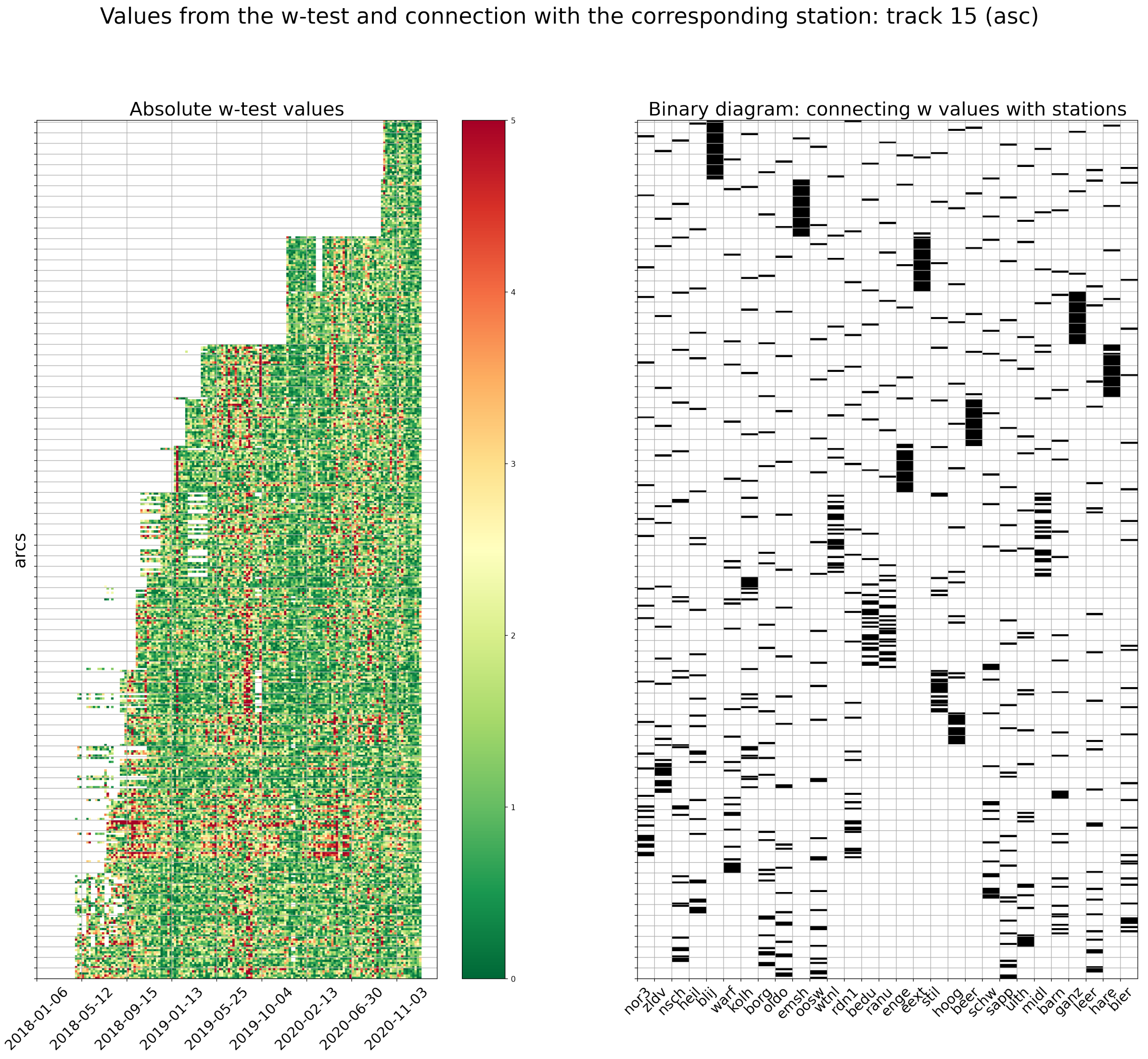

Figure E.2: Plot with the w-test values for track 15. On the left hand side we can see a mesh grid with the absolute value of the w-test and on the right hand side we can see in a binary diagram which helps us understand which stations are involved in each arc.